Title
Nonequilibrium energy surfaces and discrete solvent environments in solution-phase chemical bond breaking

Author
Vong, Andy

Publication Date
2022

Peer reviewed|Thesis/dissertation

UNIVERSITY OF CALIFORNIA

Los Angeles

Nonequilibrium energy surfaces and discrete solvent environments in solution-phase chemical bond breaking

A dissertation submitted in partial satisfaction of the
requirements for the degree Doctor of Philosophy
in Chemistry

by

Andy Vong

2022

ABSTRACT OF THE DISSERTATION

Nonequilibrium energy surfaces and discrete solvent environments in solution-phase chemical bond breaking

by

Andy Vong
Doctor of Philosophy in Chemistry
University of California, Los Angeles, 2022
Professor Benjamin J. Schwartz, Chair

Solvent dynamics are varied, complex, and can even change during the course of a chemical reaction. At the same time, they can be important for understanding the physics of solution-phase chemistry, thus requiring a framework for which to think about solvent effects. On one side, energy surfaces capture the average behavior of the reaction dynamics, but it is not clear how energy surfaces for solution-phase reactions ought to be constructed. On the other side, response functions capture the solvent fluctuations and provide information on how the solvent responds to changes of reacting solutes. This thesis explores the nature of solvent dynamics during the course of a bond-breaking reaction using the simulated photodissociation dynamics of Na_2^+ in liquid Ar and tetrahydrofuran (THF).

Following the introduction, Chapter 2, reprinted with permission from Andy Vong, Devon R. Widmer, and Benjamin J. Schwartz "Nonequilibrium Solvent Effects During Photodissociation in Liquids: Dynamical Energy Surfaces, Caging and Chemical Identity" *J. Phys. Chem. Lett.* **2020**, *11*, 9230–9238, identifies key photodissociation dynamics in Ar and THF and how energy surfaces for solution-phase reactions may be constructed. The potential energy surfaces of solution-phase reactions are generally inherited from gas-phase potentials or calculated by assuming that the solvent is in equilibrium with the solute, commonly referred to as the potential of mean force. For

photodissociation reactions, which are molecularly "violent", it is unlikely for the solvent to remain at equilibrium with the dissociating solute. Alternatively, a time-integral of work expression can directly capture the nonequilibrium dynamics to create a dynamical, nonequilibrium energy surface. For Na_2^+ in liquid Ar, the dynamical energy surface shows clear signatures of solvent caging, and the degree of caging is directly related to the mass of the solvent atoms. For Na_2^+ in liquid THF, local specific interactions between the solute and solvent lead to changes in chemical identity that create a kinetic trap that effectively prevents the molecule from dissociating. For both systems, this time-integral of work expression captures the key nonequilibrium effects during bond breaking, providing an example of how solution-phase energy surfaces may be constructed and indicating how both a gas-phase energy surface and potential of mean force are inadequate for describing solution-phase dynamics.

In Chapter 3, reprinted with permission from Andy Vong and Benjamin J. Schwartz "Bond-Breaking Reactions Encounter Distinct Solvent Environments Causing Breakdown of Linear Response" *J. Phys. Chem. Lett.* **2022**, *13*, 6783–6791, the nature of the solvent dynamics during the photodissociation of Na_2^+ in liquid Ar are followed along the bond-length coordinate. Surprisingly, we find that the solute experiences a small number of solvent environments that change in a discrete fashion as the bond lengthens. We also test a common assumption about nonequilibrium solvent fluctuations, the linear response approximation, and find that linear response fails by all measures, even when nonstationarity of solvent dynamics is considered. The observation of distinct solvent response environments with a solvent that can undergo only translational motions highlights the complexity of solute-solvent interactions, but that there are only a few environments give hope to the idea that solvation dynamics can be understood for solution-phase reactions that explore a wide configuration space, such as photodissociation.

In Chapter 4, reprinted with permission from Andy Vong, Kenneth J. Mei, Devon R. Widmer, and Benjamin J. Schwartz "Solvent Control of Chemical Identity Can Change Photodissociation into Photoisomerization" *J. Phys. Chem. Lett.* **2022**, *13*, 7931–7938, we improve upon the dynamical energy surface of Na_2^+ in THF by explicitly considering the motion of neighboring solvent molecules. Moderate locally-specific solute-solvent interactions can make it more appropriate to think of neighboring solvent molecules as a part of the solute's chemical identity. By focusing on the dynamics of a $Na_2(THF)_n^+$ complex, rather than just Na_2^+, we identify a second reaction coordinate

and formulate a two-dimensional dynamical energy surface. This new energy surface highlights how solvent effects changes what would be a strictly dissociative reaction in the gas phase into a two-step, sequential reaction with the first step similar to a photoisomerization reaction, and the second step being a weakly dissociative step.

Overall, this work serves as a reference point for developing a framework for thinking about solution-phase chemistry by considering how energy surfaces might be constructed for these reactions and detailing how the solute can experience discrete changes in solvent dynamics and environments.

The dissertation of Andy Vong is approved.

William M. Gelbart

Justin R. Caram

Christopher R. Anderson

Benjamin J. Schwartz. Committee Chair

University of California, Los Angeles

2022

To my mother for her endless love and support

and to all other parents that enable their children to follow their ambitions.

I truly am privileged to be your son.

Contents

List of Figures

List of Tables

ACKNOWLEDGEMENTS

I would not have gotten through grad school without the help of many people. Firstly, I need to thank my advisor, Ben Schwartz, for his scientific advice but more importantly for his support and encouragement. I am not special enough to not be burdened by self-doubt and it means a lot to have an advisor that believes in you and appreciates your work. I also need to thank Devon Widmer, a previous graduate student for setting me up with the group code. Next, I would like to thank Alex Sercel, Sanghyun Park, Quynh Duong, and Ken Mei for their friendship throughout grad school. I also thank the remainder of the Schwartz group for their support. It certainly has been an a harrowing yet entertaining and stimulating time. Below are the particular acknowledgements for my published works, included as reprints.

Chapter 2 is reprinted with permission from Andy Vong, Devon R. Widmer, and Benjamin J. Schwartz. "Nonequilibrium Solvent Effects During Photodissociation in Liquids: Dynamical Energy Surfaces, Caging and Chemical Identity" *J. Phys. Chem. Lett.* **2020**, *11*, 9230–9238. doi.org/10.1021/acs.jpclett.0c02515. Devon Widmer, my co-author for this paper, collected the data for and completed analysis for Na_2^+ in THF. Ben Schwartz is the PI.

Chapter 3 is reprinted with permission from Andy Vong and Benjamin J. Schwartz. "Bond-Breaking Reactions Encounter Distinct Solvent Environments Causing Breakdown of Linear Response" *J. Phys. Chem. Lett.* **2022**, *13*, 6783–6791. doi.org/10.1021/acs.jpclett.2c01656. Ben Schwartz is the PI.

Chapter 4 is reprinted with permission from Andy Vong, Kenneth J. Mei, Devon R. Widmer, and Benjamin J. Schwartz. "Solvent Control of Chemical Identity Can Change Photodissociation into Photoisomerization" *J. Phys. Chem. Lett.* **2022**, *13*, 7931–7938. doi.org/10.1021/acs.jpclett.2c01955. Ken Mei, my co-author for this paper, helped with the analysis and data collection. Ben Schwartz is the PI.

This work was supported by the U.S. Department of Energy Condensed Phase and Interfacial Molecular Science program under Grant No. DOE-CPIMS-0000228903.

VITA

The author earned a Bachelor of Science in Chemistry and a Bachelor of Science in Mathematics from Northeastern University. While at Northeastern, he worked in electrochemistry with Eugene Smotkin. He also worked as a battery engineer intern where his interests in solvation dynamics were sparked.

Upon entering UCLA, he transitioned to theory and began working with Ben Schwartz initially on the cavity dynamics of THF and water. Later, he transitioned to working on the photodissociation dynamics of Na_2^+ in liquid Ar and THF. In 2021, he earned the Ralph and Charlene Bauer Award for excellence in research, teaching, and service. He published three first-authored papers all in a top-tier journal, *The Journal of Physical Chemistry Letters*.

Chapter 1

Introduction

1.1 Solvent Effects in Solution-Phase Chemical Dynamics

Solvents can affect chemical reactivity in a variety of ways. On one hand, solvents can be thought of as having minimal effect where they act as a background medium for which reacting solute molecules encounter one another via diffusion. On the other hand, solvents can play an integral role in chemical reactivity, including the formation of solvent-supported species such as solvated electrons[1] and charge-transfer-to-solvent reactions.[2, 3] In addition to these special cases, solvent molecules can "cage" the dissociating solute molecules of photodissociation reactions, inhibiting separation of photofragments and promoting recombination.[4–8]

Despite the impact of solvent effects being widely recognized, current frameworks for thinking about solvent dynamics and the way they affect chemical reactivity is limited. Chemists like to think about chemical reactions as occurring on a potential energy surface (PES), i.e. a high-dimensional energy landscape of the system energy as a function of the reaction coordinate(s). For gas-phase bond-breaking reactions, the PES creates a textbook-like understanding of chemical physics: the PES for a gas-phase chemical bond, which we like to think about as acting like a spring, is a Morse potential.

However, solvent motions can instantaneously and strongly perturb chemical bonds, making it difficult for a simple PES to describe solution-phase dynamics.[9–18] Given the challenge of solution-phase dynamics, potentials of mean force (PMF) are frequently used as a PES to describe solution-phase chemistry. Although PMFs have successfully described solution-phase dynamics at

equilibrium,[19, 20] they do not describe nonequilibrium solution-phase reactions terribly well, and particularly poorly for solution-phase bond-breaking dynamics.[10]

Aside from energy surfaces, which are useful for describing average behavior, solvent response functions, which measure the solvent fluctuations and how the solvent responds to changes in the solute, are frequently used to understand solution-phase dynamics.[21–25] Rather than perform nonequilibrum simulations, equilibrium fluctuations can used to approximate the nonequilibrium fluctuations according the the linear response approximation (LR). For bond-breaking reactions which explore a large configuration space, the solvent dynamics can change with the reaction coordinate, potentially affecting the LR approximation.

This dissertation explores the nature of solvent effects in nonequilibrium bond-breaking reactions. The key motivations of the dissertation are (1) what energy surfaces can be used to describe such reactions, (2) how should such energy surfaces be constructed, (3) what considerations are important while constructing these surfaces, and (4) how do the solvent fluctuations change as the reacting molecules traverse the reaction energy surface. In the following chapters, we explore what energy surfaces can be used to describe the nonequilibrium bond-breaking dynamics of Na_2^+ in liquid Ar, one of the simplest chemical solvents. Next, we explore how the solvent dynamics changes during the course of the reaction and in the process we also test ideas of LR, which uses information about equilibrium dynamics to predict nonequilibrium dynamics. Finally, we explore how the identity of the solvent can alter the energy surfaces on which the reaction occurs by exploring the bond-breaking dynamics of Na_2^+ in liquid THF.

1.2 Reactive Energy Surfaces for Understanding Chemical Dynamics

Solution-phase chemical reactions are inherently difficult systems to study given the stochastic nature of solvents and issue of many-body effects. For fundamental chemical processes such as bond-breaking, the solution-phase photodissociation of diatomic molecules in rare gas solvents has been the focus of many studies,[5, 8, 10, 26, 27] with particular emphasis on molecular iodine (I_2).[4, 6, 7, 28–31] The dominant solvent-induced dynamics of these systems include solvent caging, trapping, and recombination, and the simplest description simply describes the photodissociation

steps as occurring on the PES of the gas-phase solute molecule.[29] This means that even though solvent effects on chemical reactivity have been identified, the underlying surfaces on which reaction dynamics occur do not contain information about how the solvent alters the PES.

One way to include such solvent information directly into the energy surface is through the PMF. The PMF includes the average equilibrium solvent contribution to the system energy as a function of the reaction coordinate, which for bond-breaking is the bond separation length. PMFs, in practice, are calculated using importance sampling methods like umbrella sampling. With umbrella sampling, the bond separation is restrained via an umbrella potential that allows the solvent to fluctuate at equilibrium around the solute. Therefore, the PMF includes the average equilibrium solvent contribution. For molecularly "violent" reactions, including photodissociation, the solvent generally does not remain at equilibrium with the solute, so a PMF description is bound to fail.

Alternatively, the nonequilibrium solvent contribution to the system energy can be included by integrating the average solvent force over time to create a time-integral of work expression.[11, 32] Mathematically, this comes out to:

$$U(r(t)) = -\int_{t_0}^{t} F(r(t)) \cdot v(t) dt, \tag{1.1}$$

where F is the average force acting on the dissociating molecule, v is the bond velocity, and t_0 is the time at which photoexcitation takes place. In work published in *J. Phys. Chem. Lett.*, Ref. 11, and summarized in the following chapter of this dissertation, we explore how well this expression captures the nonequilibrium solvent dynamics of a homonuclear diatomic molecule, Na_2^+, in two solvent systems, liquid Ar and liquid tetrahydrofuran (THF). Then, in work published in *J. Phys. Chem. Lett.*, Ref. 33, and summarized in the fourth chapter, we extend this formalism using the enthalpy of the solute to define a two-dimensional energy surface that explicitly uses solvent degrees of freedom, highlighting how the solvent system can change the identity of the solute.

1.3 Can Equilibrium Dynamics be Used to Understand Nonequilibrium Dynamics?

By comparing PMFs and a time-integral of work expression, we can learn about the average behavior of the equilibrium and nonequilibrium ensemble, but such comparisons do not include information about the equilibrium and nonequilibrium solvent fluctuations. In other words, comparisons of energy surfaces do not provide information about the equilibrium and nonequilibrium solvent response or how the solvent responds to perturbations of the solute, and understanding the solvent response is as important as understanding energy surfaces.

By invoking the LR approximation, the nonequilibrium solvent response can be predicted using the equilibrium response, allowing nonequilibrium simulation dynamics (which are computationally expensive) to be avoided. There are two common invocations of LR. The first uses the ground-state equilibrium dynamics of the solute and can be arrived at by assuming a perturbation of the ground-state dynamics, similar to the Onsager regression hypodissertation.[24, 34, 35] The second uses the excited-state equilibrium dynamics of the solute and be arrived at using a stronger condition based on Gaussian statistics since linear-response predictions are obeyed exactly if the liquid fluctuations obey Gaussian statistics.[35, 36].

Although LR approximations have performed remarkably well,[22, 37–39] there are many cases in which LR fails.[24, 25, 35, 36, 40–49] When the solute is moderately large, such as in the case of coumarin 153 and N-methyl-6-oxyquinolinium betaine, changes in dipole moment in a polar solvent can lead to an adherence of LR.[22] Others have also argued that LR holds as long as only the charge state of the solute changes,[39, 50] but not the size of the solute.[43, 51, 52] However, there are many cases where LR fails following only a change in charge distribution.[40, 42, 53, 54]

When LR fails, it is often due to the contribution of just a few solvent degrees of freedom that have an outsized effect on the chemical dynamics, causing the fluctuations to be non-Gaussian and thus violating the assumptions behind LR. Some notable examples include the rotational coherence of a rigid rotor,[45] a dipole reversal and subsequent solvent restructuring,[25] and solutes that undergo significant changes in size and shape.[43, 46, 47] LR also can fail when the solvent response occurs on a timescale similar to changes in a solute's physical or electronic structure.[36, 40] Even when LR appears to hold, it can still fail for hidden reasons like when the equilibrium

and nonequilibrium responses appear similar but follow different relaxation dynamics.[24]

There is also theoretical work arguing that a formalism incorporating non-stationary dynamics might be a way to extend the validity of LR.[42] For photodissociation reactions whose dynamics are strongly affected by solvent caging, which is a nonequilibrium effect, it is unlikely that LR will hold. However, it is still interesting to observe what particular solvent motions cause LR to fail. Furthermore, because photodissociation covers a wide range of configuration space, it is interesting to see how the equilibrium and nonequilibrium dynamics change along the reaction coordinate which will inform how a non-stationary approach to LR might be pursued. In work published in *J. Phys. Chem. Lett.*, Ref. 49, and summarized in Chapter 3 of this dissertation, we explore how the solvent environment and dynamics change following photoexcitation and show that both change discretely with the reaction coordinate whether following the equilibrium or nonequilibrium pathway. We also explore the implications for LR and show that no matter how LR might be applied, non-stationary or otherwise, LR fails.

1.4 Mixed Quantum/Classical Molecular Dynamics

The work carried out in this dissertation was done using mixed quantum/classical (MQC) molecular dynamics (MD) of Na_2^+ in either liquid Ar or liquid tetrahydrofuran (THF). In the MQC framework, the solvent molecules are treated classically and the solute, Na_2^+ is treated as two classical Na^+ cores bound by a fully quantum mechanical electron. The interaction between the quantum mechanical electron and classical particles are handled using Phillips Kleinman pseudopotentials[55] previously developed in the group and/or rigorously tested in the literature.[56–59] By using MQC MD, we are able to simulate large system sizes with either 1600 Ar atoms or 254 THF molecules spanning a simulation of box of at least 32.5 Å. With this system size we are able to explore dynamics nearing the dissociation limit of the solute.

The choice of Na_2^+ was made because we have previously studied the molecule[60] and similar solutes.[61–66] Additionally, with Na_2^+, the system can be reduced to a one-electron problem while still being accurately represented by MQC. Additional simulation details are provided in the relevant chapters below.

1.5 Summary of Dissertation Content

Solvents can affect chemical dynamics in a variety of chemically significant ways, but a foundation for which to think about solution-phase chemical reactions is lacking. This dissertation explores how energy surfaces can be used to think about solution-phase chemical reactions and how the solvation dynamics can change with time. Rather than explore all classes of chemical reactions, we focus on bond-breaking dynamics by simulating the photodissociation of Na_2^+ in liquid Ar and THF. Chapter 2 of the dissertation constructs a dynamical, nonequilibrium energy surface of both systems using the time-integral of work expression (Eq. 1.1) and compares it to various PMFs and the gas-phase PES, showing that neither the PMFs nor gas-phase PES can captures key nonequilibrium events, while the newly-constructed dynamical surface does. Chapter 3 shows that solvent dynamics and environment changes discretely along the reaction coordinate and that no LR construction, either non-stationary or otherwise, can predict the nonequilibrium dynamics. Chapter 4 of the dissertation revisits the construction of nonequilibrium energy surfaces specifically for Na_2^+ in liquid THF and shows how incorporating the neighboring solvent as a part of the solute's chemical identity can recast photodissociation as a two-step reaction with the first step being a photoisomerization reaction and the second step being a weakly dissociative reaction.

Chapter 2

Nonequilibrium Solvent Effects During Photodissociation in Liquids: Dynamical Energy Surfaces, Caging and Chemical Identity

2.1 Introduction

Most chemical reactions, including photodissociation reactions that use light to break chemical bonds, take place in solution. Since solution-phase reactions are inherently more complex than those in the gas phase, most studies of photodissociation and recombination dynamics have focused on simple diatomic molecules to elucidate solvent effects on chemical reaction dynamics,[5, 8, 10, 29, 67–69] with a particular emphasis on molecular iodine (I_2).[4, 6, 7, 28, 30, 31]

How can one use energy surfaces to think about solute and solvent motions involved in solution-

phase photodissociation? For the solute, a common approach when considering solution-phase reactions is to simply assume that the solute moves on the same potential energy surfaces as in the gas phase.[29] We have shown in recent work, however, that the Pauli repulsion interactions between the solvent and the solute's bonding electrons can change the electronic structure of diatomic solutes, inducing large instantaneous dipole moments and causing changes in the vibrational frequency and dissociation energy.[66] Moreover, we also have found that when there are local specific interactions between the solvent molecules and the solute that only need to have a strength comparable to that of a hydrogen bond, the electronic structure and even the chemical identity of the solute can be dramatically altered.[60, 61] Thus, one needs to go beyond gas-phase surfaces and include the way in which solutes and solvents interact to understand solution-phase chemical reactions.

Rather than assuming the solute moves on the same potential energy surface as in the gas phase, the solute could be thought of as moving along an effective potential energy surface where the solvent is at equilibrium with the solute, the so-called potential of mean force (PMF).[70] Such an approach can describe, on average, how the solvent will interact with and potentially alter the electronic structure of the solute, presuming that the solvent truly does remain in equilibrium throughout the course of the reaction.[5, 10, 29] For example, PMFs are appropriate for thinking about ion pairs in water: solute-solvent structures identified in the ground state PMF[71, 72] have been associated with those found with X-ray absorption,[73] neutron scattering,[74] and Raman spectroscopy.[75] And several groups have used PMFs to understand how solvent effects can alter electronic structure during proton transfer,[76] electron transfer,[38] proton-coupled electron transfer,[44] hydride transfer,[77], etc. and following electronic excitation of a dye molecule used as a solvation probe.[78]

For all of the success of using PMFs to interpret solution-phase chemistry, one generally does not expect the assumption of the solvent remaining at equilibrium to hold for a molecularly violent event like photodissociation, or even for chemistry that takes place on electronic excited states. Ishida and Rossky[12, 78] used excited-state PMFs to understand the solvent reorganization following the photoexcitation of a betaine dye. There also have been a few studies that used a semi-empirical description to concoct the potential energy surfaces governing solute motion following photoexcitation in solution.[69, 79] However, we are not aware of any investigations exploring the quantum mechanics of how solvents alter the electronic structure and excited-state reaction

dynamics of molecules in liquids, and for photodissociation in particular, one would not expect an equilibrium description to properly account for the strong 'caging' solvent collisions that promote recombination.[10] Thus, one of the primary goals of this work is to explore the use of a rigorous formalism, based on the time integral of work,[32] to describe nonequilibrium photodissociation dynamics in solution.

The key questions explored in this paper are: what type of potential energy surfaces should be used to think about the dynamics during condensed-phase photodissociation reactions? Given that the dissociation pathway can depend on solvent effects like caging or complexation, is it appropriate to think of the solvent as being in equilibrium with the solute, and if not, why not? If equilibrium energy surfaces do not capture solute and/or solvent dynamics, how should one think about the nonequilibrium dynamics? And what generalities about solution-phase photodissociation reactions can be learned by studying model systems, especially when local specific solute-solvent interactions can potentially alter the chemical identity of the solute?[60, 61]

In this Letter, we directly address all of these questions through mixed quantum/classical (MQC) molecular dynamics (MD) simulations of Na_2^+ in both liquid Ar and liquid tetrahydrofuran (THF). We choose this system because we already have explored how solvent interactions alter the ground-state solute electronic structure for both Na_2[61, 66] and Na_2^+[60] in these solvents; we focus on Na_2^+ here because it dissociates (in the gas phase) when placed on its lowest electronic excited state[80] and Na_2 does not. We find that taking the time integral of work leads to a dynamical energy surface that captures key solvent effects for understanding photodissociation of Na_2^+ in both Ar and in THF. In particular, solvent caging dominates the photodissociation dynamics of Na_2^+ in liquid Ar, something that is well-captured by the dynamical energy surface but not properly accounted for by the gas-phase surfaces or PMFs. For the photodissociation dynamics of Na_2^+ in THF, the dynamical energy surface shows how local specific interactions that dynamically change the solute's chemical identity create a kinetic trap that effectively prevents the molecule from dissociating the way it would at equilibrium.

2.2 Results and Discussion

To investigate the type of potential energy surfaces that best elucidate the dynamics of condensed-phase photodissociation, we performed a series of MQC MD simulations, the computational specifics of which are summarized in the methods section below and detailed in the Supporting Information (SI). Briefly, we treat the Na_2^+ molecule as two classical Na^+ cores that are held together by a single quantum mechanical valence bonding electron. We utilize previously-developed pseudopotentials[56] to describe the interaction between the bonding electron and the Na^+ cores[62] and 254 THF molecules[59, 64, 81] or 1600 Ar[57] atoms, and solve the Schrödinger equation for the electron in a basis of 32^3 grid points in Ar and 64^3 grid points in THF. This methodology reproduces gas-phase quantum chemistry calculations quite well,[62, 80] and also has successfully reproduced the experimental properties of sodium cation:solvated electron tight-contact pairs in THF.[63, 64] Here, we calculate the behavior of the Na_2^+ molecule in 120 K liquid Ar at a density of 1.26 g/mL, well in the liquid region of the phase diagram, and at 298 K in liquid THF at the experimental density at 1 atm of 0.89 g/mL.

First we generated PMFs where the solvent in is equilibrium with the solute by holding the Na–Na bond length at fixed distances through the application of an umbrella potential[82] centered at the bond distance of interest; we let the condensed-phase system equilibrate at each distance, and then calculated the average energy while running the system on both the ground and first excited electronic states. Stitching together these energies as a function of distance using the MBAR method[83] produced PMFs, which are shown in Fig. 2.1, where the solvent is equilibrium with the solute. One question is whether the excited-state PMF can be generated while the solvent is in equilibrium with the solute's ground state and vice-versa. In other words, are the solvent structures and fluctuations associated with the two solute electronic states similar enough that the PMFs are independent of which electronic state we choose?

The black curves in Fig. 2.1 show the ground- and first excited-state potential energy surfaces of the Na_2^+ molecule in the gas phase calculated with our MQC methodology; the curves do an excellent job reproducing the known potential energy surfaces of this molecule, including the ground state vibrational frequency, bond dissociation energy, and the lowest-energy electronic absorption.[80] The solid, colored curves in Fig. 2.1 show the ground- (blue solid triangles) and first excited-state

(red solid diamonds) PMFs for Na_2^+ in Ar (panel a) and in THF (panel b) calculated with the solvent at equilibrium with the solute occupying the electronic state under investigation. The data in Fig. 2.1a show that on the Na_2^+ electronic ground state, compared to the gas phase, interactions with liquid Ar lead to a shorter equilibrium bond length (3.74 Å in Ar vs. 3.84 Å in the gas phase) and a higher Na–Na vibrational frequency (134 cm^{-1} in Ar vs. 113 cm^{-1} in the gas phase), much like we observed previously for the Na_2 molecule.[60, 61, 66] The red solid diamonds show that when the molecule is placed on the electronic excited state, the PMF is nearly identical to the potential energy surface in the gas phase, indicating that the equilibrium excited-state solvent interactions are small compared to the intrinsic gas-phase energy.

The dashed, colored curves in Fig. 2.1a test whether PMFs for one solute electronic state can be predicted when the solute resides in a different electronic state. The blue open triangles show the Na_2^+ first excited state while the solvent is equilibrated with the electronic ground state; this prediction yields a dissociative surface that is raised in energy relative to the gas phase because when the solvent is equilibrated around the ground-state solute, it is in an unfavorable geometry for solvating the solute excited state. The red open diamonds show that when the solvent is equilibrated for the solute's excited state, there is a significant de-solvation and thus increase in energy and decreased vibrational frequency of the ground electronic state. Thus, as might be expected, we cannot accurately predict the excited-state PMF while the solute resides in its electronic ground state because the way the solvent equilibrates around one solute electronic state destabilizes the other electronic state.

Although the PMFs for Na_2^+ in Ar are qualitatively similar to the gas-phase potentials, the situation turns out to be completely different for Na_2^+ in liquid THF. In previous work, we found that the oxygen atoms on THF make weak dative bonds with the Na^+ cores inside the Na_2^+ molecule.[60, 61] These dative bond interactions are only about the same strength as a hydrogen bond ($\sim$4 kcal/mol), but they cause the bonding electron density to be pushed out of the internuclear region, leading to a significant increase in bond length (the bond length changes from 3.84 Å in the gas phase to 5.24 Å in liquid THF) and a factor of $\sim$3 decrease in both vibrational frequency (from 113 cm^{-1} to 42 cm^{-1}) and bond dissociation energy (from 0.92 eV in the gas phase to 0.23 eV in THF).[60] We also found that the dative bonding interactions stabilize the Na_2^+ solute in two primary coordination states: $Na(THF)_4$-$Na(THF)_5^+$ and $Na(THF)_5$-$Na(THF)_5^+$. These coordination

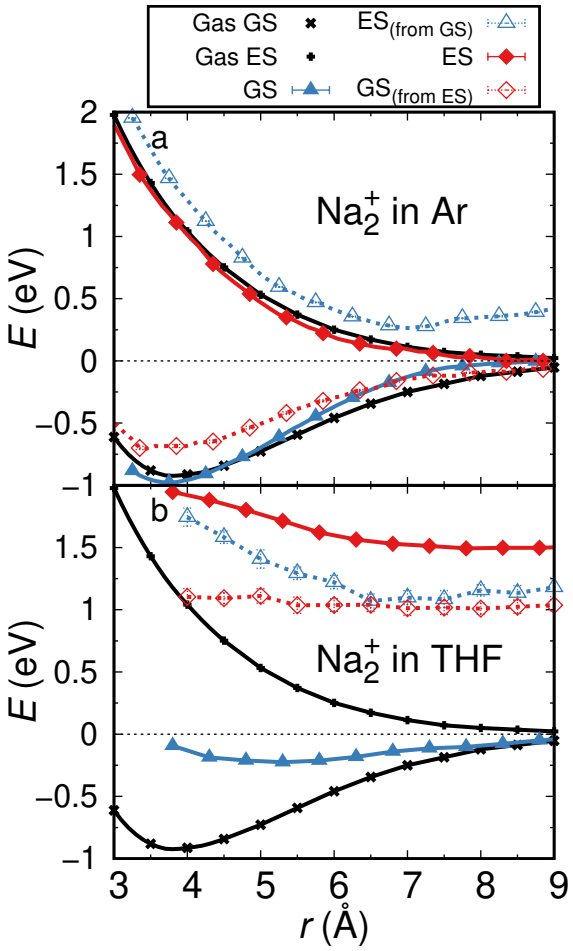

Figure 2.1: Potentials of mean force for the Na_2^+ molecule in Ar and $Na_2(THF)_n^+$ in THF. The Na_2^+ gas-phase potential energy surfaces are plotted as the black curves. The condensed-phase PMFs are plotted as solid blue triangles for the ground state, solid red diamonds for the excited state, dashed blue curves for the excited state calculated while propagating the solvent dynamics on the ground state, and dashed red curves for the ground state calculated while propagating the solvent dynamics on the excited state. Panel (a) shows the PMFs for Na_2^+ in Ar while panel (b) shows the results in THF. A comparison of the solid and dashed curves shows that the solvent structures are different on the ground and excited electronic states so that the PMF for the excited state cannot be generated from studying equilibrium configurations on the ground state.

states behave as distinct molecules whose chemical identity is different both from gas-phase Na_2^+ and from each other; the two coordination states are in equilibrium with each other and have to surmount a barrier of $\sim 8\ k_B T$ to interconvert.[60] Each coordination state has its own bond length, vibrational frequency and dissociation energy. In other words, in THF, the solvent has integrated itself as part of the chemical identity of two different Na_2^+-based solutes.[61]

Figure 2.1b shows that because of the change in chemical identity from Na_2^+ to Na_2^+:$(THF)_n$, the PMFs for the Na_2^+ molecule in THF are entirely different than those in the gas phase or in liquid Ar. Furthermore, comparison of the solid and dashed curves show that the ground- and excited-state solvent structures are dramatically different from one another. Surprisingly, the most prominent feature in Fig. 2.1b is that unlike in the gas phase or liquid Ar, the excited-state PMF for Na_2^+ solvation on the excited state (solid red diamonds) in THF is hardly dissociative.

To test the ability of PMFs in predicting photodissociation dynamics, we used the time integral of work formalism[32] to describe the actual potential energy surface followed during the nonequilibrium dynamics. We ran a series of nonequilibrium trajectories, 15 in Ar and 20 in THF, starting from equilibrated configurations near the PMF minimum in the Na_2^+ electronic ground state ($\sim$3.7 Å in Ar; $\sim$5.4 Å in THF), and then placed the molecule on the electronic excited state to simulate photoexcitation. We then calculated the effective potential surface on which the excited Na_2^+ moved during nonequilibrium dissociation by:

$$U(t) = -\int_{t_0}^{t} F(t) \cdot v(t) dt, \tag{2.1}$$

where $F(t)$ is the total force (from the solute and solvent) on the Na nuclei along the bond axis, $v(t)$ is the bond velocity, and t_0 is the time at which photoexcitation takes place. Since we know the trajectory that the dissociating molecule takes, $r(t)$, we can parametrically combine $U(t)$ and $r(t)$ to produce an effective energy surface followed during the dynamics, $U(r)$, as described in the SI. The time t in Eq. 2.1 is chosen to range up to $\sim$300 fs in liquid Ar and to $\sim$1000 fs in liquid THF, which is long enough to have sampled all the appropriate photodissociation dynamics but short enough to avoid diffusive recrossings that occur at longer times.

In this paper, we refer to the nonequilibrium $U(r)$ as a 'dynamical energy surface'; by construction, this energy surface incorporates the actual nonequilibrium dynamics followed during the

chemical reaction without any assumptions regarding the gas-phase potential energy surfaces or maintaining equilibrium with the solvent. Our use of a dynamical energy surface in this instance was inspired by the work of Zanuttini et al., who studied the connection of solvent collisions to photodissociation pathways.[10] The nonequilibrium ensemble-averaged dynamical energy surface following photoexcitation of Na_2^+ in both liquid Ar and liquid THF are shown as the green curves in Fig. 2.2. The raw trajectory data used to calculate the dynamical energy surfaces are shown in the SI for reference.

Figure 2.2a shows that following the initial excitation, the dynamical energy surface for Na_2^+ in liquid Ar has a slope that is quite similar to that in the gas phase, which is also very similar to the PMF. This is in agreement with prior work studying diatomic photodissociation in rare-gas solids.[6, 10, 27] But after the first ∼1 Å (∼60 fs) of separation, the dynamical energy surface in liquid Ar shows a positive slope; this occurs at exactly the internuclear distance at which the expanding Na_2^+ molecule collides with the first-shell solvent atoms; in the nonequilibrium dynamics, there is always a collision with the first solvent shell that exerts a force on the expanding molecule back towards shorter bond distances. By ∼7 Å (∼200 fs), the slope of the dynamical energy surface has decreased to roughly zero, indicating that the dissociated solute has on average escaped the solvent cage and that the dynamics are now governed more by diffusion than the electronic structure of Na_2^+. Clearly, neither the gas-phase surfaces nor the PMFs capture the dissociation dynamics of Na_2^+ in Ar because they do not capture solvent caging, which is by necessity a nonequilibrium effect: there are no strong directional collisions like this at equilibrium.

The green curve in Fig. 2.2b shows the dynamical energy surface following photoexcitation of Na_2^+ in liquid THF. The dynamical energy surface displays two main features: a small initial 'dip' at an internuclear separation of ∼5.6 Å, followed by a general increase in energy at longer distances. What this dynamical energy surface shows is that following photoexcitation, the Na_2^+ species elongates but does not dissociate; the details of what causes this will be discussed below. The nonequilibrium dynamical energy surface shows a strong contrast to both the gas-phase (black curve) potential surface and the excited-state PMF (red diamonds), both of which predict that the molecule should dissociate.

To understand why gas-phase surfaces and PMFs fail in such different fashions for the photodissociation of Na_2^+ in liquid Ar and liquid THF, we next turn to exploring the nonequilibrium

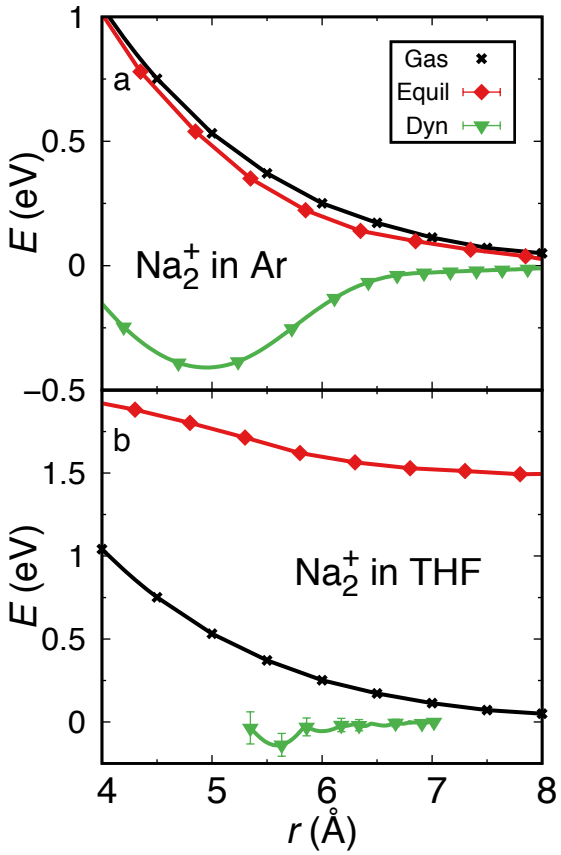

Figure 2.2: Dynamical energy surfaces reveal the shortcomings of gas-phase surfaces and equilibrium-based potentials of mean force for the photodissociation of Na_2^+ in solution. The potential energy surface for the first excited state of gas-phase Na_2^+ (black crosses) and the PMF for the electronic excited state (red diamonds) are the same curves as in Fig. 2.1; the dynamical energy surface calculated from nonequilibrium trajectories parametrically with $r(t)$ using Eq. 2.1 (green triangles) is shown for Na_2^+ in Ar (panel a) and in THF (panel b). The dynamical energy surfaces show clear solvent-induced nonequilibrium features of the Na_2^+ dissociation reaction. In Ar, the well at ∼5 Å in the dynamical energy surface is the result of nonequilibrium caging by the surrounding solvent, as explored further in Fig. 2.3, below, while the gradual upward slope of the dynamical energy surface in THF comes from changes in the electronic structure and chemical identity of Na_2^+ in this solvent, as detailed in Figs. 4 and 5, below.

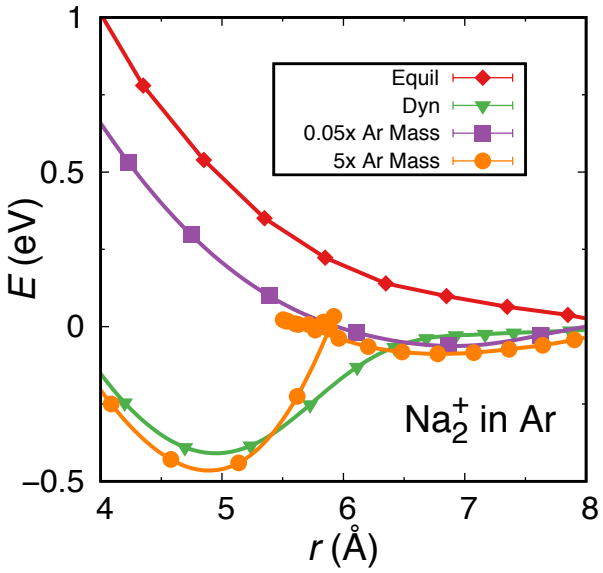

Figure 2.3: Dynamical energy surfaces from nonequilibrium simulations (computed via Eq. 2.1 parametrically with $r(t)$; see the SI) of the photodissociation of Na_2^+ in liquid Ar as a function of the Ar mass reveal that the magnitude of solvent caging is dependent on the timescale of the solvent fluctuations. When the Ar mass is divided by 20 (purple squares) and increased by a factor of 5 (orange circles) but the intermolecular potentials are left unchanged from the original simulations (green triangles, same curve as in Fig. 2.2a), there are significant changes in the dynamical energy surface. For comparison, the excited-state PMF is shown as the red diamonds (same curve as in Fig. 2.1a). When the solvent mass is reduced to the point where fluctuations occur on a timescale comparable to the Na_2^+ photodissociation dynamics, the dynamical energy surface begins to resemble the PMF. When the solvent mass is increased, however, the initial collision with the solvent cage knocks the photofragments back with much greater force, dynamics that are not seen at equilibrium. This leads to a temporary shortening of the Na–Na bond length before the fragments ultimately escape the solvent, creating the loop in the dynamical energy surface near 5.8 Å.

behavior in each solvent in more detail. In liquid Ar, the dissociation dynamics involves a strong interaction of the photofragments with the Ar solvent cage that does not occur at equilibrium. This leads to the question of whether an equilibrium approach could ever capture this type of caging event. To explore this, we tuned the timescale of the Ar solvent fluctuations by artificially changing the Ar mass while leaving all the intermolecular potentials unchanged; this means that the equilibrium solvation structures do not change, but the timescale for equilibration does. We then ran nonequilibrium trajectories with the altered solvent mass. Figure 2.3 shows that when the mass of the Ar atoms is reduced by a factor of 20 (purple squares) such that the Ar atoms are an order of magnitude lighter than the Na^+ cores, the dynamical energy surface now strongly resembles the PMF (red diamonds). The solvent in this case is so light that the dissociating Na_2^+ molecule can easily push the nearby atoms aside, removing the 'caging' event that dominated the dynamics when the Ar had its full mass. In other words, the artificially lighter Ar solvent can equilibrate on a timescale comparable to the time it takes photoexcited Na_2^+ to dissociate, so that an equilibrium approach predicts the nonequilibrium dynamics reasonably well.

Figure 2.3 also explores the other extreme, where the mass of the Ar solvent atoms is increased by a factor of five (orange curve) such that the Ar atoms are 10 times heavier than the Na^+ cores. Now the 'cage effect' is exaggerated, as the dynamical energy surface shows not only a stronger reflection, but actually a small loop at internuclear separations near 5.8 Å, the result of the fact that the dissociating Na_2^+ solute has to undergo multiple bounces before being able to escape the surrounding solvent cage, as seen experimentally for I_2 in solid rare gas matrices.[7] Thus, even in a simple, non-interacting solvent like liquid Ar, an equilibrium picture will fail to describe photodissociation reactions when the timescale of dissociation is faster than the intrinsic timescale of the solvent fluctuations.

To better visualize the solvent caging in this system, Fig. 3.5 shows plots of the average solvent positions around Na_2^+ in liquid Ar as a function of Na–Na distance both at equilibrium, panel (a), and during the nonequilibrium photodissociation dynamics, panel (b). The plots show an isosurface at solvent distances at about the van der Waals size of the solute molecule, ∼3.3 Å from each Na^+ nucleus; the color represents the cylindrically-averaged probability of finding a solvent atom at that point on the surface relative to the bulk solvent density. The red color indicates that more Ar is present than the average density, white color shows about an average amount of solvent, while blue

color shows a deficit of solvent at that position. The points are evenly spaced so that the color density provides an accurate representation of the spatial density of solvent atoms.

The left-most plots compare the solvent distribution around Na_2^+ in Ar at equilibrium on the excited state (panel a) and at equilibrium on the ground state (panel b, which has a ground-state solvent configuration because it shows the Franck-Condon excited solute before the solvent has had time to move). Clearly, the equilibrium ground- and excited-state solvation structures are different. When the Na–Na bond is separated by 3.5 Å and 5.5 Å at equilibrium on the excited state (left and center plot in panel a), there is a clear preference for the solvent to reside near the 'neck' of the molecule, as the excited-state electron density has a node between the two atoms, causing the solvent to move into this region to maximize ion-induced dipole interactions. During the nonequilibrium dynamics, however, the center plot of panel b shows that there is a deficit of solvent in the neck region and an excess of solvent at the ends of the molecule as it encounters the solvent cage. The solvent has not had time during the ∼80 fs since excitation to move into the neck region or away from the ends of the dissociating molecule, showing the caging is what causes the positive slope in this region of the dynamical energy surface. The memory of photoexcitation persists even as the molecule separates to 8 Å, which is 260 fs after excitation, as evidenced by the deficit of solvent on the inside of the bond in the right plot of panel b compared to the excited-state equilibrium prediction in panel a.

Unlike in liquid Ar, where the dynamical energy surface approaches the PMF and the gas-phase potential energy curve when the solvent fluctuates on fast timescales compared to the molecular dissociation, the dynamical energy surface for the photodissociation of Na_2^+ in liquid THF looks completely different because the chemical identity of the Na_2^+ molecule is intricately linked with its local solvent environment, such that the solute is better thought of as Na_2^+:$(THF)_n$ complexes.[60, 61] To understand how the complexation by the solvent affects dissociation, we turn to Figs. 4c and d (left), which shows that when Na_2^+:$(THF)_n$ is initially photoexcited to its lowest energy excited state, the node in the electron density lies oriented along the bond axis: the electronic structure resembles that of a molecular π bonding orbital rather than the σ^* antibonding orbital seen with gas-phase Na_2^+ or Na_2^+ in liquid Ar (see SI).[60] This is a reflection of the fact that the coordination complex in liquid THF is truly a different molecule with a different chemical identity from the gas-phase Na_2^+ species, leading to a very different electronic structure.

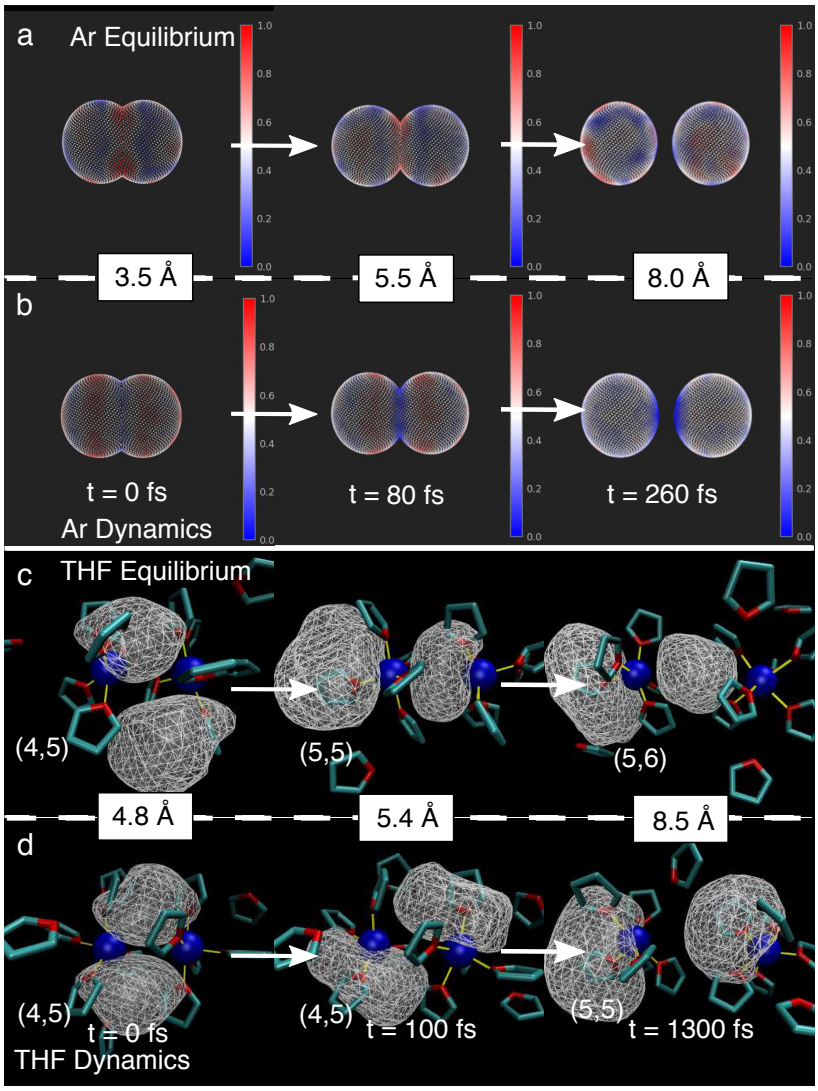

Figure 2.4: Representative solvent distributions around excited-state Na_2^+ at equilibrium, panel a, and during nonequilibrium dynamics, panel b, in liquid Ar. The surfaces are ∼3.3 Å from the Na^+ cores and colored to show the relative solvent density at that distance (bulk - white, red - excess, blue - deficit). During nonequilibrium dynamics, there is a larger chance of finding axial Ar and a smaller chance of finding equatorial Ar than at equilibrium, providing a direct visualization of caging. Corresponding representative snapshots of excited-state $Na(THF)_4$-$Na(THF)_5^+$ in liquid THF are shown at equilibrium, panel c, and during the nonequilibrium dynamics, panel d. Na^+ cores are plotted as blue spheres and THF as turquoise sticks with red O atoms. The bonding electron is drawn as a wire mesh containing 75% of the charge density. Following photoexcitation, the bonding electron density has its node oriented along the bond axis; however, rotation of the node (cf. Fig. 2.5b, below) occurs differently at equilibrium (panel c) than following photoexcitation (panel d). The coordination of the Na_2^+ species by THF also changes differently at equilibrium and during the nonequilibrium dynamics (cf. Fig. 2.5a).

If we start from a $Na(THF)_4$-$Na(THF)_5^+$ configuration, as in Fig. 3.5, the solute begins its dissociation process from its equilibrium ground state distance of ∼4.8 Å.[60] Following photoexcitation, the solute's Na–Na bond distance increases to ∼5.4 Å after approximately 100 fs, but the electronic structure at this time (Fig. 3.5d, center) is clearly very different than the equilibrium structure at the same distance (Fig. 3.5c, center). The equilibrium picture when the bond length reaches this distance has the node of the electronic wavefunction perpendicular to the bond, creating a dissociative force. But the node in the wavefunction during the nonequilibrium dynamics is not able to fully rotate from parallel (in the Franck-Condon region) to perpendicular to the Na–Na bond. The rotation of the excited-state node requires significant rearrangement of the datively-bonded THF molecules; there is simply insufficient time following excitation for these THFs to have reached their equilibrium stable orientation. Finally, even 1.3 ps after photoexcitation, the molecule is still not able to dynamically reach distances past 8.5 Å; this is because significant electron density remains between the nuclei, holding the molecule together. This is what is responsible for the weak positive slope in the dynamical energy surface at long distances seen in Fig. 2.2b: even though the molecule would prefer to dissociate at equilibrium, there is no easy kinetic pathway to achieve dissociation following the actual photoexcitation.

In addition to the inability of the excited-state wavefunction to achieve the correct configuration for dissociation, there is a second reason the dynamical energy surface for the photodissociation of Na_2^+ in liquid THF looks so different: the chemical identity of the molecule changes during photodissociation in a way that cannot be accounted for in the gas phase or at equilibrium. At the Franck-Condon ground-state equilibrium distance, the molecule prefers to reside in the $Na(THF)_4$-$Na(THF)_5^+$ coordination state. As the Na–Na distance is increased at equilibrium on the excited state, Fig. 3.5c shows that the coordination state changes to predominantly $Na(THF)_5$-$Na(THF)_5^+$ by 5.4 Å and to the $Na(THF)_5$-$Na(THF)_6^+$ state by 8.5 Å, the result of the extra space available to form additional dative bonds, which are shown as yellow lines. However, during the photodissociation process, Fig. 3.5d shows that there has been insufficient rearrangement of the coordination complex to allow an additional dative bond to form when the Na–Na distance reaches 5.4 Å, and only a single additional dative bond can form by 8.5 Å instead of the two extra dative bonds seen at equilibrium. The insertion of the last dative bond is what is critical to allowing the molecule to fully dissociate, as this is what weakens the bonding electron's association with the more-coordinated

sodium core.

To better visualize how the dynamical energy surface describes the photodissociation of Na_2^+ in THF, Fig. 2.5a plots the number of solvent molecules forming dative bonds with each Na^+ core as a function of the Na–Na bond distance, both at equilibrium on the excited state (red curves) and during the nonequilibrium dynamics (green curves). The dashed curves in this figure show the average number of THF dative bonds to the lesser-coordinated sodium core (referred to as Na_a) while the solid curves show the number of dative bonds around the more-coordinated sodium core (referred to as Na_b). At equilibrium on the excited state, there are two transitions to new coordination states, a $Na(THF)_4$-$Na(THF)_5^+ \rightarrow Na(THF)_5$-$Na(THF)_5^+$ transition around 5.5 Å and a $Na(THF)_5$-$Na(THF)_5^+ \rightarrow Na(THF)_5$-$Na(THF)_6^+$ transition around 8.5 Å, as visualized in the snapshots in Fig. 3.5c. However, the photodissociation dynamics shows only the first of these transitions (which is not complete until a distance of nearly 7 Å), in concordance with the snapshots shown in Fig. 3.5d.

Figure 2.5b provides a way to understand how the electronic structure changes at equilibrium and during nonequilibrium dissociation. The plot shows the angle of the node in the excited electronic wavefunction with respect to the Na–Na bond axis, calculated as an ensemble-averaged dot product of the gas-phase Franck-Condon excited state at the equilibrium ground-state distance with the equilibrium (red diamonds, equilibrated on the excited state) or dynamic (green triangles) excited state at other Na–Na distances. As such, a 'node orientation' of zero indicates that the node is perfectly parallel with the Na–Na bond axis while a value of one means that the node is perfectly perpendicular to the Na–Na bond axis. Figure 2.5b shows that at equilibrium, the node is able to fully rotate at much lower Na–Na bond distances (∼5.5 Å); whereas, the node does not fully rotate until ∼7 Å in the photodissociation dynamics. Following photoexcitation, the datively-bonded THFs do not have time to move to an appropriate position to allow the node to rotate.

The changes in the Na_2^+ chemical identity coupled with the changes in the electronic structure of the bonding electron during the nonequilibrium dissociation of Na_2^+ in THF explain the behavior of the dynamical energy surface shown in Fig. 2.2b. The preliminary 'dip' in the dynamical energy surface arises because upon photoexcitation, the bonding electron's wavefunction must orient on the fly from a π-like to a σ^*-like electronic structure; in addition, the molecule must potentially change

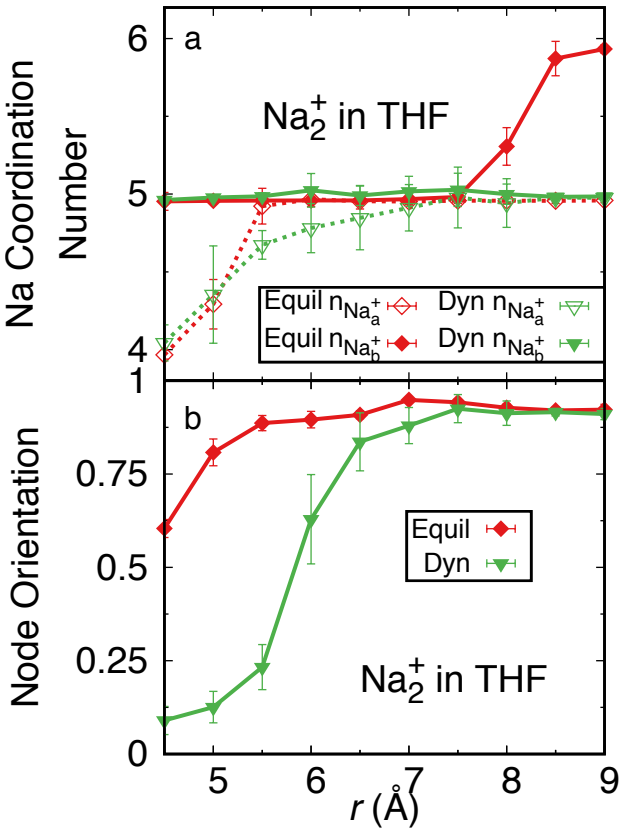

Figure 2.5: Changes in the $Na_2(THF)_n^+$ chemical identity (i.e., THF coordination number) and the orientation of the bonding electron density explain the dynamical energy surface for the photodissociation of Na_2^+ in THF. Panel a plots the THF dative bond coordination number around each sodium core (more coordinated Na^+, solid curves; less coordinated Na^+, dashed curves) as a function of Na–Na bond length at equilibrium (red) and during the dynamical, nonequilibrium dissociation (green); there is insufficient time for the coordination number to change during the nonequilibrium dynamics to match the equilibrium prediction. Panel b shows the orientation of the excited-state bonding electron's node for at equilibrium (red) and during the dynamical, nonequilibrium dissociation (green) as a function of Na–Na bond length. Clearly, the node rotation is hindered during the nonequilibrium dynamics compared to what happens at equilibrium as a function of Na–Na distance. Together, the inability for the node to rotate and the coordination number to change during dynamics hamper dissociation as reflected in the dynamical energy surface.

chemical identity through the formation of new Na–THF oxygen-site dative bonds. However, these processes consume the energy the molecule needs to form the final dative bond that at equilibrium takes the loosely-bound $Na(THF)_5$-$Na(THF)_5^+$ state to the $Na(THF)_5$-$Na(THF)_6^+$ state allowing the bond to break. This leaves the nonequilibrium molecule without an easy kinetic pathway to dissociate until sufficient time has passed for equilibration to occur.

2.3 Conclusions

In summary, through MQC MD simulations of Na_2^+ in the condensed phase, we have shown that nonequilibrium solvent effects are necessary for thinking about photodissociation dynamics and that there are a variety of such effects to consider even for the same solute in different environments. We demonstrated that a dynamical energy surface can be constructed to capture the nonequilibrium solvent effects needed to think about the photodissociation dynamics of Na_2^+ in Ar and in THF. In liquid Ar, the dynamical energy surface directly captures the initial collision of the dissociating molecule with the surrounding cage of Ar atoms. This singular event is reminiscent of the single-collision that causes a breakdown of linear response in photofragment rotational dynamics.[36, 45] The cage effect is clearly dynamical, as it depends on the magnitude of the solvent's mass: heavier masses amplify the bounce-back of the photofragments upon collision with the solvent cage, while sufficiently light masses lead to better agreement with the PMF because the lighter solvent can equilibrate on the timescale of the dissociation dynamics. In liquid THF, the dynamical energy surface reveals that photoexcitation of Na_2^+ leads to a kinetic trap that originates from solvent-induced changes in the Na_2^+ molecule's chemical identity and electronic structure. During dynamical, nonequilibrium dissociation, the solute is unable to re-orient its bonding electron density from the π-bonding-like state created initially upon photoexcitation to the more σ*-like state that is needed for dissociation. In addition, there is not sufficient time following photoexcitation for the molecule to undergo the change in chemical identity via the creation of new dative bonds with the solvent, which is also needed for the bond to fully break. All of this work shows that understanding nonequilibrium solvent effects is important for thinking about solution-phase photodissociation dynamics and that an appropriately constructed dynamical energy surface captures a variety of solvent effects that affect the nonequilibrium dynamics in different ways.

2.4 Overview of Simulation Details

The work in this paper consists of mixed quantum classical (MQC) molecular dynamics (MD) simulations of Na_2^+ in the condensed phase. In these simulations, which were performed in the microcanonical ensemble, we treated the Na_2^+ molecule as two classical Na^+ cores held together by a single quantum-mechanically-treated valence bonding electron plus hundreds of classical solvent molecules. The interactions between the classical particles and the quantum mechanical electron were accounted for using Phillips-Kleinman (PK) pseudopotentials,[55] modified with polarization potentials to correct for the frozen-core approximation implicit in the PK formalism. These pseudopotentials, which are identical to those used in our previous studies,[58–62, 66] are described in more detail in the SI. The classical interactions between the Na^+ cations and the Ar and rigid OPLS THF solvent molecules were modeled with the same potentials used in our earlier studies in these solvents[60, 66] and are detailed in the SI.

The cubic simulation cells had a side length of 43.8 Å for simulations in Ar and 32.5 Å for those in THF, which given the number of solvent molecules yielded densities of 1.26 g/mL at 120 K for Ar 0.89 g/mL at ∼298 K for THF. In Ar, we expanded the electronic eigenstates of the quantum mechanical electron in a basis of 32 × 32 × 32 plane waves over a 25 $Å^3$ box. Due to the diffuse nature of the valence electron's excited state in THF, particularly at larger Na–Na distances, we used 64 × 64 × 64 plane waves that spanned the entire cubic simulation cell. For all simulations, we utilized periodic boundary conditions with the minimum image convention.[82] All interactions in the cell were tapered smoothly to zero at 16 Å over a 2-Å range using a center-of-mass-based switching function.[84] The single-electron Hamiltonian, which is shown explicitely in the SI, was diagonalized at every MD time step using the implicitly-restarted Lanczos method as implemented in ARPACK.[85] For simulations in THF, the solvent molecules were treated as rigid, planar five-membered rings following the work of Chandrasekar and Jorgensen.[86] All simulations were propagated using the velocity Verlet algorithm[82] with a 4-fs time step, except for simulations with light Ar in which case a 2-fs time step was used.

We performed both equilibrium umbrella sampling, where the Na_2^+ bond length was restrained on either the ground or first excited electronic state, and nonequilibrium dissociation trajectories, where the molecule was placed into the excited state from its equilibrium ground state configuration

and then propagated adiabatically on its electronic excited state. For umbrella sampling in Ar, bins were set at every 0.1 Å from 3.0 Å out to a dissociative distance of 9.0 Å. For umbrella sampling in THF, bins were set every 0.1 Å from 4.0 Å out to a dissociative distance of 10.0 Å. Within each bin after appropriate equilibration, umbrella trajectories were run for 10 ps to ensure ample statistics across the potential of mean force. Details of the umbrella sampling and the MBAR process used to stitch the individual umbrella sampled windows together to create the PMFs shown in Fig. 1 are given in the SI. For the nonequilibrium trajectories, the Na_2^+ molecule was placed in the first excited state starting from uncorrelated ground-state configurations taken from an equilibrated ground-state trajectory; 15 nonequilibrium trajectories were run in Ar and 20 nonequilibrium trajectories were run in THF to provide statistics for nonequilibrium ensemble averages. Details of the initial configurations chosen for these studies as well as the process used to construct the PMFs and dynamical energy surfaces shown in Fig. 1 and 2 are provided in the SI.

2.5 Supplementary Information

2.5.1 Simulation Details

Mixed Quantum/Classical Model

Our mixed quantum/classical (MQC) molecular dynamics (MD) simulations consisted of two classical Na^+ cations, one fully quantum mechanical electron, and hundreds of classical solvent molecules. Simulations in liquid argon (Ar) contained 1600 Ar atoms in a simulation cell with a side length of 43.8 Å, and simulations in liquid tetrahydrofuran (THF) contained 254 THF molecules in a 32.5 Å simulation cell. The sizes of the simulation cells were chosen to reproduce the appropriate solvent densities at the simulation temperatures (1.26 g/mL at 120 ± 2 K for Ar simulations, which is well within the liquid region of simulated Ar's phase diagram[87] and 0.89 g/mL at 298 ± 6 K for THF simulations). For simulations in THF, the solvent molecules were treated as rigid, planar five-membered rings following the work of Chandrasekar and Jorgensen.[86] This rigid planarity was enforced using the RATTLE algorithm, as in our previous MQC MD work.[61, 64] In all simulations, periodic boundary conditions were implemented with minimum image convention[82] and all interactions were tapered smoothly to zero at 16 Å over a 2 Å range with a center of

mass-based switching function according to Steinhauser.[84] All simulations were performed in the microcanonical ensemble.

Because all interactions were taken to be pair-wise additive, the full Hamiltonian of the system is $\hat{H} = H^{\mathrm{cl}} + \hat{H}^{\mathrm{qm}}$. In atomic units, the classical portion of the Hamiltonian is given by

$$H^{\mathrm{cl}} = \frac{1}{2} m_{\mathrm{Na^+}} \sum_{i=1}^{2} v_{\mathrm{Na^+}_i}^2 + \frac{1}{2} m_{\mathrm{solv}} \sum_{i=1}^{n_{\mathrm{solv}}} v_{\mathrm{solv}_i}^2 + U^{\mathrm{Na^+-Na^+}}(|\boldsymbol{R}_{\mathrm{Na^+}_1} - \boldsymbol{R}_{\mathrm{Na^+}_2}|) + \sum_{i=1}^{n_{\mathrm{solv}}} \sum_{j>i}^{n_{\mathrm{solv}}} U^{\mathrm{solv-solv}}(|\boldsymbol{R}_{\mathrm{solv}_i} - \boldsymbol{R}_{\mathrm{solv}_j}|) + \sum_{i=1}^{2} \sum_{j=1}^{n_{\mathrm{solv}}} U^{\mathrm{Na^+-solv}}(|\boldsymbol{R}_{\mathrm{Na^+}_i} - \boldsymbol{R}_{\mathrm{solv}_j}|) \quad (2.2)$$

where $v_{\chi_{\mathrm{i}}}$ is the velocity of the i^{th} sodium ($\chi = \mathrm{Na^+}$) or solvent molecule ($\chi = \mathrm{solv}$) at position $\boldsymbol{R}_{\chi i}$ and mass m_χ. $U^{\chi-\gamma}$ is a classical potential between atom types χ and γ ($\chi, \gamma = \mathrm{Na^+}$ or solv).

The quantum Hamiltonian is given by

$$\hat{H}^{\mathrm{qm}} = \sum_{i=1}^{2} \frac{\hat{\boldsymbol{p}}_i^2}{2} + \sum_{i=1}^{2} \sum_{j=1}^{2} V^{\mathrm{Na^+}}(|\boldsymbol{R}_{\mathrm{Na^+}_j} - \hat{\boldsymbol{r}}_i|) + \sum_{i=1}^{2} \sum_{j=1}^{n_{\mathrm{solv}}} V^{\mathrm{solv}}(|\boldsymbol{R}_{\mathrm{solv}_j} - \hat{\boldsymbol{r}}_i|) \quad (2.3)$$

where $\hat{\boldsymbol{p}}_i$ and $\hat{\boldsymbol{r}}_i$ are the momentum and position operators for electron i, respectively, and V^χ is the pseudopotential representing the interaction between an electron and atom type χ.

For the MQC studies, the classical interaction between the two $\mathrm{Na^+}$ cations was modeled through a point-charge Coulomb potential, $U^{\mathrm{Na^+-Na^+}}(R) = 1/R$, since the short-range repulsion between the cores is negligible around the internuclear separation of $\mathrm{Na_2^+}$.

The $\mathrm{Na^+}$-Ar interaction was taken from a fit to the *ab initio* calculations of Ahmadi, Almlöf, and Røeggen[88]:

$$U^{\mathrm{Na^+-Ar}}(R) = \frac{a_1 \exp(-a_2 R)}{R} - \frac{2}{1 + a_1 \exp(a_3/R)} \left(\frac{C_6}{R^6} + \frac{C_8}{R^8} \right) \quad (2.4)$$

where $a_1 = 242.32$ Hartree, $a_2 = 1.67$ bohr^{-1}, $a_3 = 5.6$ bohr, $C_6 = 255$ bohr^5, and $C_8 = 4410$ bohr^7. Following Gervais et al,[57] we have subtracted the charge-dipole term, which goes as $-0.5\alpha_{\mathrm{Ar}}/R^4$, where α_{Ar} is the dipole polarizability of Ar.

All other classical interactions were modeled with Lennard-Jones potentials:[82]

$$u_{ij}(r_{ij}) = \frac{1}{4\pi\epsilon_0}\frac{q_i q_j}{r_{ij}} + 4\epsilon_{ij}\left[\left(\frac{\sigma_{ij}}{r_{ij}}\right)^{12} - \left(\frac{\sigma_{ij}}{r_{ij}}\right)^{6}\right] \tag{2.5}$$

where r_{ij} is the distance between the i^{th} and j^{th} solvent/Na^+ site, q_i is the charge on the i^{th} site, ϵ_{ij} is the potential well depth, and σ_{ij} is the finite distance at which the inter-particle potential is zero. The Lennard-Jones parameters used in this study are listed in Supplementary Table 1. The standard Lorentz-Berthelot combining rules were also used to calculate the solute-solvent site and solvent site-solvent site interactions in THF.[82]

	σ (Å)	ϵ (kJ/mol)	q (e)
Argon	3.405	0.996	0.0
THF-oxygen	3.0	0.71	–0.5
THF-α-methyl	3.8	0.49	+0.25
THF-β-methyl	3.905	0.49	0.0
Na^+	1.67	22.07	+1.0

Table 2.1: **Lennard-Jones and Coulomb Potential Parameters for the Solute-Solvent Systems Studied in This Work.**

Phillips Kleinman (PK) pseudopotentials were used to account for the interactions between the classical particles and the quantum mechanical electrons.[55] These PK potentials were modified with polarization potentials to correct for the frozen core approximation implicit in PK formalism.[58, 59, 89] For the electron-Ar interaction, $V^{e^- - \text{Ar}}$, we used a modified version of the pseudopotential developed by Gervais *et al*,[57] described in detail in our previous work.[66] For $V^{e^- - \text{Na}^+}$ and $V^{e^- - \text{THF}}$, we used rigorously-derived psedopotentials previously developed by our group, the details of which can be found in Refs. 58 and 59, respectively. The final pseudopotential fits are presented here in Supplementary Tables 2 and 3.

Simulation Setup

The eigenstates of the quantum mechanical valence bonding electron were expanded on a three dimensional grid. For simulations in Ar, we used a basis of 32 × 32 × 32 grid points distributed over a 25 Å^3 box. Because the valence electron is more diffuse in THF, for simulations in THF, we used a larger grid that spanned the entire simulation cell and contained 64 × 64 × 64 grid points.

i	c_i (a.u.)	α_i (a.u.)
1	-16.3145	0.124293
2	0.0455219	0.0322129
3	16.3213 81	0.124181

Table 2.2: **Parameters used in the construction of the sodium-electron pseudopotential,** $\phi(r) = \sum_{i=1}^{3} c_i e^{-\alpha_i r^2}$**.** Further details of the sodium-electron pseupotential can be found in Ref 58.

$$U_{fit}(\mathbf{r}) = \begin{cases} & U_o + U_{c\alpha 1} + U_{c\alpha 2} + U_{c\beta 1} + U_{c\beta 2} \\ + & U_{h\alpha 1} + U_{h\alpha 2} + U_{h\alpha 3} + U_{h\alpha 4} + U_{h\beta 1} \\ + & U_{h\beta 2} + U_{h\beta 3} + U_{h\beta 4} + U_{ao} + U_{ao} \\ + & U_{ac} + U_{ac} + U_{aa} + U_{af} \end{cases}$$

$$U_o(\mathbf{r}-\mathbf{r_o}) = \begin{array}{rl} & \left(o_1(x-x_o)^4 + o_2(y-y_o)^4 + o_3(z-z_o)^4 - o_4\right) \\ \times & exp\left(-\left[o_5(x-x_o)^2 + o_6((y-y_o)^2 + (z-z_o)^2)\right]\right) \\ + & o_7 \frac{e^{-o_8(\mathbf{r}-\mathbf{r_o})^2}}{|\mathbf{r}-\mathbf{r_o}|} \end{array}$$

$o_1 = 2.8926$	$o_2 = 0.1017$	$o_3 = 1.9379$	$o_4 = 4.1887$
$o_5 = 1.0552$	$o_6 = 1.2853$	$o_7 = 9.4147$	$o_8 = 23.4135$

$$U_{c\alpha}(\mathbf{r}-\mathbf{r_{c\alpha}}) = \begin{array}{rl} & c_1^\alpha\left[(y-y_{c\alpha}) + c_2^\alpha(z-z_{c\alpha})\right] \\ \times & exp\left(-\left[c_3^\alpha(x-x_{c\alpha})^2 + c_4^\alpha((y-y_{c\alpha})^2 + (z-z_{c\alpha})^2)\right]\right) \\ - & c_5^\alpha \frac{1}{|\mathbf{r}-\mathbf{r}_{c\alpha}|} + c_6^\alpha exp\left[-c_7^\alpha(\mathbf{r}-\mathbf{r}_{c_\alpha})^4\right] \end{array}$$

$c_1^\alpha = 62.6462$	$c_2^\alpha = 0.1426$	$c_3^\alpha = 7.9044$	$c_4^\alpha = 7.9516$
$c_5^\alpha = 0.3147$	$c_6^\alpha = 6.3821$	$c_7^\alpha = 34.2773$	

$$U_{c\beta}(\mathbf{r}-\mathbf{r_{c\beta}}) = \begin{array}{rl} & c_1^\beta\left[(y-y_{c\beta}) + c_2^\beta(z-z_{c\beta})\right] \\ \times & exp\left[-\left(c_3^\beta(x-x_{c\beta})^2 + c_4^\beta((y-y_{c\beta})^2 + (z-z_{c\beta})^2)\right)\right] \\ - & c_5^\beta \frac{1}{|\mathbf{r}-\mathbf{r}_{c\beta}|} + c_6^\beta e^{-c_7^\beta(\mathbf{r}-\mathbf{r}_{c\beta})^4} \end{array}$$

$c_1^\beta = 13.3107$	$c_2^\beta = 1.3455$	$c_3^\beta = 5.3624$	$c_4^\beta = 4.4085$
$c_5^\beta = 0.3033$	$c_6^\beta = 1.4495$	$c_7^\beta = 7.8897$	

$$U_{h\alpha}(\mathbf{r}-\mathbf{r_{h\alpha}}) = -h_1^\alpha \frac{exp\left[-h_2^\alpha(\mathbf{r}-\mathbf{r}_{h\alpha})^2\right]}{|\mathbf{r}-\mathbf{r}_{h\alpha}|} + h_3^\alpha exp\left[-h_4^\alpha(\mathbf{r}-\mathbf{r}_{h\alpha})^2\right]$$

$h_1^\alpha = 0.8357$	$h_2^\alpha = 0.8769$	$h_3^\alpha = 0.2657$	$h_4^\alpha = 0.0852$

$$U_{h\beta}(\mathbf{r}-\mathbf{r_{h\beta}}) = -h_1^\beta \frac{exp\left[-h_2^\beta(\mathbf{r}-\mathbf{r}_{h\beta})^2\right]}{|\mathbf{r}-\mathbf{r}_{h\beta}|} + h_3^\beta exp\left[-h_4^\beta(\mathbf{r}-\mathbf{r}_{h\beta})^2\right]$$

$h_1^\beta = 0.7861$	$h_2^\beta = 0.9584$	$h_3^\beta = 0.1362$	$h_4^\beta = 0.0359$

$$U_{ao}(\mathbf{r}-\mathbf{r_{ao}}) = a_1^o exp\left[-\left(a_2^o(x-x_{ao})^2 + a_3^o(y-y_{ao})^2 + a_4^o(z-z_{ao})^2\right)\right]$$

$a_1^o = 2.7673$	$a_2^o = 1.0552$	$a_3^o = 0.5211$	$a_4^o = 0.7436$

$$U_{ac}(\mathbf{r}-\mathbf{r_{ac}}) = a_1^c exp\left[-\left(a_2^c(x-x_{ac})^2 + a_3^c((y-y_{ac})^2 + (z-z_{ac})^2)\right)\right]$$

$a_1^c = 0.9996$	$a_2^c = 0.6810$	$a_3^c = 0.3058$	

$$U_{aa}(\mathbf{r}-\mathbf{r_{aa}}) = \begin{array}{rl} & a_1^a exp\left[-\left(a_2^a(x-x_{aa})^2 + a_3^a((y-y_{aa})^2 + (z-z_{aa})^2)\right)\right] \\ - & a_4^a exp\left[-\left(a_5^a(x-x_{aa})^2 + a_6^a((y-y_{aa})^2 + (z-z_{aa})^2)\right)\right] \end{array}$$

$a_1^a = 11.7043$	$a_2^a = 0.5978$	$a_3^a = 0.1703$	
$a_4^a = 10.7099$	$a_5^a = 0.5994$	$a_6^a = 0.1597$	

$$U_{af}(\mathbf{r}-\mathbf{r_{af}}) = a_1^f exp\left[-\left(a_2^f(x-x_{af})^2 + a_3^f(y-y_{af})^2 + a_4^f(z-z_{af})^2\right)\right]$$

$a_1^f = 0.4472$	$a_2^f = 0.0443$	$a_3^f = 0.0379$	$a_3^f = 0.2579$

Table 2.3: **Functional Form and Parameters of the Fit to the Exact e$^-$–THF Effective Potential.** The 47-parameter fit has functional contributions centered on 19 different sites. The functional and parameter notations are explained in Ref 59. For the parameters given here, the distances are in Bohr radii and the energies are in Hartrees.

These dimensions were chosen to keep the basis set as small as possible for each system while still capturing the spatial extent of the electronic wave function. We centered the grid in the middle of the simulation cell and shifted all classical particles relative to the grid every 500 fs to avoid leakage of the wave function off the edges of the grid. In this way, the wave function was always located roughly in the center of the simulation cell. The classical particles were shifted an integer number of grid spaces to avoid discontinuities in the quantum energy that would prevent total energy of the simulation from being conserved.[62] We used the velocity Verlet algorithm[82] to propagate the classical degrees of freedom ($\boldsymbol{v}_{\mathrm{Na^+}_i}$, $\boldsymbol{v}_{\mathrm{solv}_i}$, $\boldsymbol{R}_{\mathrm{Na^+}_i}$, and $\boldsymbol{R}_{\mathrm{solv}_i}$) of the Hamiltonian in Eqs. 1 and 2 in the microcanonical (N, V, E) ensemble. We determined the forces from the sum of the classical-classical and classical-quantum interactions described above. We used the implicit restart Lanczos method to iteratively solve the TISE for the ground state wavefunction at every 4 fs time step.[85] The quantum forces on the classical particles were then found using the Hellman-Feynman theorem:

$$\boldsymbol{F}_i^Q = -\langle\Psi|\nabla_{\boldsymbol{R}_i}\hat{H}|\Psi\rangle \tag{2.6}$$

where, $\boldsymbol{F}_i^Q$ is the quantum force on classical particle i at position $\boldsymbol{R}_i$. Because the wave function is expanded in a basis that does not functionally depend on the position of the classical particles, Eq. 5 is exact (in other words, there are no issues with Pulay forces from the basis functions changing with time).[81]

For this paper, we collected data in two ways: 1) by holding the Na–Na bond length at a fixed distance to collect equilibrium statistics on either the ground or first excited state (umbrella sampling) and 2) by placing the Na_2^+ molecule into the first excited state from an equilibrium ground state configuration and then allowing the molecule to propagate adiabatically on its electronic excited state (dynamic dissociation). To conduct umbrella sampling, we set bins at every 0.1 Å and spanned enough distance to adequately capture the shape of both the ground and excited state electronic surfaces. Within each bin, 10 ps of data was collected to ensure ample statistics at each point on the potential energy surface.

For dynamic dissociation, we selected starting configurations from simulations of Na_2^+ in the ground state. We picked uncorrelated configurations where the Na_2^+ molecule was at its ground state equilibrium bond length. For Na_2^+ in Ar, this meant a starting Na–Na bond length of ∼3.7

Å. Because ground state Na_2^+ is stabilized in two primary coordination states in THF, we selected starting configurations for each. For the $Na(THF)_4{-}Na(THF)_5^+$ species, the equilibrium bond length is ∼4.8 Å and for the $Na(THF)_5{-}Na(THF)_5^+$ species the equilibrium bond length is ∼5.6 Å. Fifteen dissociation trajectories were run for Na_2^+ in Ar and twenty for dissociation from each of the two $Na_2(THF)_n^+$ coordination states in THF.

In the next few sections, we will outline the details of various analysis methods used to produce the results described in the paper, including how the umbrella sampling data was used to calculate the equilibrium potentials of mean force (PMFs) and the dissociation data was used to calculate the nonequilibrium, dynamic PMFs.

2.5.2 Analysis Details

Construction of Equilibrium Potentials of Mean Force

As mentioned above, we utilized umbrella sampling to collect equilibrium statistics from the condensed phase Na_2^+ molecule at a wide range of Na–Na bond lengths. Umbrella sampling is a technique used to explore potential energy surface of a system, especially ones in which large energetic barriers prevent adequate sampling of higher energy configurations during normal equilibrium dynamics. Therefore, to force the system to remain in a specific configuration in order to gather statistics, even if that configuration is energetically unfavorable, we define a collective variable and then use a potential well at a target value. Because we want to apply our biasing potential to the Na–Na bond coordinate, the umbrella potential took the form:

$$U(\boldsymbol{r}) = \frac{1}{2}k(\boldsymbol{r} - \zeta)^2 \tag{2.7}$$

where, $U(\boldsymbol{r})$ is the umbrella potential applied to the Na–Na bond coordinate, k is the force constant, $\boldsymbol{r}$ is the Na–Na bond length, and ζ is the target bond length. Because we know the form of the biasing potential, the statistics of the unbiased system can be recovered from the biased statistics.

We then performed multiple simulations, differing only in the target bond length, such that the statistics of neighboring umbrella sampled bins overlapped. These series of umbrella sampled simulations were then stitched together via the multistate Bennet acceptance ratio (MBAR) method[83] to produce the equilibrium PMFs displayed in main text Fig. 1.

Construction of Dynamic Potentials of Mean Force

To compare the equilibrium PMFs to our nonequilibrium, dissociation trajectories, we needed a way to construct a dynamic PMF. To do this, we first calculated $U(t)$ by taking advantage of the relation:

$$U(t) = -\int_{t_0}^{t} F(t)v(t)dt, \tag{2.8}$$

where $F(t)$ is the total force (from the solute and solvent) on the Na nuclei along the bond axis, $v(t)$ is the bond velocity, and t_0 is the time at which photoexcitation takes place. Thus knowing the potential in terms of time, $U(t)$, as well as the bond distance during dissociation, $r(t)$, we can parametrically combine the two to produce the effective potential surface followed during the dynamics, $U(r)$. The integration is calculated in reverse time so that U following dissociation is set to zero.

Because the Na_2^+ molecule dissociates at different time scales in different solvents, the value of t in Eq. 2.8 was chosen such that they were long enough to have sampled all the appropriate photodissociation dynamics but short enough to avoid diffusive recrossings that occur at longer distances. For simulations in liquid Ar, this time was ∼300 fs, while in THF it was much longer at ∼1000 fs.

As mentioned previously, we ran 15 nonequilibrium, dissociation trajectories for Na_2^+ in Ar and 20 from each of the two coordination states in THF. Uncorrelated starting configurations were chosen from equilibrated ground state dynamics. These starting configurations were selected to be at the equilibrium Na–Na bond length of the Na_2^+ electronic ground state. In Ar, this meant selecting 15 initial configurations with a 3.7 Å Na–Na bond length. In THF, this meant selecting 20 initial configurations in the $Na(THF)_4{-}Na(THF)_5^+$ state with a 4.8 Å Na–Na bond length and 20 in the $Na(THF)_5{-}Na(THF)_5^+$ state with a 5.6 Å Na–Na bond length. The individual dynamic PMFs for the $Na(THF)_4{-}Na(THF)_5^+$ and $Na(THF)_5{-}Na(THF)_5^+$ species are plotted below. The data shown in main text Fig. 2b for the overall dynamic PMF in THF was produced by combining the individual PMFs according to the Gaussian weighted ratio of the two coordination states from our previous ground state studies of Na_2^+ in THF,[60] which means that the $Na(THF)_4{-}Na(THF)_5^+$ trajectories counted for about 30% and the $Na(THF)_5{-}Na(THF)_5^+$ for 70%.

Construction of Ar Heat Maps

To compare the Ar cage during dissociation to that at equilibrium, we needed to create an ensemble average of the Ar positions relative to the Na^+ cores. To do so, we created a Fibonnaci sphere of radius 3.3 Å, which is the average Na^0–Ar distance, around each Na^+ core. The advantage of using a Fibonnaci sphere is that it creates any number of evenly spaced points on a sphere. For each point, we then calculate the distance between it and each Ar atom. If an Ar atom is within 1.7 Å, which is the Lennard-Jones radius of Ar, of that point, then it is assigned a value of 1. If not, then it is assigned a value of 0. We then average the spheres over 100+ configurations to get an ensemble picture of the Ar cage at equilibrium.

To generate an ensemble picture of the Ar cage during dissociation, we duplicated each trajectory six times with 60 degree rotations between each duplicate to enhance our statistics. The rotations allow us to force cylindrical symmetry about the Na–Na bond axis. The configurations were also rotated before creating the spheres so that the initial Na–Ar collision occurs on the same Na each time.

2.5.3 Additional Data

In the main text, we described how equilibrium PMFs fail to capture the photodissociation of Na_2^+ in Ar due to a single nonequilibrium event−the solute's collision with the surrounding cage of Ar atoms. Furthermore, we showed that the collision is dynamical because it is dependant on the mass of the solvent. With sufficiently light Ar atoms, the solvent fluctuations occur on a similar time scale to the Na_2^+ photodissociation dynamics; thus, the equilibrium behavior can be recovered. On the other hand, with heavier solvent, the collision of the solute with the solvent cage actually knocks the photofragments back toward each other, leading to a temporary shortening of the Na–Na bond length before the fragments are able to eventually escape the solvent cage. This manifests as a loop in the dynamical PMF, shown in main text Fig. 3.

Here, in Supplementary Figure 1, we plot the actual dissociation trajectories for these three scenarios: Ar of normal mass (green), Ar 20 times lighter than normal (purple), and Ar 5 times heavier than normal (orange). The average of each group of trajectory is also included with green triangles for normal mass Ar, purple squares for the lighter Ar, and orange circles for the heavier

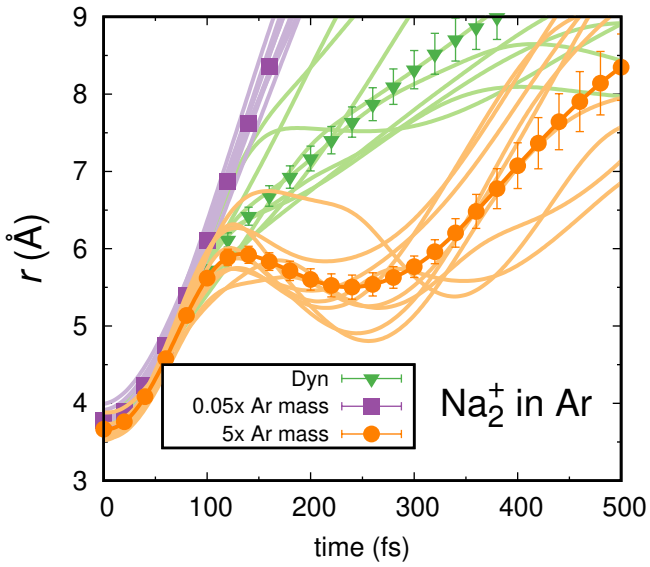

Figure 2.6: Trajectories of the photodissociation of Na_2^+ in Ar of various mass show that the magnitude of solvent caging is dependent on the time scale of the solvent fluctuations. The trajectories where Ar is at its normal mass are plotted in green while those with five times heavier Ar are plotted in orange and those with twenty times lighter Ar are plotted in purple. The average of each type of dissociation trajectory is also included with green triangles form normal mass Ar, orange circles for 20x mass Ar, and purple squares for 0.2x mass Ar.

Ar. The influence of the solute's nonequilibrium collision with the solvent cage are evident in the average curves. For normal mass Ar, a change in slope is observed at the same Na–Na bond distance that the photofragments first encounter the solvent cage. This change in slope is not present for dynamic dissociation with lighter Ar atoms. Instead, the photofragments simply blow through the solvent cage. Finally, with heavier Ar atoms, the photofragments are actually knocked back, such that the Na–Na bond length temporarily decreases, before escaping the solvent cage to continue dissociation.

These and other interesting solvent-induced effects are visible in snapshots from the Na_2^+ trajectories in Ar, as shown in Supplementary Fig. 2, which includes snapshots from the equilibrium pathway (a) and from dynamic dissociation (b). If the solvent is assumed to be at equilibrium with the dissociating molecule, the molecule is able to smoothly pull apart from an initial Na–Na bond distance of 3.5 Å all the way out to 9.5 Å, where the electron localizes onto one of the sodiums. During nonequilibrium dissociation, however, the photofragments must work their way dynamically through the solvent cage. This is most evident when comparing the two snapshots at 5.5 Å. In dynamic dissociation, this is the point where the solute encounters the cage of surrounding Ar

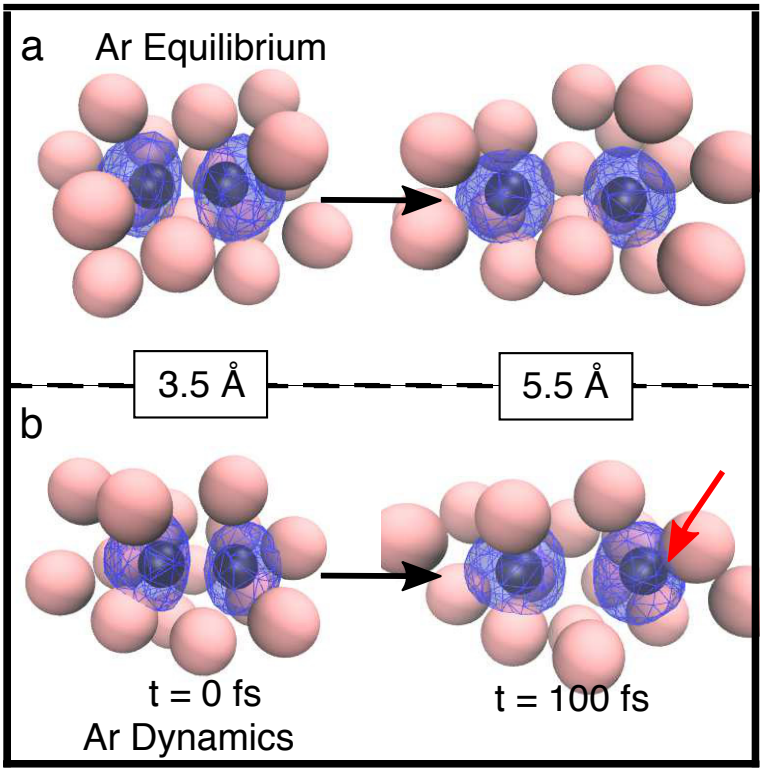

Figure 2.7: Representative snapshots of excited-state Na_2^+ in Ar at equilibrium (panel (a)) and during the nonequilibrium photodissociation dynamics (panel (b)). The Na^+ cores are plotted black spheres at the size of the Na^+ ionic radius, the Ar atoms as pink spheres, and the THF molecules as turquoise sticks with red oxygen atoms. The electron is drawn as a blue wire mesh containing 75% of the density.

atoms. This collision squishes the bonding electron density and knocks the photofragments temporarily back. A direct collision between the right-hand sodium and an Ar atom is even evident. In the equilibrium pathway, however, we see a completely different scenario. Whereas there are no Ar atoms in-between the two photofragments at this point during dynamic dissociation, in the equilibrium pathway, several Ar atoms are working to insert themselves between the sodiums. This actually shoves electron density outward, facilitating dissociation. Finally, in the 9.5 Å snapshot of dynamic dissociation, we can see that the fragments have escaped the solvent cage and now have a buffer of Ar atoms between them. However, the electron has not yet fully localized, instead remaining partially on each sodium.

Now we move on to a brief discussion of the dynamic Na_2^+ PMFs in liquid THF. Main text Fig. 2b plots the dynamic PMF for the nonequilibrium photodissociation of Na_2^+ in THF. However, we know from previous studies[60] that the Na_2^+ molecule exists in THF not as a single species but

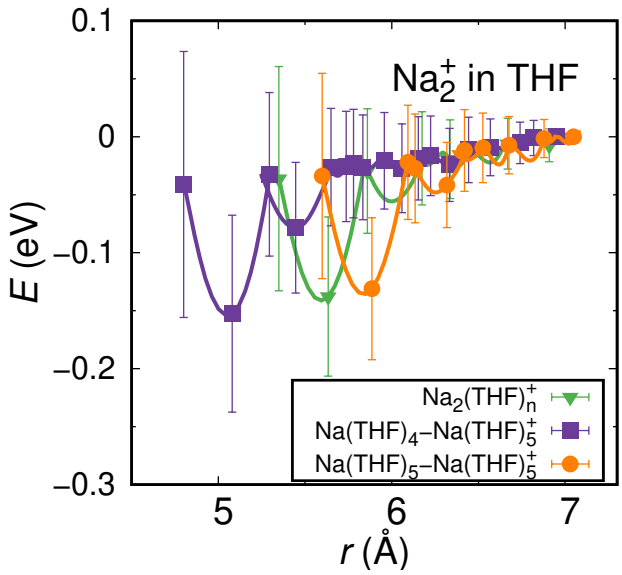

Figure 2.8: Dynamic potentials of mean force for Na2+ in THF. The PMFs are plotted for $Na(THF)_4{-}Na(THF)_5^+$ (purple squares), $Na(THF)_5{-}Na(THF)_5^+$ (orange circles), and $Na_2(THF)_n^+$ (green triangles).

as an equilibrium mixture of $Na(THF)_4{-}Na(THF)_5^+$ and $Na(THF)_5{-}Na(THF)_5^+$, each of which behaves as its own discrete molecule. Therefore, to construct the overall dynamic PMF, we conducted twenty dissociation trajectories from each of these stable coordination states. From those trajectories, we prepared dynamic PMFs as outline above and in the main text. These dynamic PMFs for the $Na(THF)_4{-}Na(THF)_5^+$ (purple squares) and $Na(THF)_5{-}Na(THF)_5^+$ (orange circles) states are plotted here in Supplemental Fig. 3 along with the overall Na_2^+ dynamic PMF in THF (green triangles). The overall dynamic PMF was prepared by combining the dynamic PMFs of the individual coordination states using their Gaussian weighted averages.

As can be seen in Supplementary Fig. 3, all three curves have the same main features: an initial 'dip' in energy followed by a gradual increase in energy at longer distances. The initial dip arises for three primary reasons. First, as we explored in the main text, in liquid THF, when the Na2+ is placed in the first excited state, the bonding electron density initially orients in a π-like state. This is a weakly bound electronic structure which drives the Na–Na bond to lengthen. Second, the bonding electron density then rotates into a σ^*-like position as the molecule dissociates. Finally, the $Na_2(THF)_n^+$ species is capable of forming new Na–THF oxygen-site dative bonds during dissociation. All of these factors combine to initially drive the molecule longer bond

lengths. However, after expending the energy needed to perform these processes, the molecule has no more energy to escape the solvent cage. Thus, there is not a kinetically favorable pathway to Na_2^+ to fully dissociate during dynamic photodissociation in THF. Other wiggles are present in the dynamic PMfs on the gradually rising energetic tail. These come from small shifts in the position of the electronic density as the molecule pulls apart as well as the vibrations of the Na–THF oxygen-site dative bonds.

Chapter 3

Bond Breaking Reactions Encounter Distinct Solvent Environments Causing Breakdown of Linear Response

3.1 Introduction

Solvents can affect chemical dynamics in a variety of ways that are important for understanding solution-phase chemistry. For example, solvents can allow reactants to encounter each other by diffusion and can stabilize or destabilize reactant transition states.[90, 91] Solvent motions also drive electron and proton transfer reactions,[9, 76, 92] and the local solvation environment can break the symmetry of symmetric molecules as well as induce dipole moments.[66, 93–95] Perhaps even more surprisingly, when there are modest local specific interactions between solvents and solutes, the solvent can become part of the chemical identity of a solution-phase reacting species.[60, 61]

The way that solvents affect chemical reactivity can change dynamically during the course of a reaction, adding an additional layer of complexity. Under the linear response (LR) approximation, the solvent dynamics at the start of a reaction should match those associated with the initial solute state (the ground state in a photochemical reaction). At longer times, when a reaction is near completion, however, one expects that the solvent dynamics will match those associated with the equilibrium final state (the excited state in a photochemical reaction).[41, 96, 97] For a number of chemical reactions, and particularly for solution-phase photodissociation, nonequilibrium effects that are not predicted by LR, such as solvent caging, control the reaction dynamics at intermediate times.[5, 8, 10, 11]

The LR approximation assumes that the solvent fluctuations during nonequilibrium dynamics are the same as those present at equilibrium.[34, 90, 98] There have been numerous studies exploring the success or failure of LR in predicting nonequilibrium reaction dynamics and investigating the conditions where LR can be expected to apply.[21, 22, 24, 35, 36, 38, 40, 41, 43–46, 76, 99]. LR is expected to hold when the solvent fluctuations coupled to the reaction coordinate obey Gaussian statistics and to fail when the fluctuations of just a few molecules deviate from Gaussian behavior. [25, 35, 48] LR also can fail when the solvent response occurs on a timescale similar to changes in a solute's physical or electronic structure.[11, 36, 40] Some notable examples of LR breakdown include the rotational coherence of a rigid rotor,[45] solutes that undergo a dipole reversal upon excitation,[25, 41, 42] solutes that undergo significant changes in size and shape,[43, 46, 47] and certain electron transfer reactions.[38, 44, 46] There is also theoretical work arguing that LR can be nonstationary if the equilibrium solvent fluctuations change along a reaction coordinate.[42]

Yet for all the previous studies on solvent dynamics, virtually none have explored how solvent effects change during chemical reactions that explore a wide range of solvent environments. This is the question that serves as the focus of this paper: how does the solvent respond when the solute undergoes a large change in configuration? This is exactly the case for the numerous chemical reactions involving the making and breaking of chemical bonds, including solution-phase photodissociation. As bonds lengthen or are formed, how does the solvent respond, and is the response predictable via LR? To answer these questions, we use quantum molecular dynamics simulations to examine how solvent dynamics change through the course of chemical bond breaking, investigate the dramatically different solvent environments an expanding chemical bond can experience, and

explore the reasons why the LR approximation fails.

The particular system we focus on is the photodissociation of the Na_2^+ molecule in liquid Ar. We chose Ar as our solvent for several reasons. First, Ar has no local specific solute-solvent interactions that could alter the solute chemical identity.[61] Second, as an atomic liquid, Ar provides a particularly simple environment for examining solvent coupling to solute degrees of freedom, as it is apolar and its response can consist only of translational motions. We also chose this system because in previous work, we performed simulations of how liquid Ar alters the electronic and vibrational structure of quantum-mechanically-treated Na_2^+ and we examined how nonequilibrium solvent caging alters the photodissociation dynamics of Na_2^+ relative to that in the gas phase, providing a reference point for the present study.[11, 60]

In this work, we show that following photoexcitation of Na_2^+, the solvent dynamics of liquid Ar change discretely at distinct values of the Na_2^+ bond length. In other words, despite the fact that Ar atoms can only translate, the way that Ar translational motions affect the solute's energy gap dramatically changes as the the solute moves along its reaction coordinate. We further show that the presence of distinct solvation environments is a quantum mechanical effect that cannot be captured using classical molecular dynamics. We also find that the solvent dynamics at the earliest times after photoexcitation do not follow either the ground- or excited-state equilibrium dynamics, constituting a failure of both standard and nonstationary LR. Instead, we see that the initial solvent dynamics are driven by just a few solvent atoms whose motions relative to the dissociating Na_2^+ modulate the solute electronic structure in ways that cannot occur at equilibrium.

The computational methods employed in this work are detailed in the Supporting Information (SI). Briefly, we treat the Na_2^+ molecule as two classical Na^+ cores that are held together by a single quantum mechanically-treated valence bonding electron. We utilize previously-developed pseudopotentials[56] to describe the Na^+–e^- and Ar–e^- interactions.[57, 62, 66] We solve the Schrodinger equation for the electron in a basis of 32^3 grid points. This methodology reproduces gas-phase quantum chemistry calculations of the Na_2^+ molecule quite well.[60, 62] Here, we calculate the behavior of Na_2^+ in liquid Ar, with 1600 solvent atoms, in the canonical (N, V, T) ensemble at 120 K at a density of 1.26 g/mL, well in the liquid region of the phase diagram. In addition to simulations at equilibrium with fixed solute bond lengths on either the ground or electronic excited state, we also ran a nonequilibrium ensemble of 100 trajectories in which uncorrelated equilibrium

ground state configurations were suddenly switched to the excited state to mimic photodissociation. A representative 'movie' of a nonequilibrium photodissociation trajectory is given in the SI.

3.2 Results and Discussion

The standard approach to examining nonequilibrium solvent dynamics is through the calculation of solvation correlation functions. Linear response theories, which are based on the Onsager regression hypothesis, assume that the solvent fluctuations can be treated in the limit where changes in solute structure during chemical reactions are small perturbations from the either the equilibrium ground or excited state.[35, 96, 97] In this limit, the nonequilibrium solvent fluctuations, which are described by a normalized nonequilibrium solvent response function,

$$S(t) = \frac{\langle \Delta E(t) \rangle_{\mathrm{ne}} - \langle \Delta E(\infty) \rangle_{\mathrm{ne}}}{\langle \Delta E(0) \rangle_{\mathrm{ne}} - \langle \Delta E(\infty) \rangle_{\mathrm{ne}}}, \tag{3.1}$$

are well approximated by an equilibrium solvation time correlation function, that is,

$$S(t) \approx C_{\mathrm{g/e}(t)} = \frac{\langle \delta\Delta E(0) \delta\Delta E(t) \rangle_{\mathrm{g/e}}}{\langle (\delta\Delta E(0))^2 \rangle_{\mathrm{g/e}}}, \tag{3.2}$$

where $\langle \ldots \rangle_{\mathrm{ne}}$ indicates a nonequilibrium average, $\langle \ldots \rangle_{\mathrm{g/e}}$ indicates an equilibrium ensemble average on the solute ground (g) or excited (e) state, and $\delta\Delta E(t) = \Delta E(t) - \langle \Delta E \rangle$ is the fluctuation of the solute energy gap, ΔE, away from its average value at equilibrium. The connections between $S(t)$ and $C(t)$ have been described in detail elsewhere.[22, 24, 35, 36, 42]

For our Na_2^+ solute, the energy gap between the electronic ground and excited states can be altered not only by solvent fluctuations but also from changes in the solute bond length, r. Therefore, to isolate the effects of solvent relaxation on the solute electronic structure, we subtract the gas-phase solute energy gap at each bond distance such that

$$\Delta E_{\mathrm{solv}}(r(t)) = E_{\mathrm{e}}(r(t)) - E_{\mathrm{g}}(r(t)) - \Delta E_{\mathrm{gas}}(r). \tag{3.3}$$

We use this definition of the solvent contribution to the solute electronic energy gap for all of the discussion below.

For Na_2^+ in liquid Ar, Figure 3.1 shows equilibrium solvent time correlation functions, $C(t)$, as a function of the Na^+–Na^+ solute bond length, which is held fixed for this series of simulations, from the Frank-Condon region (3.8 Å) out to the dissociation limit (9.0 Å). Figure 3.1a shows the bond-distance-dependent equilibrium response when Na_2^+ is on its electronic ground state, $C_g(t)$, while Fig. 3.1b shows that when the solute is held on its lowest electronic excited state, $C_e(t)$. For comparison, the black curve in Fig. 3.1c shows the nonequilibrium solvent response, $S(t)$, following excitation of Na_2^+ from its ground to its dissociative electronic excited state. The figure makes clear that neither the ground- nor the excited-state equilibrium fluctuations at any solute bond distance are able to accurately predict the nonequilibrium dynamics. Instead, the nonequilibrium solvent relaxation, particularly at early times when the response is expected to consist of the inertial translational motions of the Ar solvent atoms, is faster than the regression of the equilibrium fluctuations on either electronic state.

Of course, one would expect LR to break down in situations where the timescale of solvent rearrangement is comparable to or slower than the timescale of the reaction,[36, 40] something that we have previously observed in this system.[11] Moreover, LR also tends to fail when the dynamics are driven by the motion of just a few molecules so that the fluctuations are not Gaussian,[25, 36, 45] as is the case when solutes undergo changes in size or shape.[43, 46, 47] For our Na_2^+ in liquid Ar system, the nonequilibrium dissociation dynamics are strongly affected by solvent caging, which is an event that involves only a few solvent molecules,[5, 10, 11] so it might not appear surprising that standard LR approaches fail. What is surprising, however, is that the solvent motions that cause LR to fail precede caging and that the nature of the solvent fluctuations changes discretely as the solute bond length expands, both at and away from equilibrium, as we discuss further below.

Looking at the solvent response as a function of Na^+–Na^+ bond distance, Fig. 3.1a demonstrates that the equilibrium ground-state energy gap solvent fluctuations are quantitatively similar, no matter what the bond length of the Na_2^+ solute. In contrast, Fig. 3.1b shows that the equilibrium excited-state energy gap solvent fluctuations change significantly as the solute bond is stretched, with the solvent relaxation becoming faster at longer bond distances. This opens the possibility that LR might hold in the Na_2^+/Ar system, but in a nonstationary fashion. The idea of nonstationary LR was proposed by Geissler and Chandler, who studied the solvent dynamics following a solute dipole reversal in liquid water and argued that solvent fluctuations could be Gaussian but not

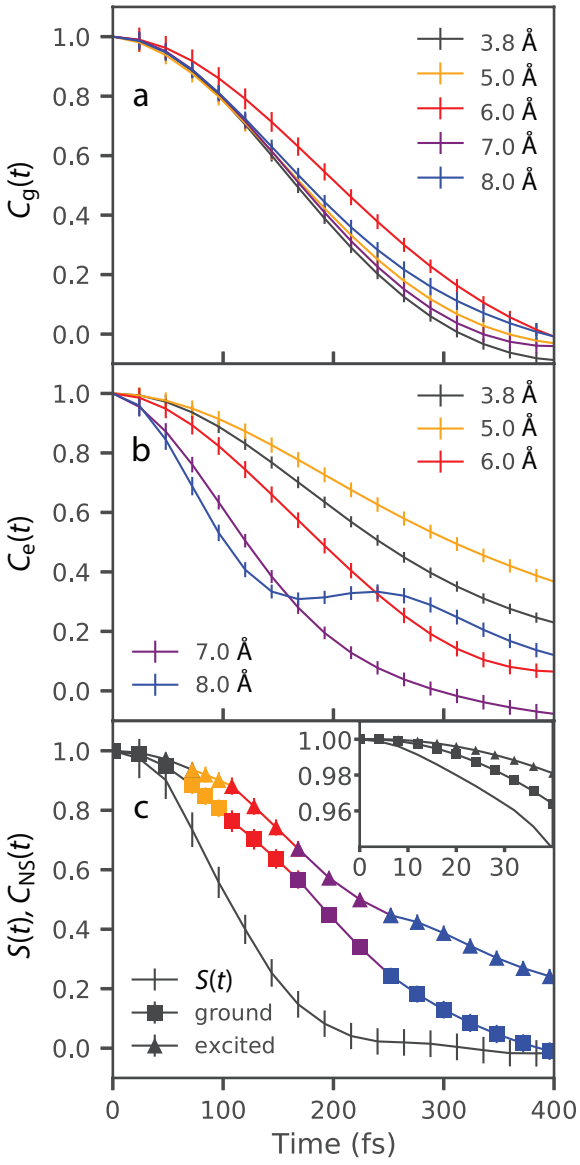

Figure 3.1: Equilibrium solvation time correlation functions (Eq. 3.2) and the nonequilibrium solvent response function (Eq. 3.1) following photoexcitation of Na_2^+ in liquid Ar; all the correlation functions use just the solvation component of the energy gap, Eq. 3.3. The ground-state equilibrium correlation functions shown in panel (a) are evaluated at a series of distances along the Na_2^+ bond length reaction coordinate starting from 3.8 Å, the Franck-Condon region, out to 9.0 Å, the dissociation limit of the molecule. The excited-state equilibrium correlation functions evaluated along the bond distance reaction coordinate are shown in panel (b). Panel (c) shows the nonequilibrium solvent response function as the solid black curve as well as two nonstationary equilibrium correlation function predictions, $C_{NS}(t)$, one using ground-state fluctuations (squares) and the other using excited-state fluctuations (triangles); the colors show the equilibrium correlation functions that are used to construct the nonstationary prediction (see text for details). Clearly, none of the equilibrium solvent response functions, including the nonstationary ones, are able to correctly predict the nonequilibrium behavior, even at early times (inset).

stationary: in other words, the LR-predicted equilibrium solvent dynamics can change at different places along the reaction coordinate. This means that nonequilibrium relaxation might be thought of as proceeding through a series of different equilibrium relaxation dynamics in a nonstationary LR limit.[42]

The colored curves in Fig. 3.1c show two attempts to describe the nonequilibrum relaxation dynamics using a nonstationary LR prediction. The idea is that since the equilibrium solvent response depends on the bond length of the sodium dimer cation (Figs. 1a and b), the nonequilibrium response might follow different LR predictions at different times. Thus, we constructed nonstationary equilibrium correlation functions, $C_{\mathrm{NS}}(t)$, as piecewise additions of the time behavior according to the average nonequilibrium bond distance, $\langle r(t)\rangle_{\mathrm{ne}}$; details are given in the SI. For example, on average, the dimer dissociates to a bond length of 5.0 Å after 72 fs, so the nonstationary correlation function switches from a stationary equilibrium correlation function associated with 3.6 Å to that associated with 5.0 Å after 72 fs. The nonstationary LR prediction using ground-state fluctuations is shown with square markers and that using excited-state fluctuations is shown with triangular markers; the different colors show the equilibrium correlation 'pieces' that contribute to the nonstationary total, using the same color scheme as in panels a and b. What we see is that neither nonstationary correlation function prediction matches the nonequilibrium relaxation, even at the earliest times prior to caging (Fig. 3.1c inset) when the solvent response should be largely inertial. Thus, LR breaks down for describing the solvent motions associated with chemical bond breaking, even when nonstationarity is taken into account.

To understand the role that different solvent motions play at and away from equilibrium for the Na_2^+/Ar system, we analyzed the solvent fluctuations that affect the quantum mechanical energy gap of the solute. Figure 3.2 plots the natural logarithm of the distribution of solvent-induced changes in solute energy gap, creating an effective solvation free energy surface similar to those used in the Marcus theory of electron transfer.[38, 100–102] Panel a shows that the way the solvent affects the solute's electronic structure is quite different when the solute is at equilibrium on the electronic ground state (squares), electronic excited state (triangles) and during the nonequilibrium dissociation dynamics (vertical lines). None of the three free energy surfaces are parabolic, indicating that the solvent fluctuations that underlie these surfaces are not Gaussian (see the SI for details), which is one of the hallmarks of LR breakdown.[25, 35, 36, 45, 48].

All three of the solvation free energy surfaces in Fig. 3.2a, however, fit well to the sum of just a few parabolas that arise at different Na_2^+ bond lengths. For example, Fig. 3.2b shows that the ground-state solvation free energy surface is well described as the sum of three parabolic surfaces, one for solute bond distances between 3.6 and 5.0 Å (yellow squares), one for distances between 5.0 and 7.0 Å (red squares), and one for nearly-dissociated Na_2^+ with bond distances greater than 7.0 Å (blue squares). In a similar fashion, Fig. 3.2c shows that the excited-state solvation free energy surface is composed of four parabolas, separated by bond lengths at 5.8 Å, 6.9 Å, and 7.6 Å, while Fig. 3.2d indicates that the nonequilibrium dynamics following photoexcitation are well-described by three parabolas separated by bond lengths at 6.0 Å and 7.0 Å.

The fact that these solvation free energy surfaces fit to parabolas with different curvatures at distinct Na_2^+ bond lengths suggests that the solute encounters unique solvent environments as it dissociates. In other words, the solvent motions that modulate the solute energy gap fluctuate in one particular way when the bond length is small, and suddenly fluctuate in a different way as the bond extends. The way the fluctuations change with bond length is different for the equilibrium ground-state, equilibrium excited-state, and during the nonequilibrium dynamics. This is remarkable because the liquid Ar solvent in this system can undergo only translational motions, meaning that the same solvent motions affect the solute's quantum energy gap differently as the bond length changes. Thus, rather than experiencing a continuous change of solvent environments, the dissociating solute encounters a small handful of discrete, distinct environments. As described further below, the presence of these distinct environments explains the solute bond length-dependent correlation functions seen in Fig. 3.1, and provides a rationale for the way LR breaks down in this system.

Given that the Ar interaction with Na_2^+ is isotropic and that Ar can only translate, why are there discrete solvation signatures both at and away from equilibrium? We begin answering this question by examining dissociation along the ground-state equilibrium pathway. Near the equilibrium bonding distance, the Na_2^+ electronic ground-state wavefunction is roughly a σ molecular orbital with a prolate spheroidal shape (see, e.g., Fig. 3.1b of Ref. 61 as well as the SI). On the other hand, the excited-state wavefunction, roughly a σ^* anti-bonding molecular orbital, has a node between the two Na^+ cores. As the Na_2^+ molecule's bond lengthens, there comes a point near 5 Å when the Na_2^+ bond length is large enough that an Ar atom can fit between the two Na^+ cores, as

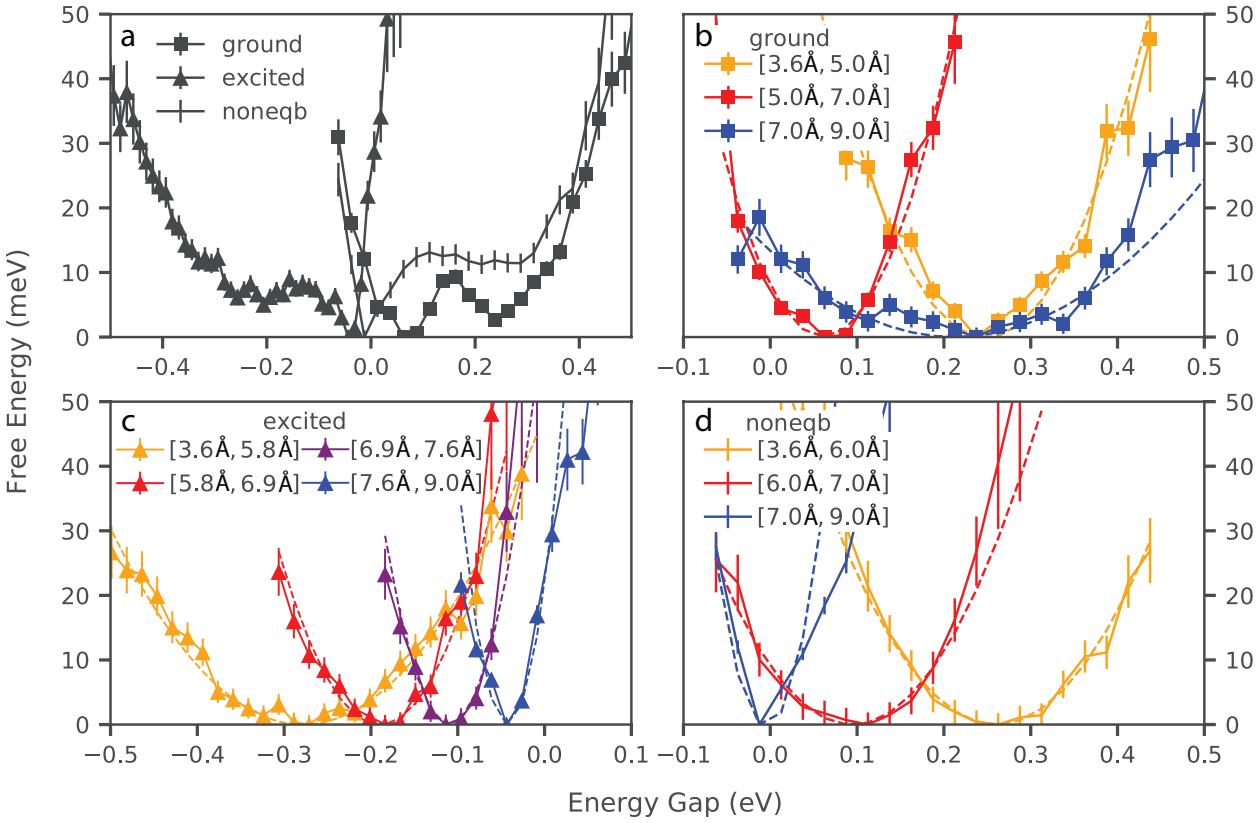

Figure 3.2: Solvation free energy surfaces, computed as the natural logarithm of the solvation energy gap (Eq. 3.3) distributions, for the dissociation of Na_2^+ in liquid Ar. Panel (a) shows the results along the ground-state equilibrium surface (squares), excited-state equilibrium surface (triangles), and the nonequilibrium surface (vertical lines). These distributions can be well described by either three or four parabolas associated with the solvent fluctuations at different Na_2^+ bond lengths; the way the ground-state free energy surface is composed of solvent fluctuations associated with different solute bond lengths is shown in panel (b), the excited-state surface in panel (c), and the nonequilibrium behavior in panel (d). Clearly, the same translational motions of liquid Ar affect the Na_2^+ solute's energy gap differently as the bond length changes during the photodissociation reaction.

demonstrated further below in Fig. 3.3a. The presence of this solvent atom in the intramolecular region modulates the solute energy gap differently from other surrounding Ar atoms because of the node in the excited-state wavefunction. Finally, at even longer bond lengths, starting around 7 Å, the solvent breaks the local molecular symmetry, causing the bonding electron to localize onto one of the two sodium cations: once dissociated, the electronic structure becomes that of a neutral Na atom plus sodium cation rather than a molecular dimer cation; this localization is evident in the representative nonequilibrium trajectory movie shown in the SI.

To visualize the changes in solvent structure when the Na_2^+ bond length reaches 5 Å, Fig. 3.3a shows the average number of Ar atoms in the intramolecular region. The calculation is performed by integrating over a cylinder centered on the dimer, where the length of the cylinder is equal to the solute bond length and the radius of the cylinder is 3.0 Å, which is the average first-shell Na^+-Ar distance, as shown in Fig. 3.3b. As the Na_2^+ bond length increases beyond 5 Å, the most probable number of Ar atoms in the intramolecular region increases from zero to one. The Ar atom located in the intramolecular region has a stronger interaction with the ground-state wavefunction than other Ar atoms but less overlap with the excited-state wavefunction than other Ar atoms because of the excited-state node, as shown explicitly in the SI. Thus, the second solvation free energy parabola in Fig. 3.2b, for bond lengths between 5.0 and 7.0 Å, results from the introduction of intramolecular Ar atoms that destabilize the ground-state energy while moderately stabilizing the excited-state energy. The fluctuations of these intramolecular Ar atoms more strongly affects the solute's energy gap than the motions of other Ar atoms, resulting in a steeper parabolic free energy surface.

To characterize the solvent structure for the third solvation regime at long Na_2^+ bond distances in Fig. 3.2b, for bond lengths between 7.0 and 9.0 Å, we calculated the radial distribution function of the Ar solvent atoms around each Na^+ core (solid curves in Fig. 3.3b). In this figure, we differentiate the two Na^+ cores by labelling $Na_{(1)}$ as that which is closer to the bonding electron's center of mass and $Na_{(2)}$ as that which is further away. Defined this way, we see that $Na_{(1)}$ (green solid curve) has its first Ar solvation shell at 3.8 Å, with a peak height of ∼2, while $Na_{(2)}$ (red solid curve) shows its first solvation shell peak at 3.0 Å with a peak height of nearly 5. The two different pair distribution functions match well with those of isolated neutral sodium atoms and sodium cations in liquid Ar, respectively (dashed curves). Thus, the distinct solvation regime in Fig. 2b at long

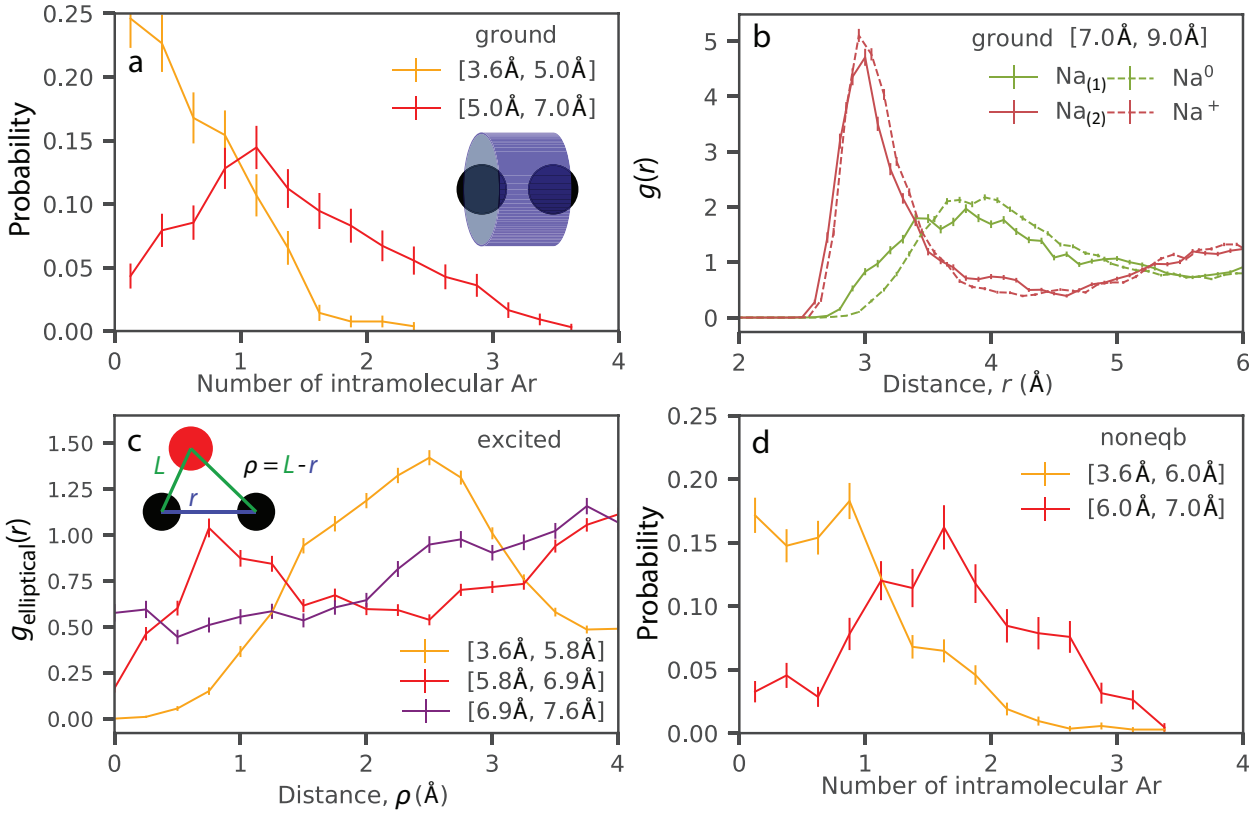

Figure 3.3: Structural changes in the local solvent environment as the Na_2^+ dimer in liquid Ar dissociates along different pathways. Panels (a) and (b) show the changes in structure at equilibrium on the ground state for different Na_2^+ bond lengths, with panel (a) showing the number of Ar atoms in a cylinder around the intramolecular region, as depicted in the inset. Ar atoms within this region more strongly affect the energy gap due to high density of the ground-state wavefunction and sparse density of the excited-state wavefunction. Panel (b) shows Na^+–Ar radial distribution functions, where $Na_{(1)}$ is the Na^+ core closest to the bonding electron's center of mass and $Na_{(2)}$ is the other Na^+ core; at long solute bond lengths, the electron localizes on $Na_{(1)}$ to form Na^0 and Na^+ dissociation products. Panel (c) shows the solvation structure at equilibrium on the excited state using an elliptical distribution function defined according to the schematic in the inset and discussed in the main text. For small excited-state Na_2^+ bond lengths ($\leq$5.8 Å), Ar atoms can only come within $\rho = 2$ Å of the intramolecular region. As the bond length increases, Ar atoms can move to reside between the Na^+ cations on the bond axis, shown by the increase at $\rho = 0$ Å for Na^+–Na^+ distances $\geq$6.9 Å. Panel (d) shows the intramolecular Ar distribution, the same as in panel (a), for different bond length ranges during the nonequilibrium dissociation dynamics.

Na^+–Na^+ distances is due to the bonding electron being localized by the solvent to produce Na^0 and Na^+ dissociation products, a quantum mechanical phenomenon. Ar solvent motions affect the neutral atomic Na^0 energy gap differently than the ionic Na_2^+ cation gap, explaining the different curvature of the solvation free energy parabola for these bond distances in Fig. 3.2b.

To characterize the solvent structures along the excited-state equilibrium pathway, we found it best to use an elliptical distribution function, which is shown in Fig. 3.3c. Like a radial distribution function, the elliptical distribution function we show in Fig. 3.3c counts Ar atoms within a defined region of space around the dimer, but instead of radial distances, it counts according to an elliptical criterion, L, which is the sum of the distances between an Ar atom and each Na^+ core. Plotted on the horizontal axis of Fig. 3.3c is the difference between the elliptical criterion, L, and the Na^+–Na^+ distance, r, to create a common axis, $\rho = L - r$, for ease of comparison. Defined this way, a value of $\rho = 0$ Å would identify Ar atoms positioned directly along the bond axis, while a value of $\rho = 2$ Å would identify first-shell Ar atoms in the Na_2^+ intramolecular region that lie ≈ 2 Å away from the bond axis, as illustrated in the schematic shown in the inset. As Na_2^+ dissociates, the solvent rearranges so that first-shell Ar atoms that were outside the bond axis can now lie along the bond axis, which can be seen in the rise in the elliptical distribution at $\rho = 0$ Å and the fall between $\rho = 1$ Å and $\rho = 3$ Å. Like the change in solvent structure seen at 5.0 Å for the ground-state equilibrium dissociation (Fig. 3.3a), this change in packing leads to a greater interaction of intramolecular Ar atoms with the ground-state wavefunction than the excited-state wavefunction of the solute, and thus a distinct solvent fluctuation signature with a steeper parabola as the dimer dissociates and Ar atoms can reach the bond axis between the Na nuclei.

The change in solvent environment along the excited-state equilibrium pathway at Na_2^+ bond lengths greater than 7.6 Å can be understood by the fact that the ground and excited states of the solute are becoming degenerate. (For reference, the ground- and excited-state energies with the solvent held in equilibrium with the excited-state solute, are shown in Ref. 11.) Because the electronic states are quasi-degenerate at the dissociation limit, the energy gap is necessarily close to 0 eV with small fluctuations, as observed in Fig. 3.2c. It is worth noting that in the dissociation limit, the ground- and excited-state wavefunctions have the electron on different Na^+ cores (the roles of Na^0 and Na^+ are reversed on the electronic ground and excited states), so that at equilibrium the two states are equally solvated. In the SI, we calculate the Ar-electron overlap for each solute

energy state in the 7.6 Å to 9.0 Å bond length range, and show that the overlap of Ar atoms with the excited state is indeed identical to that of the ground state.

Although our finding that there are discrete solvation environments along the equilibrium dissociation pathways was unexpected, the main motivation of this work is to understand the nature of the nonequilibrium solvation dynamics during photodissociation, shown in Fig. 3.2d. Away from equilibrium, the dimer cation encounters three distinct solvent environments, at solute bond lengths less than 6 Å, between 6 Å and 7 Å, and for bond separations greater than 7 Å. The initial nonequilibrium solvation free energy distribution (yellow curve in Fig. 3.2d) is clearly more similar to that of the ground-state distribution (yellow squares in Fig. 3.2b), while the nonequilibrium solvation free energy surface at later times (blue curve in Fig. 3.2d) is more similar to that of the excited state (blue triangles in Fig. 3.2c). This change in behavior from more ground-state-like to more excited-state-like is in line with expectations,[41, 96, 97] but the nonequilibrium solvent fluctuations still do not match any of the equilibrium distributions.

Of course, one feature that affects the nonequilibrium dynamics of dissociating Na_2^+ in liquid Ar that is not present at equilibrium is solvent caging, which we have previously investigated for this system.[11] On average, the dimer cation dissociates to a Na^+–Na^+ distance of 6.0 Å after 100 fs, which is the average time when the Na^+ cores collide with their first-shell Ar solvent atom neighbors. Along with this caging event, we also observe an increase in the number of intramolecular Ar atoms (Fig. 3.3d) at this distance, similar to what we described above for the ground-state equilibrium at 5.0 Å separation; the intramolecular Ar atoms do not appear until larger bond distances in the nonequilibrium dynamics because given the inertia of the solvent atoms, there simply isn't time for Ar to 'notice' the empty space between the separating Na atoms. Once the Na_2^+ bond length reaches 7.0 Å, the solvation dynamics are determined by the near-degeneracy of the ground and excited states, much like what what we described above for the excited-state equilibrium, where the fluctuating energy gap is necessarily centered at zero with minimal spread.

With this understanding of how the nonequilibrium solvent environment changes with solute bond distance, we return to discuss the origins of the breakdown of LR seen at early times seen in Fig. 3.1c. Although solvent caging, the strong collision of the dissociating solute with the first-shell solvent atoms, is a single-solvent-atom effect that is expected to lead to a breakdown of LR,[5, 10, 11] caging does not take place until $\geq$100 fs after photoexcitation. Instead, the more rapid

relaxation of the nonequilibrium energy gap at early times that is the hallmark of LR breakdown can be explained by the motion of the dissociating Na^+ cations creating relative Ar motions that help to rapidly close the energy gap. In other words, the breakdown of LR is entirely a quantum mechanical effect that directly involves the electronic structure of the Na_2^+ solute on its ground and electronic excited states; this breakdown would not have been observed had we described the system on a potential of mean force using classical molecular dynamics.

To understand how relative solute-solvent motions affect the dissociating solute's quantum energy gap, we performed gas-phase calculations of a dissociating Na_2^+ dimer interacting with a single Ar solvent atom; details of how we performed these calculations are included in the SI. The idea is that when Na_2^+ is promoted to its dissociative excited state, the rapidly expanding solute effectively moves Ar atoms toward the solute. Ar atoms that lie along the expanding solute bond axis move toward the Na^+ cores (Fig. 3.4a), while Ar atoms that are displaced from the bond axis move parallel to the bond toward the intramolecular region (Fig. 3.4b). Because Ar atoms undergo relative motion toward the solute, the distances shown in Figs. 4a and 4b are plotted with larger Ar–Na distances to the left, so that time following the photodissociation proceeds from left to right. The distance ranges shown approximately reflect the relative Ar motions over the first 100 fs following photoexcitation, prior and up to the caging event.

Figure 3.4a shows that relative motion of axial Ar atoms moving toward the expanding Na_2^+ solute causes a large change in the quantum energy gap. The excited-state wavefunction has a larger axial extent than the ground state wavefunction, so Pauli repulsion interactions from the approaching solvent atom raise the solute's excited-state energy. In contrast, the same axial motion of solvent atoms toward the solute leads to slight stabilization of the ground-state energy due to van der Waals' forces. Figure 3.4b shows that for Ar atoms that are displaced from the bond axis, the effect of relative solvent motion toward the solute is opposite, stabilizing the excited state and destabilizing the ground state. Because of the node in the excited-state wavefunction, the presence of Ar in the intramolecular region leads to van der Waals' stabilization, while the nodeless ground-state wavefunction experiences strong Pauli repulsion from the overlapping Ar atom in this region. During the nonequilibrium dissociation dynamics, both types of relative solvent motion—along the bond axis and 'above' the bond axis into the intramolecular region—occur. In combination, these motions lead to net destabilization of the ground state and relatively little change in the

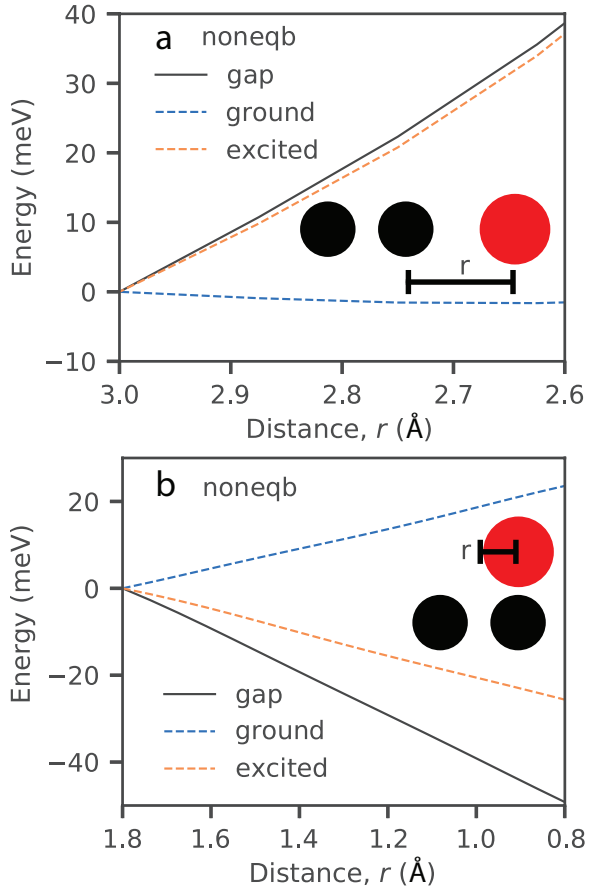

Figure 3.4: Panel (a) shows the effect on the Na_2^+ energy gap (black curve) of a single non-intramolecular Ar atom moving along the sodium dimer cation bond axis towards one of the Na^+ cores: because the excited-state Na_2^+ molecular orbital extends further along the bond axis, Ar motions along the bond axis destabilize the excited-state energy (red dotted curve) more than the ground-state energy (blue dashed curve). Panel (b) shows the effect on the Na_2^+ energy gap (black curve) of a single Ar atom that sits 3.0 Å above the bond axis moving parallel to the bond axis towards the intramolecular region: because of the presence of the node in the excited-state molecular orbital, Ar motion along this axis tends to stabilize the excited-state energy (red dashed curve) and destabilize the ground state (blue dashed curve). The distance axis is defined separately for each panel and each panel includes a cartoon to illustrate the motion being considered. The distance axis is plotted with larger distances to the left so that reading from left to right follows the relative Ar motion with time following photoexcitation: 100 fs after excitation, axial Ar atoms are ∼2.6 Å away from the Na^+ cores, and Ar atoms that are displaced from the bond axis have moved to reside 1.0 Å from the intramolecular region. These differences explain why the solute encounters distinct solvent environments as it dissociates.

excited-state energy (see the SI for more details). This quantum mechanical effect is what causes the nonequilibrium energy gap to close more quickly than at equilibrium on either the ground or the excited state, leading to the breakdown of LR seen in Fig. 3.1c.

3.3 Conclusions

In summary, through MQC MD simulations of the photodissociation of Na_2^+ in liquid Ar, we have explored how solvent fluctuations change during the course of a bond breaking reaction. In the process, we tested both standard approaches and a nonstationary approach to LR and find that neither LR approach captures the nonequilibrium solvent fluctuations at early times (Fig. 3.1). We find that the energy gap distributions can be fit to a few Gaussians that are well separated by solute bond length and have unique curvatures, indicating discrete changes in solvent environment (Fig. 3.2). If the dimer dissociates along the ground-state equilibrium surface, it will encounter three distinct solvent environments, with one new environment induced by an increase in the number of intramolecular Ar atoms (Fig. 3.3a) and a second induced by localization of the electron to form $Na^+ + Na^0$ (Fig. 3.3b). If the dimer dissociates along the excited-state equilibrium surface, then it will encounter four distinct solvent environments, with the one at the longest bond distances caused by the near solvation energy degeneracy of the two Na^+ cores on the ground and electronic excited states. The intermediate excited-state environments result from changes in solvation structure that are best captured using an elliptical distribution function (Fig. 3.3c). When nonequilibrium dissociation is initiated by photoexcitation, the solute encounters three distinct solvent environments including the Franck-Condon region. One change in environment results from solvent caging and the driven collision of the photofragments with the first solvent shell, and the second new environment at long bond lengths arises from degeneracy as with the equilibrium excited state. Although the initial nonequilibrium solvent environment in the Franck-Condon region is structurally identical to that of the equilibrium ground state, the solvation dynamics away from equilibrium are significantly different because of dissociation-driven relative Ar motions that quickly close the energy gap (Figs. 4a and 4b). The effect of these nonequilibrium relative motions on the solute energy gap is entirely quantum mechanical in nature, and these motions also explain the early-time (pre-caging) breakdown of LR for this system.

Overall, even for an isotropically interacting, apolar solvent with primarily repulsive interactions that can only undergo translational motions, such as liquid Ar, solvent environments and the way their fluctuations couple to the electron structure of solutes can change suddenly and dramatically during the course of bond breaking or bond formation. We close by noting that the changes in solvent response result from changes in solute geometry that change the quantum mechanical interactions between the solute and solvent. Because of the fact that solutes encounter distinct solvent environments as their bond length changes, the solvent response depends on the reaction pathway taken, highlighting the complexity of solution-phase solvation dynamics. We expect that these observations should be generally applicable for solution-phase chemistry, including bond breaking, bond formation, and electron transfer reactions where there are significant changes in geometry of the donor and acceptor.[103–105]

3.4 Supplementary Information

3.4.1 Simulation Details

Mixed Quantum/Classical Model

Our mixed quantum/classical (MQC) molecular dynamics (MD) simulations consisted of two classical Na^+ cations, one fully quantum mechanical electron, and 1600 Ar atoms in a simulation cell with a side length of 43.8 Å. The simulation size was chosen to reproduce the appropriate solvent densities at the simulation temperatures (1.26 g/mL at 120 ± 2 K for Ar simulations, which is well within the liquid region of simulated Ar's phase diagram[87]). Periodic boundary conditions were implemented with minimum image convention[82] and all interactions were tapered smoothly to zero at 16 Å over a 2 Å range with a center of mass-based switching function according to Steinhauser.[84] All simulations were performed in the microcanonical ensemble.

Because all interactions were taken to be pair-wise additive, the full Hamiltonian of the system is $\hat{H} = H^{\mathrm{cl}} + \hat{H}^{\mathrm{qm}}$. In atomic units, the classical portion of the Hamiltonian is given by

$$H^{\mathrm{cl}} = \frac{1}{2} m_{\mathrm{Na}^+} \sum_{i=1}^{2} v_{\mathrm{Na}^+{}_i}^2 + \frac{1}{2} m_{\mathrm{solv}} \sum_{i=1}^{n_{\mathrm{solv}}} v_{\mathrm{solv}_i}^2 + U^{\mathrm{Na}^+-\mathrm{Na}^+}(|\boldsymbol{R}_{\mathrm{Na}^+{}_1} - \boldsymbol{R}_{\mathrm{Na}^+{}_2}|)$$
$$+ \sum_{i=1}^{n_{\mathrm{solv}}} \sum_{j>i}^{n_{\mathrm{solv}}} U^{\mathrm{solv}-\mathrm{solv}}(|\boldsymbol{R}_{\mathrm{solv}_i} - \boldsymbol{R}_{\mathrm{solv}_j}|) + \sum_{i=1}^{2} \sum_{j=1}^{n_{\mathrm{solv}}} U^{\mathrm{Na}^+-\mathrm{solv}}(|\boldsymbol{R}_{\mathrm{Na}^+{}_i} - \boldsymbol{R}_{\mathrm{solv}_j}|) \quad (3.4)$$

where v_{solv_i} is the velocity of the i^{th} solvent (Ar) at position $\boldsymbol{R}_{\mathrm{solv}_i}$ with mass m_{solv}. $U^{\chi-\gamma}$ is a classical potential between atom types χ and γ ($\chi, \gamma = \mathrm{Na}^+$ or Ar).

The quantum Hamiltonian is given by

$$\hat{H}^{\mathrm{qm}} = \sum_{i=1}^{2} \frac{\hat{\boldsymbol{p}}_i^2}{2} + \sum_{i=1}^{2} \sum_{j=1}^{2} V^{\mathrm{Na}^+}(|\boldsymbol{R}_{\mathrm{Na}^+{}_j} - \hat{\boldsymbol{r}}_i|) + \sum_{i=1}^{2} \sum_{j=1}^{n_{\mathrm{solv}}} V^{\mathrm{solv}}(|\boldsymbol{R}_{\mathrm{solv}_j} - \hat{\boldsymbol{r}}_i|) \quad (3.5)$$

where $\hat{\boldsymbol{p}}_i$ and $\hat{\boldsymbol{r}}_i$ are the momentum and position operators for electron i, respectively, and V^{χ} is the pseudopotential representing the interaction between the quantum electron and atom type χ =Na^+ or Ar.

For the MQC studies, the classical interaction between the two Na^+ cations was modeled through a point-charge Coulomb potential, $U^{\mathrm{Na}^+-\mathrm{Na}^+}(R) = e^2/R$, where e is the fundamental charge, since the short-range repulsion between the cores is negligible around the internuclear separation of Na_2^+.

The Na^+-Ar interaction was taken from a fit to the *ab initio* calculations of Ahmadi, Almlöf, and Røeggen[88]:

$$U^{\mathrm{Na}^+-\mathrm{Ar}}(R) = \frac{a_1 \exp(-a_2 R)}{R} - \frac{2}{1 + a_1 \exp(a_3/R)} \left(\frac{C_6}{R^6} + \frac{C_8}{R^8} \right) \quad (3.6)$$

where $a_1 = 242.32$ Hartree, $a_2 = 1.67$ bohr^{-1}, $a_3 = 5.6$ bohr, $C_6 = 255$ bohr^5, and $C_8 = 4410$ bohr^7. Following Gervais et al,[57] we have subtracted the charge-dipole term, which goes as $-0.5\alpha_{\mathrm{Ar}}/R^4$, where α_{Ar} is the dipole polarizability of Ar.

All other classical interactions were modeled with Lennard-Jones potentials:[82]

$$u_{ij}(r_{ij}) = \frac{1}{4\pi\epsilon_0} \frac{q_i q_j}{r_{ij}} + 4\epsilon_{ij} \left[\left(\frac{\sigma_{ij}}{r_{ij}} \right)^{12} - \left(\frac{\sigma_{ij}}{r_{ij}} \right)^{6} \right] \quad (3.7)$$

where r_{ij} is the distance between the i^{th} and j^{th} Ar/Na^+ site, q_i is the charge on the i^{th} site, ϵ_{ij} is the potential well depth, and σ_{ij} is the finite distance at which the inter-particle potential is zero. The Lennard-Jones parameters used in this study are listed in Supplementary Table 1. The standard Lorentz-Berthelot combining rules were used to calculate the solute-solvent site interactions.[82]

	σ (Å)	ϵ (kJ/mol)	q (e)
Argon	3.405	0.996	0.0
Na^+	1.67	22.07	+1.0

Table 3.1: **Lennard-Jones and Coulomb potential parameters for the solute-solvent systems studied in this work.**

Phillips Kleinman (PK) pseudopotentials were used to account for the interactions between the classical particles and the quantum mechanical electrons.[55] These PK potentials were modified with polarization potentials to correct for the frozen core approximation implicit in PK formalism.[58, 59, 89] For the electron-Ar interaction, $V^{e^- - \text{Ar}}$, we used a modified version of the pseudopotential developed by Gervais *et al*,[57] described in detail in our previous work.[66] For $V^{e^- - \text{Na}^+}$ we used rigorously-derived psedopotentials previously developed by our group, the details of which can be found in Ref. 58. The final pseudopotential fits are presented here in Supplementary Table 2.

Simulation Setup

The eigenstates of the quantum mechanical valence bonding electron were expanded on a three dimensional grid. For simulations in Ar, we used a basis of 32 × 32 × 32 grid points distributed over a 43.8^3 Å^3 box. These dimensions were chosen to keep the basis set as small as possible for each system while still capturing the spatial extent of the electronic wave function. We centered the grid in the middle of the simulation cell and shifted all classical particles relative to the grid every 500 fs to avoid leakage of the wave function off the edges of the grid. In this way, the wave function was always located roughly in the center of the simulation cell. The classical particles were shifted by an integer number of grid spacings to avoid discontinuities in the quantum energy that would prevent total energy of the simulation from being conserved.[62] We used the velocity Verlet algorithm[82] to propagate the classical degrees of freedom ($\boldsymbol{v}_{\text{Na}^+}$, $\boldsymbol{v}_{\text{Ar}}$, $\boldsymbol{R}_{\text{Na}^+}$, and $\boldsymbol{R}_{\text{Ar}}$) of the Hamiltonian in Eqs. 1 and 2 in the microcanonical (N, V, E) ensemble. We determined the forces from the derivatives

sum of the classical-classical and classical-quantum energy interactions, described above. We used the implicit restart Lanczos method to iteratively solve the time-independent Schrodinger equation for the ground-state wavefunction at every 4-fs time step.[85] The quantum forces on the classical particles were found using the Hellman-Feynman theorem:

$$\boldsymbol{F}_i^Q = -\langle\Psi|\nabla_{\boldsymbol{R}_i}\hat{H}|\Psi\rangle, \tag{3.8}$$

where, $\boldsymbol{F}_i^Q$ is the quantum force on classical particle i at position $\boldsymbol{R}_i$. Because the wave function is expanded in a basis that does not functionally depend on the position of the classical particles, Eq. 5 is exact (in other words, there are no issues with Pulay forces from basis functions that change with time).[81]

For this paper, we collected data in two ways: 1) by holding the Na–Na bond length at a fixed distance to collect equilibrium statistics on either the ground or first excited state (a form of umbrella sampling) and 2) by placing the Na_2^+ molecule onto its first excited state from an equilibrium ground-state configuration and then allowing the molecule to propagate adiabatically on its electronic excited state (dynamic dissociation). To conduct umbrella sampling, we set bins at every 0.1 Å and spanned enough distance to adequately capture the shape of both the ground- and excited-state electronic surfaces. Within each bin, 10 ps of equilibrated data was collected to ensure ample statistics at each point on the potential energy surface.

For dynamic dissociation, we selected starting configurations from simulations of Na_2^+ in the ground state. We picked uncorrelated configurations where the Na_2^+ molecule was at its ground state equilibrium bond length. For Na_2^+ in Ar, this meant a starting Na–Na bond length of ∼3.8 Å. One hundred dissociation trajectories were run for Na_2^+ in Ar. In the next sections, we will outline the details of the analysis methods used to produce the results described in the paper.

3.4.2 Analysis Details

Calculation of Error Bars

The error bars of the equilibrium response functions are calculated using the standard error,

$$\text{error} = \frac{s}{\sqrt{n}} \tag{3.9}$$

where s is the sample standard deviation and n is the number of samples.

The error bars of the nonequilibrium response functions are calculated by propagation of error

$$\text{error} = S(t)\left[\left(\frac{\sigma_f}{f}\right)^2 + \left(\frac{\sigma_g}{g}\right)^2\right]^{1/2} \tag{3.10}$$

where σ is the standard error, $f = \langle \Delta E(t) \rangle_{\text{ne}} - \langle \Delta E(\infty) \rangle_{\text{ne}}$, and $g = \langle \Delta E(0) \rangle_{\text{ne}} - \langle \Delta E(\infty) \rangle_{\text{ne}}$.

The error bars shown in the solvation free energy surfaces (Fig. 2 of the main text) are calculated by propagation of error

$$\text{error} = -0.424 k_B T \left(\frac{N}{n}\right)\left[\left(\frac{\sigma_n}{n}\right)^2 + \left(\frac{\sigma_N}{N}\right)^2\right]^{1/2} \tag{3.11}$$

where σ is the standard error and n is the number of observations for a particular bin and N is the number of the observations for the largest bin.

All error bars shown in Fig. 3 of the main text are calculated using the standard error.

Construction of Nonstationary Response

The equilibrium solvent response functions, $C_{\text{g/e}}(t)$, shown in the main text do not individually account for changes in Na–Na length. We formulated a nonstationary equilibrium solvent response by stitching together $C_{NS}(t)$ by Na–Na length using $\langle r(t) \rangle_{\text{ne}}$ as reference. Each piece was also vertically adjusted to ensure continuity.

$$C_{\text{NS,g/e}}(t) = \begin{cases} C_{\text{g/e,3.8}}\ (t) & t \leq t_{\text{ne}} \ni \langle r(t) \rangle_{\text{ne}} = 5.0 \\ C_{\text{g/e,5.0}}\ (t) & t \leq t_{\text{ne}} \ni \langle r(t) \rangle_{\text{ne}} = 6.0 \\ C_{\text{g/e,6.0}}\ (t) & t \leq t_{\text{ne}} \ni \langle r(t) \rangle_{\text{ne}} = 7.0 \\ C_{\text{g/e,7.0}}\ (t) & t \leq t_{\text{ne}} \ni \langle r(t) \rangle_{\text{ne}} = 8.0 \\ C_{\text{g/e,8.0}}\ (t) & t > t_{\text{ne}} \ni \langle r(t) \rangle_{\text{ne}} = 8.0 \end{cases} \tag{3.12}$$

Parabolicity and Gaussian Statistics

The free energy surface is calculated by taking the negative natural logarithm of the energy gap distribution. If the surface is parabolic, then exponentiating will result in a Gaussian distribution

of the gap fluctuations.

Interaction of Gas-Phase Rigid Na_2^+ with a Single Ar Atom

The gas-phase calculations in Fig. 4 of the main text were performed by setting the Na^+–Na^+ distance to 3.8 Å, the average Na-Na equilibrium bond length, and the initial Na^+–Ar distance to 3.0 Å, also the average value at equilibrium in solution. While the Na^+ positions were held fixed, the Ar motion was controlled to create the slices shown in Fig. 4a and 4b of the main text, with Fig. 4a showing the influence of an axial Ar moving toward a Na^+ core and Fig. 4b showing the influence of Ar moving into the intramolecular region from above the bond axis. The Ar motions were controlled to show only the expected distances traveled within the first 100 fs of dissociation (i.e., prior to caging).

3.4.3 Additional Data

Snapshots of the Bonding Electron Before and After Excitation

In the main text, we connected the change in solvent environments with the electronic structure of the bonding electron. In Supplementary Figure 3.5, both the ground- and excited-state wavefunctions for a representative equilibrium ground-state configuration are shown. The ground-state wavefunction resembles a prolate spheroidal σ molecular orbital, and the excited-state wavefunction resembles a σ^* molecular orbital with a node between the Na^+ cores. As the dimer dissociates, Ar atoms that enter the nodal region will destabilize the ground-state energy but not strongly affect the excited-state energy.

Nonequilibrium Bond Distance Against Time

The main text describes the evolution of the Na^+–Na^+ distance after photoexcitation at a few key time points. To aid the reader in visualizing the time scale of the dynamics, we have included the nonequilibrium average Na^+–Na^+ distance against time with time zero being the moment of photoexcitation. Times <100 fs correspond to the inertial region where the sodium cores dissociate freely and follow similar dynamics as gas phase Na_2^+. Around 100 fs, the sodium cores collide with the first solvent shell, "caging" the solute where we can see the evolution of Na^+–Na^+ distance

i	c_i (a.u.)	α_i (a.u.)
1	-16.3145	0.124293
2	0.0455219	0.0322129
3	16.3213 81	0.124181

Table 3.2: **Parameters used in the construction of the sodium-electron pseudopotential,** $\phi(r) = \sum_{i=1}^{3} c_i e^{-\alpha_i r^2}$**.** Further details of the sodium-electron pseupotential can be found in Ref. 58

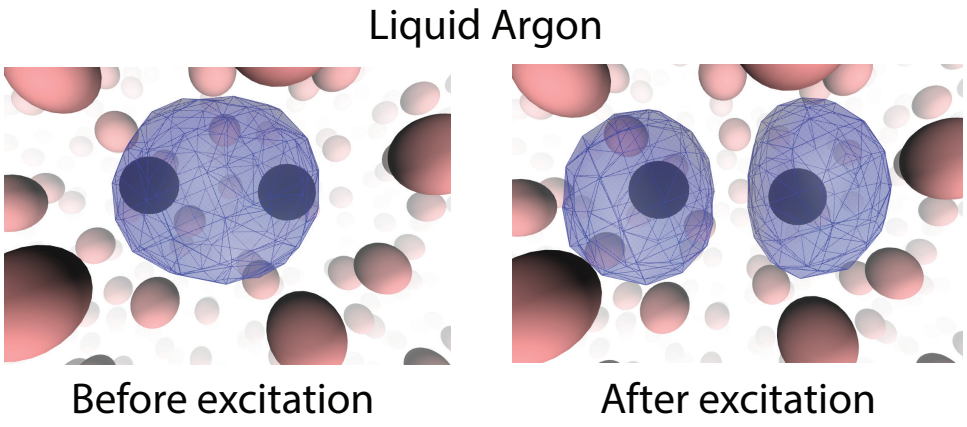

Figure 3.5: Snapshots of Na_2^+ in Ar before and after Franck-Condon excitation of the bonding electron for a ground-state equilibrium configuration. The ground-state bonding electron is roughly a σ molecular orbital with a prolate spheroidal shape prior to excitation. The excited state is roughly a σ^* molecular orbital with a node between the two Na^+ cores.

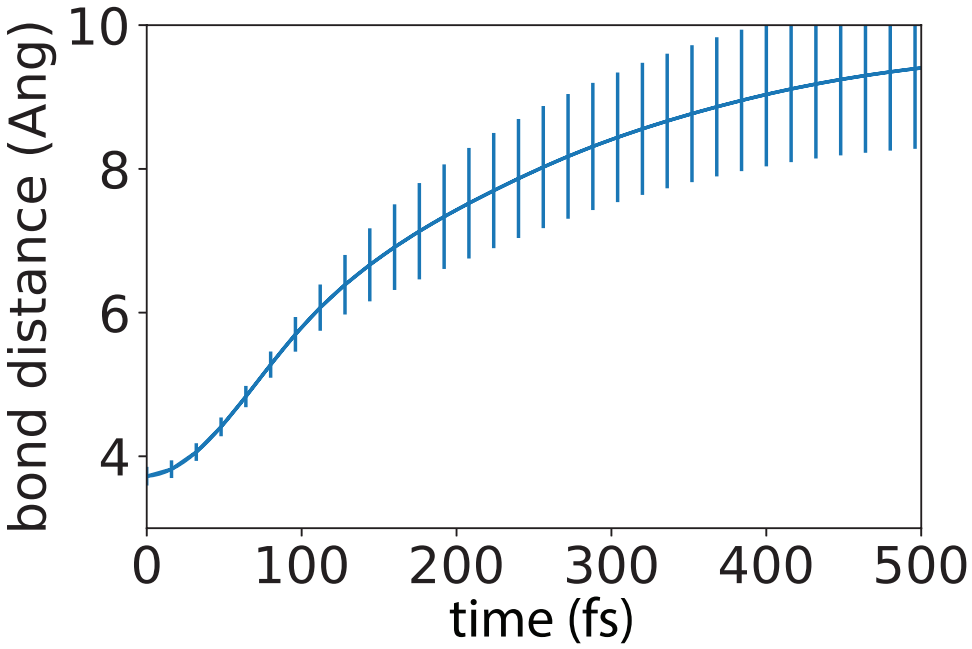

Figure 3.6: Average nonequilibrium Na^+–Na_+ distance against time. After excitation, the sodium cores rapidly dissociate in the inertial region, then ∼100 fs, the sodium cores collide with the first solvent shell. The error bars shown are for the standard deviation.

deflect.

Counting Intramolecular Ar for Excited State Equilibrium

The main text details how solvent environments change along the ground state equilibrium and nonequilibrium pathways by counting the number of intramolecular Ar at each distance. But instead of counting the intramolecular Ar for the excited state equilibrium pathway, we opted instead to show an elliptical distribution function in the main text. For interested readers, the count of intramolecular Ar for the excited state equilibrium pathway is shown in Supplementary Figure 3.7. For all values of Na^+–Na^+ distance, there is at least one intramolecular Ar, unlike the ground state equilibrium and nonequilibrium pathways, because of the solvent is equilibrated to the node of the excited state wavefunction. As the dimer cation dissociates beyond 5.8 Å, the average number of intramolecular Ar increases but it appears as the distribution shifts to larger numbers, but this difference is within the noise. As the dimer dissociates to 6.9 Å, the change in the distribution of intramolecular Ar is more clear. Overall, the elliptical distribution function shows a clearer structural change hence why we opted to use it for the main text.

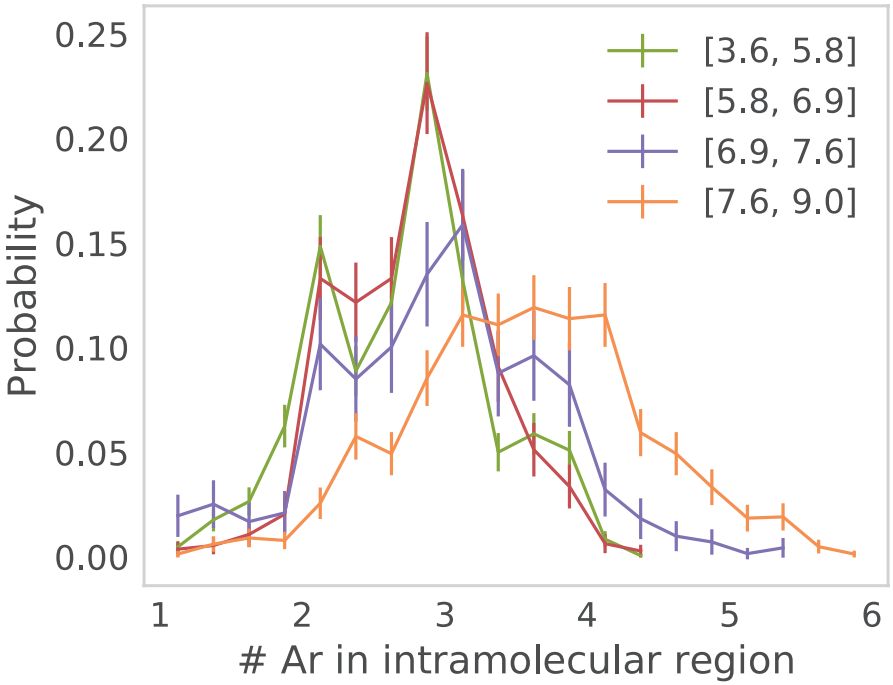

Figure 3.7: Structural change in the local environment of Na_2^+ in liquid Ar along the excited state equilibrium pathway by counting the number of intramolecular Ar. Like the main text, counting is done by integrating over a cylinder of radius 3 Åwhose height is the bond vector.

Ground- and Excited-State Energies at Equilibrium and Nonequilibrium

The main text describes how changes in solvent environment affect the signature of the energy gap fluctuations. In Supplementary Figure 3.8, we show how the ground-state and excited-state energies change with Na_2^+ bond length for each dissociation pathway: ground-state equilibrium, excited-state equilibrium, and nonequilibrium. The ground-state equilibrium pathway shows three distinct regimes separated at 5.0 Å and 7.0 Å, which coincide with the Gaussian fits and structural changes shown in the main text. As the dimer lengthens beyond 5.0 Å, the ground state is destabilized and the excited state is moderately stabilized, which is coincident with Ar atoms entering the intramolecular region as described in the main text. As the dimer lengthens beyond 7.0 Å, the ground- and excited-state energies diverge with the difference approaching the difference in solvation energy between Na^+ and Na^0.

The main text describes the excited-state equilibrium pathway as having four distinct regions separated at 5.8 Å, 6.9 Å, and 7.6 Å. The fluctuations in both the ground- and excited-state energies make it difficult to observe clear transitions, but near 7.6 Å, the energies become nearly degenerate, which can be more clearly seen in the bottom right panel of Supplementary Figure 4, where the energy gap is plotted. Because the energies are quasi-degenerate, the distribution is necessarily centered near 0 eV with minimal spread, as shown in the main text.

The main text describes the nonequilibrium pathway as having three distinct regions separated at 6.0 Å and 7.0 Å. Because of the relative Ar motions described in the main text, the ground state is quickly destabilized while the excited state is largely unaffected at early times. Between 6.0 Å and 7.0 Å, the excited state stabilizes from solvents entering the intramolecular region, like that described for the ground state equilibrium pathway and as depicted in the main text. From 7.0 Å on, the ground state and excited state are degenerate, just as was seen near the dissociation limit along the excited state equilibrium pathway.

Ar-e^- Overlap for Excited-State Equilibrium

The main text points out that the ground state and excited state reside on different Na^+ cores near the dissociation limit. With the two states being degenerate in energy and on different Na^+ cores, the two wavefunctions should also have equivalent solvent environments. To illustrate this,

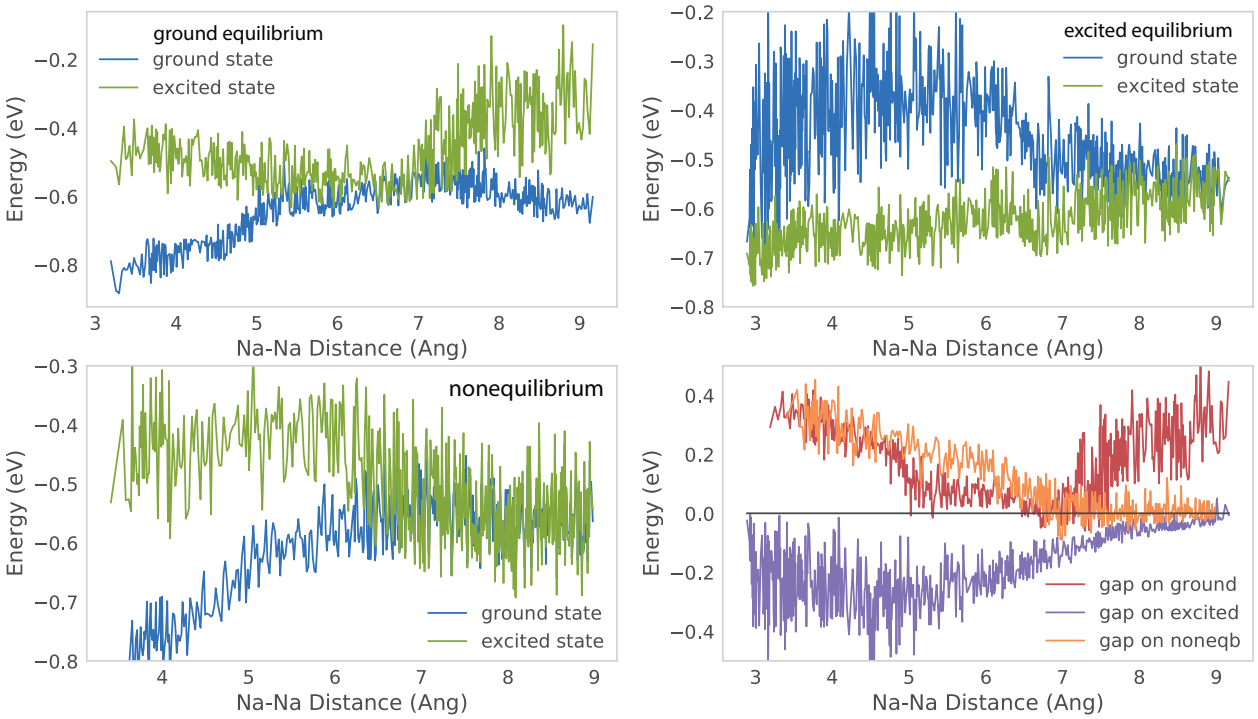

Figure 3.8: Stabilization/destabilization of the ground- and excited-state energies held at equilibrium and also during nonequilibrium dynamics. When the molecule is held on the ground state (top left), the ground-state energy is destabilized by Ar atoms entering the intramolecular region at 5 Å, but the excited-state energy is slightly stabilized. Then at 7 Å, when the electron localizes onto one of the sodium cation cores, the ground- and excited-state energies split, with the difference being the difference in the solvation energies of Na^0 and Na^+. When the molecule is held on the excited state (top right), the ground and excited states become degenerate at 7.6 Å. Other characteristic changes in solvent environment are difficult to observe because of the magnitude of fluctuations. When the molecule dissociates away from equilibrium (bottom left), the ground state is quickly destabilized and the excited state is slightly stabilized from the relative Ar motions detailed in the main text. At 6.0 Å, the excited state stabilizes from intramolecular Ar and from 7.0 Å on, the ground state and excited state become degenerate.

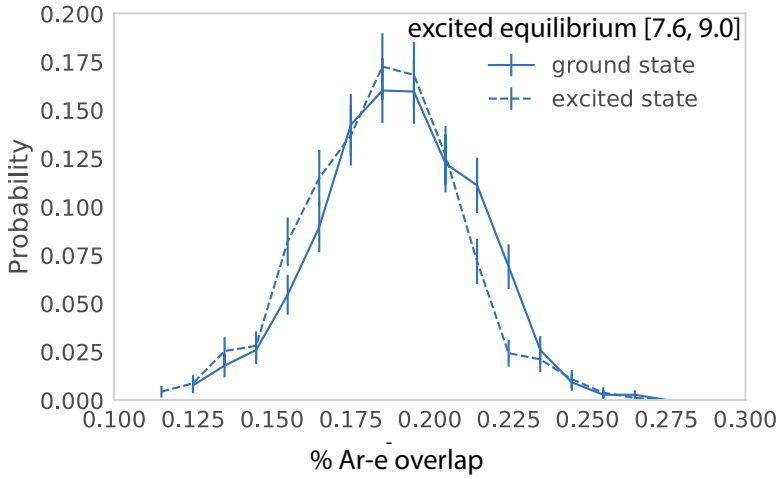

Figure 3.9: Ar-e^- overlap for both the ground- and excited-state wavefunctions when the Na_2^+ molecule is held on the excited state and bond length is between 7.6 Å and 9.0 Å. That identical overlap between the Ar and each wavefunction indicates that both states are equally solvated, coinciding with the energies becoming degenerate.

we calculate the Ar-e^- overlap for each wavefunction, and indeed it is identical for the two states.

Chapter 4

Solvent Control of Chemical Identity Can Change Photodissociation Into Photoisomerization

4.1 Introduction

Most chemical reactions take place in solution, where the solvent is typically viewed as a background medium for reacting solute molecules to encounter one another via diffusion. Of course, for a few special cases, such as solvated electrons[1] and charge-transfer-to-solvent transitions,[**Blandamer**, 3] solvents can help to create electronic states that otherwise would not exist if the solutes were in the gas phase. And in electron transfer and related reactions, solvent reorganization is the primary driving force[106] to move charge from the donor to the acceptor, and thus determines the reaction rate.[107–111]

In addition to the special cases where reactions cannot occur without solvent mediation, the presence of solvent molecules can also strongly alter our gas-phase-like picture of solution-phase

chemistry, i.e. solvent molecules can do much more than act as a reactive medium. For example, first-shell solvent molecules can 'cage' the products of photodissociation reactions, inhibiting separation of the photofragments and promoting recombination.[4–8] Additionally, photoreaction pathways and photofragment relaxation timescales can differ depending on solvent polarity [112–114] or viscosity[115] . Moreover, solvent interactions can alter the potential energy surface on which reactions take place, changing them significantly from what they were for an isolated gas-phase solute[9–18]. Previously, we have shown that Pauli repulsion interactions from surrounding solvent molecules can compress a solute's bonding electrons, raising a solute's bond vibrational frequency.[66] We have also shown that modest locally-specific solute-solvent interactions, with energetics similar to those of a hydrogen bond, can change the chemical identity of a solute.[60, 61] In such cases, the chemical species must be thought of as a solute-solvent complex rather than a gas-phase solute perturbed by solvent interactions.[60, 61]

In this work, we use quantum simulation methods to examine how solvent-induced changes in chemical identity affect the breaking of chemical bonds. In particular, we show that for a diatomic solute that normally undergoes a photodissociation reaction in the gas phase, the chemistry following photoexcitation in solution is entirely different: the solution-phase dynamics involve a two-step process whose first step is best described as a photoisomerization reaction involving solvent rearrangement, followed by a second quasi-dissociative step that can take place only after the solvent isomerization is complete. Because motions of the solvent molecules rather than solute photofragments dominate the early-time dynamics, the solution-phase reaction needs to be described by a two-dimensional potential energy surface involving collective motion of the first-shell solvent molecules rather than the simpler one-dimensional potential energy curves that describe the gas-phase photoreactivity. The results indicate that the solvent can play an intimate role in chemical reactions involving bond breaking or formation, potentially requiring a whole new formalism beyond what is typically done in the gas phase.

The system we choose to study in this work is the Na_2^+ molecule dissolved in liquid tetrahydrofuran (THF), which we simulate using mixed quantum/classical (MQC) molecular dynamics (MD). The Na^+ solute cores and THF solvent molecules are treated classically, while the valence bonding electron is treated quantum mechanically. We simulate photoexcitation of the solute by taking uncorrelated equilibrium configurations of the ground-state system and placing the bonding elec-

tron onto its first excited state at time zero, then propagating dynamics adiabatically to generate a nonequilibrium ensemble of 20 trajectories. We chose this system because it is readily amenable to study via MQC MD: the electronic structure of gas-phase Na_2^+ is fairly easy to describe due to the relative lack of exchange and correlation contributions between the valence bonding electron and the core electrons,[80] and the necessary electron–Na^+ core and electron–THF pseudopotentials[56] have already been developed and thoroughly benchmarked.[59, 62, 64, 81] The methods we employ here are similar to those in our previous work,[11, 60, 61] and they reproduce the gas-phase quantum chemistry of Na_2^+[62, 80] and experimental properties of Na^+:solvated electron tight contact pairs in liquid THF[63, 64] quite well. Further details are given in the Methods section below as well as the Supporting Information (SI).

4.2 Results and Discussion

As a reference point for understanding solvent effects on chemical bond-breaking, we begin our analysis by studying the behavior of the photoexcited Na_2^+ solute in the gas phase. Figure 4.1a shows snapshots of the bonding electron's charge density for the solute in the ground state before excitation (left), in the Franck-Condon region immediately following excitation (center), and when the fragments have separated to a distance of 8 Å (right). The ground and Franck-Condon excited-state charge density clearly resemble bonding σ and antibonding σ^* molecular orbitals, respectively, with the nodal plane of the excited-state wavefunction oriented perpendicular to the bond axis. As the molecule separates, half the bonding electron is associated with each Na^+ core, as there is nothing in the gas phase to break the symmetry to localize the electron and create the eventual Na^0 + Na^+ photoproducts.

In liquid THF, however, the solvent forms dative bonds to the solute,[64] which changes the solute chemical identity.[61] For Na_2^+ in liquid THF, two new chemical species are formed, consisting of $Na(THF)_4$–$Na(THF)_5^+$ and $Na(THF)_5$–$Na(THF)_5^+$ complexes, which we will refer to as (4,5) and (5,5), respectively, for brevity. We will also refer to $Na(THF)_4^+$ and $Na(THF)_5^+$ as the 4-end and 5-end, respectively. We have previously argued that these complexes are separate molecules (with a $\sim$6 kT barrier for interconversion between them) with distinct Na^+–Na^+ bond lengths, vibrational frequencies, and electronic absorption spectra.[60]. Here, we focus on the chemistry

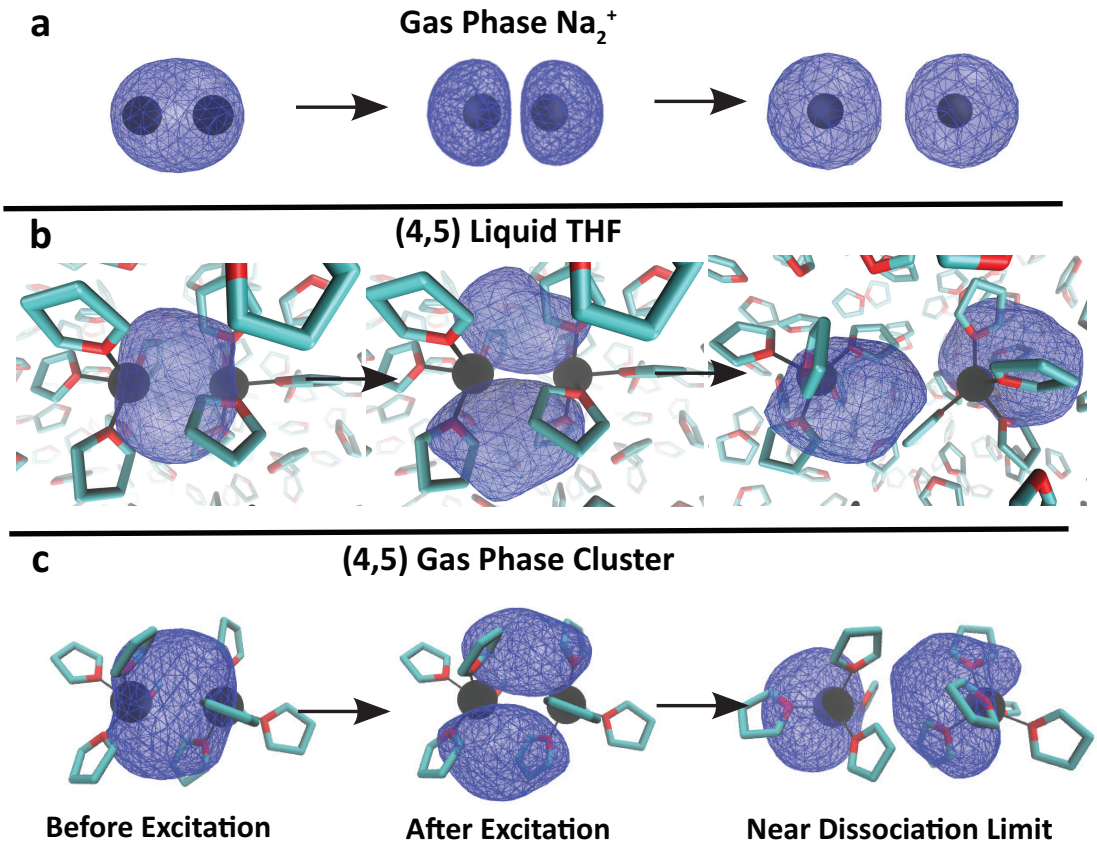

Figure 4.1: Simulation snapshots of the excited-state electron density for Na_2^+ in different environments: (a) the gas phase; (b) in liquid THF; (c) as a gas-phase $Na(THF)_4{-}Na(THF)_5^+$ solvated cluster. In each panel, the left-most figure displays a snapshot of the Na_2^+ species in its ground-state equilibrium, the center figure shows the electron density in the Franck-Condon region immediately after photoexcitation, and the right-most figure shows the excited-state electron density after the photofragments have separated to a distance of ~8 Å. The Na^+ cores are plotted as black spheres and THF solvent molecules are plotted as turquoise sticks with red oxygen atoms. Dative bonds are shown as thin black lines connecting THF oxygen sites and Na^+. The gas-phase Na_2^+ bonding electron density resembles a σ^* MO immediately after photoexcitation. In the presence of datively-bonded THF, however, the Franck-Condon excited-state bonding electron density resembles a π MO, whose node re-orients to a σ^* orientation only at the dissociation limit.

following photoexcitation of the (4,5) species for conciseness, but a similar analysis and conclusions for photoexcitation of the (5,5) complex can be found in the SI.

The change in chemical identity from Na_2^+ to a (4,5) (or (5,5)) solvated complex completely changes the electronic structure of Na_2^+,[60, 61] as can be seen in Fig. 4.1b. Due to Pauli repulsion of the datively-bound THF molecules, the bonding electron has its excited-state node oriented parallel to the Na^+–Na^+ bond axis, similar to the structure of a π bonding molecular orbital (center). As the Na^+–Na^+ distance lengthens, the electron density shifts so that the node now lies perpendicular to the bond axis, picking up σ^* character (right; see also the movie of this process included in the SI).[11] Because of the differences in electron density between Fig. 4.1a and Fig. 4.1b, photoexcitation of Na_2^+ in liquid THF, where dative bonds with the solvent cause changes in the chemical identity of the solute, cannot be thought of as simply a gas-phase Na_2^+ photodissociation reaction slightly perturbed by the solvent.

In Fig. 4.1c, we show what happens following photoexcitation of a (4,5) Na_2^+/THF complex as a gas-phase cluster, removing the effect of the bulk solvent. The excited-state relaxation process in this case is similar to what occurs in the full liquid phase, where the bonding electron initially has π character but transitions to have more σ^* character by the $\sim$8 Å dissociation limit. This verifies that the datively-bound THF molecules are important participants in this photoexcitation reaction, confirming that the proper chemical identity is a complex that includes the datively-bound THFs rather than a solvent-perturbed Na_2^+. A comparison between Figs. 1b and c, however, shows that photoexcitation of (4,5) in solution can be thought of as similar to that of the gas-phase (4,5) complex with minor perturbations, emphasizing that including the datively-bound solvents as part of the solute is necessary to understand this condensed-phase photoreaction.

The snapshots seen in Fig. 4.1 lead to an obvious question: what causes the excited-state bonding electron to change its character from π-like to σ^*-like? The answer lies in the specific datively-bonded solvent molecular geometry and how this geometry evolves following photoexcitation. For the 4-end of the (4,5) complex, the solvents are initially arranged in a seesaw configuration and evolve into a more tetrahedral configuration after photoexcitation and subsequent relaxation. For the 5-end of the (4,5) complex, we see square pyramidal and trigonal bipyramidal configurations before and after photoexcitation, respectively. To track the dynamics of these local solvent geometry changes, we define an order parameter, $h(t)$, based on the interior angles of the 4-end and

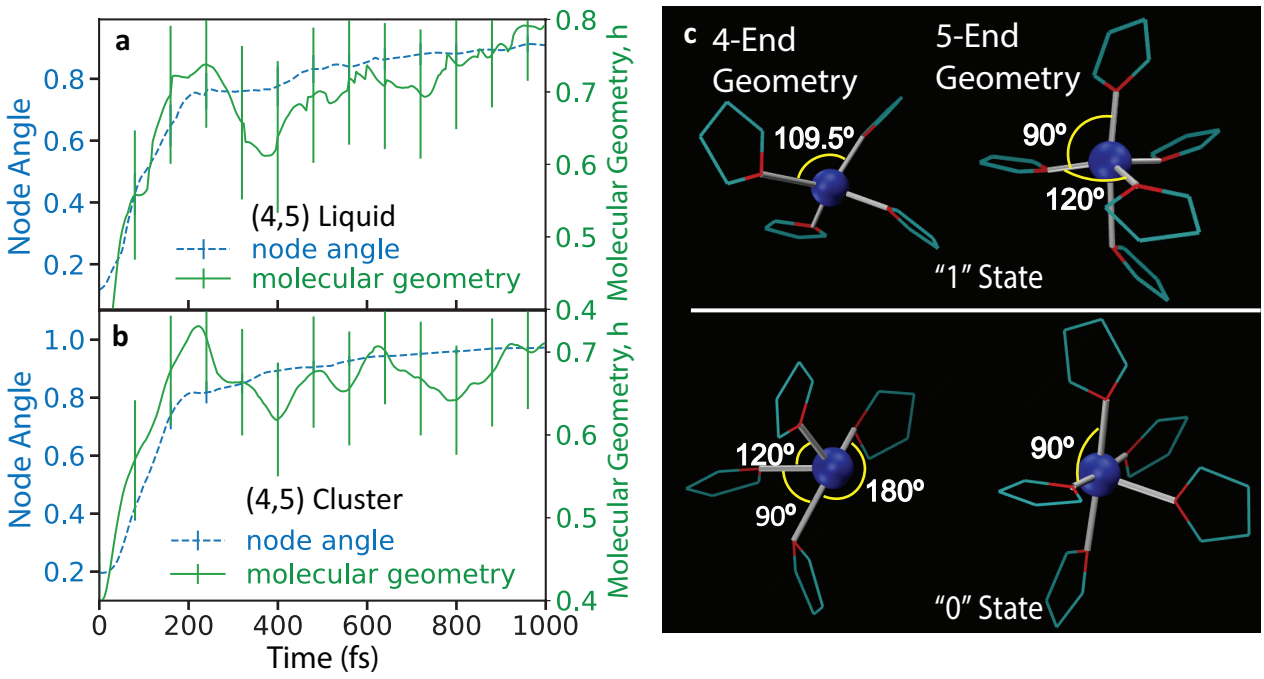

Figure 4.2: Nonequilibrium ensemble average dynamics of the molecular geometry, h (green curves), and node angle (dashed blue curves) of the (4,5) species following photoexcitation. Panel (a) shows the molecular geometry and node angle evolution for the (4,5) complex in liquid THF, while panel (b) shows the same for the (4,5) gas-phase cluster. In both cases, there is a significant change in the molecular geometry over the first ∼200 fs that is correlated with a change in the node angle. Panel (c) illustrates the ideal molecular geometry states of both the 4-end and 5-end of the (4,5) complex with the $h = 0$ equating to a seesaw/square pyramidal state and $h = 1$ equating to a tetrahedral/trigonal bipyramidal state. Error bars are $\pm 2\sigma$.

5-end of the (4,5) complex.[60] The $h(t)$ function is constructed to have a value of 0 when the local geometry is seesaw/square pyramid and a value of 1 when the local geometry is tetrahedral/trigonal bipyramid. Details of how $h(t)$ was constructed are given in the Methods section below.

Figure 4.2 shows the connection between the molecular geometry, $h(t)$, of the (4,5) complex (green curves) and the angle of the node in the excited-state wavefunction relative to the Na^+–Na^+ bond axis (blue curves) for the first ps following excitation. The node angle is calculated by taking the dot product of the ground-to-first-excited-state transition dipole moment with the Na^+–Na^+ bond axis, so that a value of 0 results when the nodal plane is parallel to the bond axis (π-like MO) and a value of 1 means that the nodal plane is perpendicular to the bond axis (σ^*-like MO). The data show that the rotation of the excited-state node from parallel to perpendicular occurs during the same ∼200-fs period following excitation as the coordinating THF's change their geometry from a seesaw/square pyramid configuration to a tetrahedral/trigonal bipyramid configuration. In other

words, after photoexcitation, the motions of the datively-bound solvent molecules are directly tied to the rotation of the node in the bonding electron's wavefunction. Since the distance between the 4-end and 5-end do not change during this solvent rearrangement, as discussed further below, we refer to the dynamics during this ∼200-fs window as a photoisomerization process.

The fact that the initial photoexcitation produces an excited-state wavefunction with more π character than σ^* character suggests that there is little driving force to separate the Na^+ ions in the Franck-Condon region: in other words, the presence of the datively-bonded THF solvents means that photoexcitation is not initially dissociative.[11] Yet, if trajectories are run sufficiently long, i.e. much longer than necessary for the gas-phase reaction, the Na^+ ions in the presence of THF eventually do separate. To understand this later-time separation and include the fact that the datively-bonded solvent molecules are part of the identity of the molecule,[60, 61] we define a dissociation parameter, R based on the distance between the centers of mass of $Na(THF)_4^+$ and $Na(THF)_5^+$ photofragments for the excited (4,5) complex. What we will show next is that h and R represent effectively orthogonal parameters that are capable of describing the excited-state dynamics of (4,5) complexes in either liquid THF or the gas phase.

The left side of Figure 4.3 shows two-dimensional energy surfaces for the photoexcitation of (4,5) in liquid THF (panel a) and for the (4,5) gas-phase complex (panel b), where one axis is the datively-bonded solvent molecular geometry, h, and the other is the distance between photofragment centers of mass, R. The specifics of how these surfaces were generated are included in the Methods section below. Superimposed on the energy surfaces are orange curves showing the time-averaged behavior of the nonequilibrium ensemble. The right side of Fig. 4.3 shows the same nonequilibrium average behavior from a 'top-down' view, where the energy change is shown via the color of the curve. The time along the nonequilibrium average trajectory is labelled at a few select points in both sets of plots.

At the time of photoexcitation, Fig. 4.3 shows that the average equilibrium configuration of the (4,5) complex has a value of $R \sim 6$ Å and $h \sim 0.4$, indicating a geometry that is closer to seesaw/square pyramid. Immediately following photoexcitation, the (4,5) complex in liquid THF (Fig. 4.3a) spends the first ∼200 fs moving solely along the molecular geometry coordinate, with the datively-bonded THFs isomerizing to achieve a more tetrahedral/trigonal bipyramid structure ($h = 0.8$), a process that is driven by an energy drop of ∼200 meV. Only after the isomerization is

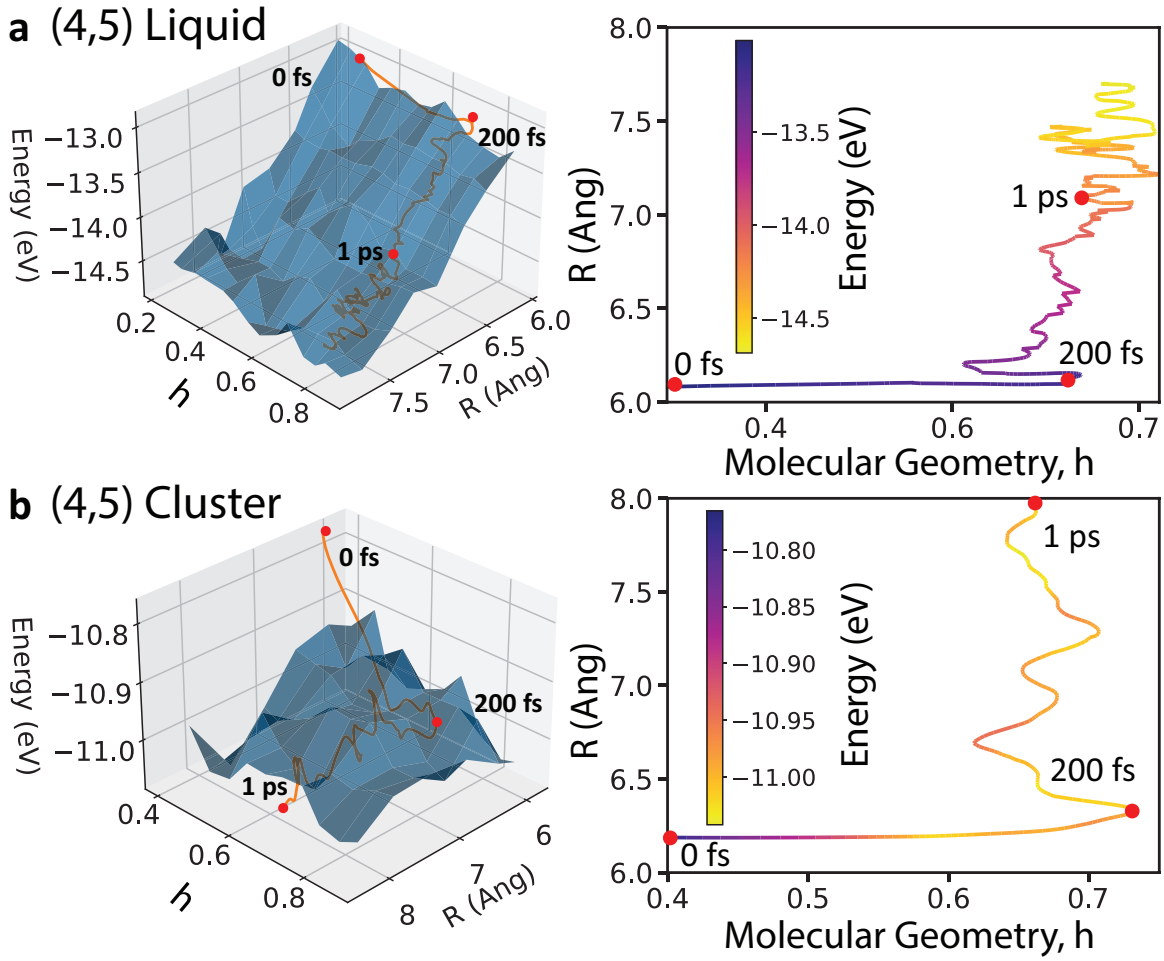

Figure 4.3: Two-dimensional energy surfaces (shown in blue in the left diagrams) with axes comprised of the datively-bonded solvent geometry, h, and the photofragment distance separation, R, for the nonequilibrium dynamics following photoexcitation of (4,5) in (a) liquid THF and (b) as a gas-phase cluster. The right diagrams show the same nonequilibrium average trajectory from a 'top-down' view with the color used to indicate the value of the energy. The time following photoexcitation is shown at a few select points. Clearly, the first ∼200-fs of the motion out of the Franck-Condon region is entirely along h, effectively a photoisomerization reaction that is associated with a ∼200 meV drop in energy. Only after the isomerization is complete can the system begin to move along the R dissociative coordinate. Dissociation of the gas-phase cluster in panel (b) is driven by only a ∼100 meV energy loss, while that of the (4,5) complex in the liquid in panel (a) is accompanied by nearly a full eV energy loss due to a change in chemical identity as the reaction occurs (cf. Fig. 4.4).

complete does the system begin to move along the distance coordinate (accompanied by fluctuations along the geometry coordinate), which leads to a roughly 1 eV additional energy drop. The velocity of motion along the R distance coordinate (compare Fig. 4.4, below) is much slower than for a bare gas-phase Na_2^+ molecule, so we refer to this separation as being only weakly dissociative. For comparison, the photodissociation reaction of bare gas-phase Na_2^+ has the fragments reaching a distance of 8 Å by ∼140 fs.

For photoexcitation of a gas-phase (4,5) complex (Fig. 4.3b), the first ∼200 fs of dynamics after excitation is nearly identical to that seen in solution, with motion solely along the molecular geometry axis and an associated energy drop of ∼200 meV. Once the isomerization is complete, the system then moves slowly along the R coordinate, but the energy drop along this coordinate is now only ∼100 meV instead of nearly a full eV. The net conclusion of Fig. 4.3 is that once we account for the fact that the solvent is part of the chemical identity of the molecule, the energy surface (of the initially diatomic solute) to describe photoexcitation is two-dimensional: photoexcitation results in a two-step, sequential process where the first step involves solely isomerization of the datively-bonded THFs. This means that carefully considering the chemical identity and choosing the correct reaction coordinates are critical for understanding solution-phase photexcitation reactions: if one were to think only of the species as dissolved Na_2^+ without explicitly considering the solvent, there would be no easily-constructed potential energy surface that could readily explain the excited-state dynamics of this species.[11]

Figure 4.3 also leaves us with an interesting puzzle: why is the energy drop along the R coordinate nearly an order of magnitude larger for the (4,5) complex in solution than that for the same complex in the gas phase? The two sets of simulations differ only in the presence of additional classical solvent molecules, so somehow the presence of extra THF molecules leads to additional relaxation, but only after the initial photoisomerization reaction is complete. To understand where this additional energy relaxation comes from, in Figure 4.4 we plot the photofragment separation, R, and the total solvent coordination number of the complex (on a color scale) against time for the initial (4,5) complex in both liquid THF (panel a) and as a gas-phase complex (panel b). The THF coordination number is calculated using a counting coordinate[60, 61, 63, 64] based on the distance of the datively-bonded THF oxygen atom from the Na^+ core, as detailed below in the Methods section.

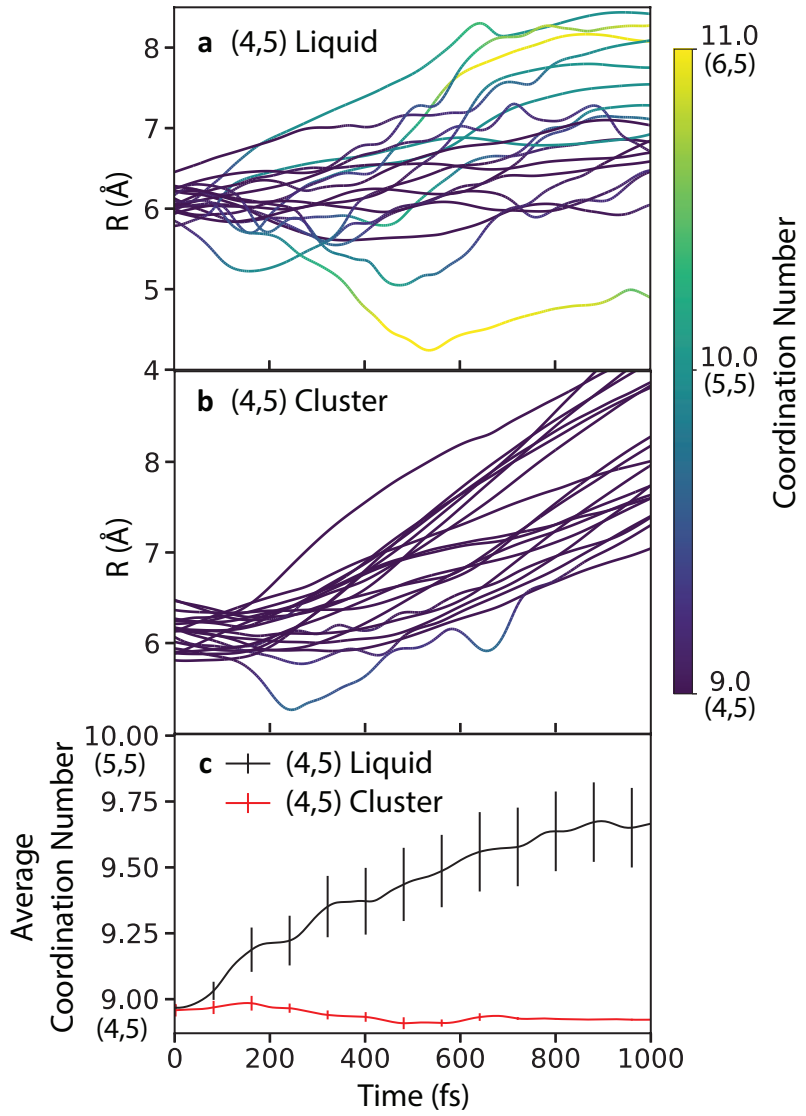

Figure 4.4: Plot of (4,5) fragment distance coordinate, R, following nonequilibrium photoexcitation with the color representing the total coordination number of datively-bonded THFs in (a) liquid THF and (b) as a gas-phase cluster. As the R coordinate for the (4,5) complex in liquid THF increases, panel (a) shows that the total THF coordination number increases, indicating a change in chemical identity to (5,5) and in a few cases, to (5,6). In panel (b), the (4,5) cluster coordination number cannot change with time because there are no additional solvent molecules with which to coordinate. Panel (c) plots the nonequilibrium ensemble average of the THF coordination number for the initially (4,5) complex in the liquid (black curve) and as a gas-phase cluster (red curve). The additional complexation in the liquid is what leads to the extra dissociative driving force seen in Fig. 4.3a.

Figure 4.4b shows that the gas-phase (4,5) complex does not change its THF coordination with time, which makes sense given that the complex is isolated in the gas phase. The situation is quite different, however, when the (4,5) complex is photoexcited in liquid THF. Figure 4.4a shows that once the isomerization is complete, THF molecules from the surrounding solvent can begin to datively coordinate with the solute, so that the solute coordination state changes from (4,5) to (5,5) in about half of the nonequilibrium trajectories, and in roughly 10% of the trajectories, the coordinate state can further change to (6,5). The additional solvation energy that accompanies higher-coordinated complexes, is what results in the additional energy drop along the R coordinate following photoexcitation in the liquid vs. that in the gas phase. In other words, the energy difference is the result of the solute chemical identity changing on-the-fly during the photoreaction, effectively converting the system from a (4,5) to (5,5) surface that has a lower zero of energy.

4.3 Conclusions

In summary, we performed nonequilibrium excited-state simulations via MQC MD that show that viewing weakly-interacting solvent molecules as a part of the chemical identity of the solute is important to understand simple photoexcitation reactions in solution. The simulations show that the the solvent plays an intimate role in the breaking of solution-phase chemical bonds. For our reaction of interest, it is clear that what originated as a photodissociation reaction of Na_2^+ in the gas phase is better understood as a two-step, sequential process of a solvated (4,5) complex, with the first step being an isomerization reaction that must be completed before the second, weakly dissociative step, can take place.

We close by noting that it certainly should be possible to experimentally detect the solvent effects described above. In previous work, we argued that one could create $Na_2(THF)_n^+$ species either in mass-selected gas-phase clusters or via pulse radiolysis in solution, and that the different complexes present at equilibrium could be separated by transient hole-burning.[60] Since the photoisomerization step involves rotation of the transition dipole between ground and excited state of the complex, one should be able to use polarized transient absorption spectroscopy to directly observe the isomerization reaction. This would allow direct interrogation of the role of the solvent in chemical bond breaking reactions in solution. We certainly expect that the solvent effects

on chemical identity described above will apply generally to bond breaking and bond formation reactions in solution.

4.4 Methods

4.4.1 Mixed Quantum/Classical Molecular Dynamics

In the MQC MD simulations the Na^+ cores and the THF solvent molecules are treated classically while the bonding electron of the solute is treated quantum mechanically. The quantum mechanical electron is treated on a basis of 64^3 grid points that span the entire simulation box. The time independent Schrödinger is solved for the bonding electron at each timestep. Interactions between the electron–Na^+ core and electron–THF solvent molecules are treated using pseudopotentials that have been previously developed and thoroughly benchmarked.[59, 62, 64, 81] The quantum electron contribution to the dynamics is accounted for through the Hellman-Feynman force.

The system is composed of two Na^+ cations bound by a single quantum mechanical electron and 254 THF solvent molecules (in the liquid phase). The box size is 32.5^3 cubic angstroms to match the experimental density of THF (0.89 g/mL at ∼298 K) with periodic boundary conditions. A timestep of 4 fs was used with the velocity Verlet algorithm to propagate dynamics and all simulations were performed on the (N, V, E) ensemble at 298 K.

4.4.2 Set Up of Nonequilibrium Ensemble

All data presented in this work are from a set of 20 nonequilibrium trajectories for each stable Na_2^+/THF complex, (4,5) and (5,5), both in liquid THF and as gas-phase clusters. The trajectories start with uncorrelated equilibrium configurations and at time zero the bonding electron is promoted into the first electronic excited state, initiating nonequilibrium photodissociation dynamics. For trajectories in the liquid phase, the simulations were run for a total of 5 ps and trajectories for the gas-phase clusters were run for 3 ps.

4.4.3 Molecular Geometry Coordinate

We analyzed the dynamics of our solvated complexes using a molecular geometry order parameter, h, based on the interior angles ($\angle O_{THF}$-Na^+-O_{THF}) of the solute–solvent complex. We start by

defining the sum of the squares of the angle deviations from an 'ideal' geometry, $\phi(t)$:

$$\phi(t) = \sum_i (\theta_i(t) - \alpha_i)^2, \tag{4.1}$$

where θ is the angle for the solvent configuration at time t, α is the angle of the ideal final structure (either 109.5° for tetrahedral or 90° or 120° for a trigonal bipyramidal structure), and i iterates through all interior angles of the solute–solvent complex. With $\phi(t)$ in hand, we then define our solvent geometry order parameter $h(t)$ by applying a logistic function to classify the configurations:

$$h(t) = \frac{1}{1 + \exp[\kappa(\phi(t) - \frac{1}{2}\sum_i (\alpha_i - \beta_i)^2)]}, \tag{4.2}$$

where β_i is one of the ideal angles for either the seesaw or square pyramid initial geometry and κ is a scaling parameter, with $\kappa^{-1} = 714$ degrees^2 for seesaw to tetrahedral and $\kappa^{-1} = 570$ degrees^2 for square pyramid to trigonal bipyramid geometries. With this definition, $h(t)$ has a value of 0 when the local geometry is seesaw on the 4-coordinate side and square pyramid on the 5-coordinate side, and a value of 1 for the corresponding tetrahedral and trigonal bipyramid geometries. The values of $h(t)$ shown in figures 2 and 3 result from averaging across both ends of the molecule.

4.4.4 Energy Surfaces

The blue shaded energy surfaces in Fig. 4.3 represent the enthalpy of the solute–solvent complex during the nonequilibrium dynamics. They are constructed by taking the sum of the Na^+–Na^+, Na^+–THF, and THF–THF classical potential energies and the energy of the quantum mechanical bonding electron. Effectively, the enthalpy is then binned against the molecular geometry, h, and the photofragment distance, R, to create an energy surface. The orange curve is the ensemble average (in other words the time average) of the 20 nonequilibrium trajectories.

4.4.5 Coordination Number Coordinate

For determining whether or not a THF molecule is part of the solute complex, we define a continuous coordination number, n_{Na^+}, as

$$n_{Na^+} = \sum_i S(|r_{O,i} - r_{Na^+}|), \tag{4.3}$$

where i runs over every THF oxygen site and r_{Na^+} and $r_{O,i}$ are the positions of the Na^+ core and the ith oxygen site, respectively. We then define a counting function, $S(r)$, as

$$S(r) = \frac{1}{1 + \exp[\kappa(r - r_c)]}, \tag{4.4}$$

where r_c is a cutoff radius that determines when a solvent molecule is coordinated to the Na^+, and κ^{-1} is the width of the transition region where the function switches from 1 to 0 around r_c. For this work, we selected $\kappa^{-1} = 0.2$ Å and $r_c = 3.65$ Å, corresponding to the first minimum of the Na^+-THF oxygen site $g(r)$. These values are similar to those used by our group in previous publications[11, 60, 61, 64] but have been slightly re-optimized to better represent the complexation of the Na_2^+ molecule.

4.5 Supplementary Information

4.5.1 Simulation Details

Mixed Quantum/Classical Model

Our mixed quantum/classical (MQC) molecular dynamics (MD) simulations consisted of two classical Na^+ cations, one fully quantum mechanical electron, and 254 classical tetrahydrofuran (THF) solvent molecules contained in a 32.5 $Å^3$ simulation cell. The size of the simulation cell was chosen to reproduce the appropriate solvent density at the simulation temperatures (0.89 g/mL at 298 ± 6 K for THF simulations). THF molecules were treated as rigid, planar five-membered rings following the work of Chandrasekar and Jorgensen.[86] This rigid planarity was enforced using the RATTLE algorithm, as in our previous MQC MD work.[61, 64] In all simulations, periodic boundary conditions were implemented with minimum image convention[82] and all interactions were

tapered smoothly to zero at 16 Å over a 2 Å range with a center of mass-based switching function according to Steinhauser.[84] All simulations were performed in the microcanonical ensemble.

Because all interactions were taken to be pair-wise additive, the full Hamiltonian of the system is $\hat{H} = H^{\mathrm{cl}} + \hat{H}^{\mathrm{qm}}$. In atomic units, the classical portion of the Hamiltonian is given by

$$H^{\mathrm{cl}} = \frac{1}{2} m_{\mathrm{Na^+}} \sum_{i=1}^{2} v_{\mathrm{Na^+}_i}^2 + \frac{1}{2} m_{\mathrm{solv}} \sum_{i=1}^{n_{\mathrm{solv}}} v_{\mathrm{solv}_i}^2 + U^{\mathrm{Na^+-Na^+}}(|\boldsymbol{R}_{\mathrm{Na^+}_1} - \boldsymbol{R}_{\mathrm{Na^+}_2}|) + \sum_{i=1}^{n_{\mathrm{solv}}} \sum_{j>i}^{n_{\mathrm{solv}}} U^{\mathrm{solv-solv}}(|\boldsymbol{R}_{\mathrm{solv}_i} - \boldsymbol{R}_{\mathrm{solv}_j}|) + \sum_{i=1}^{2} \sum_{j=1}^{n_{\mathrm{solv}}} U^{\mathrm{Na^+-solv}}(|\boldsymbol{R}_{\mathrm{Na^+}_i} - \boldsymbol{R}_{\mathrm{solv}_j}|) \quad (4.5)$$

where $v_{\chi_{\mathrm{i}}}$ is the velocity of the i^{th} sodium ($\chi = \mathrm{Na^+}$) or solvent molecule ($\chi = \mathrm{solv}$) at position $\boldsymbol{R}_{\chi i}$ and mass m_χ. $U^{\chi-\gamma}$ is a classical potential between atom types χ and γ ($\chi, \gamma = \mathrm{Na^+}$ or solv).

The quantum Hamiltonian is given by

$$\hat{H}^{\mathrm{qm}} = \frac{\hat{\boldsymbol{p}}_i^2}{2} + \sum_{j=1}^{2} V^{\mathrm{Na^+}}(|\boldsymbol{R}_{\mathrm{Na^+}_j} - \hat{\boldsymbol{r}}_i|) + \sum_{j=1}^{n_{\mathrm{solv}}} V^{\mathrm{solv}}(|\boldsymbol{R}_{\mathrm{solv}_j} - \hat{\boldsymbol{r}}_i|) \quad (4.6)$$

where $\hat{\boldsymbol{p}}_i$ and $\hat{\boldsymbol{r}}_i$ are the momentum and position operators for electron i, respectively, and V^χ is the pseudopotential representing the interaction between an electron and atom type χ.

For the MQC studies, the classical interaction between the two $\mathrm{Na^+}$ cations was modeled through a point-charge Coulomb potential, $U^{\mathrm{Na^+-Na^+}}(R) = 1/R$, since the short-range repulsion between the cores is negligible around the internuclear separation of $\mathrm{Na_2^+}$.

All classical interactions were modeled with Lennard-Jones potentials:[82]

$$u_{ij}(r_{ij}) = \frac{1}{4\pi\epsilon_0} \frac{q_i q_j}{r_{ij}} + 4\epsilon_{ij} \left[\left(\frac{\sigma_{ij}}{r_{ij}} \right)^{12} - \left(\frac{\sigma_{ij}}{r_{ij}} \right)^{6} \right] \quad (4.7)$$

where r_{ij} is the distance between the i^{th} and j^{th} solvent/$\mathrm{Na^+}$ site, q_i is the charge on the i^{th} site, ϵ_{ij} is the potential well depth, and σ_{ij} is the finite distance at which the inter-particle potential is zero. The Lennard-Jones parameters used in this study are listed in Supplementary Table 1. The standard Lorentz-Berthelot combining rules were also used to calculate the solute-solvent site and solvent site-solvent site interactions in THF.[82]

	σ (Å)	ϵ (kJ/mol)	q (e)
THF-oxygen	3.0	0.71	–0.5
THF-α-methyl	3.8	0.49	+0.25
THF-β-methyl	3.905	0.49	0.0
Na^+	1.67	22.07	+1.0

Table 4.1: **Lennard-Jones and Coulomb Potential Parameters for the Solute-Solvent Systems Studied in This Work.**

Phillips Kleinman (PK) pseudopotentials were used to account for the interactions between the classical particles and the quantum mechanical electrons.[55] These PK potentials were modified with polarization potentials to correct for the frozen core approximation implicit in PK formalism.[58, 59, 89] For $V^{e^- - \mathrm{Na}^+}$ and $V^{e^- - \mathrm{THF}}$, we used rigorously-derived psedopotentials previously developed by our group, the details of which can be found in Refs. 58 and 59, respectively. The final pseudopotential fits are presented here in Supplementary Tables 2 and 3.

Simulation Setup

The eigenstates of the quantum mechanical valence bonding electron were expanded on a three dimensional grid. We used a 64 × 64 × 64 × 64 grid that spanned the entire simulation box of dimensions 32.5 Å × 32.5 Å × 32.5 Å. These dimensions were chosen to keep the basis set as small as possible while still capturing the spatial extent of the electronic wave function. We centered the grid in the middle of the simulation cell and shifted all classical particles relative to the grid every 500 fs to avoid leakage of the wave function off the edges of the grid. In this way, the wave function was always located roughly in the center of the simulation cell. The classical particles were shifted an integer number of grid spaces to avoid discontinuities in the quantum energy that would prevent total energy of the simulation from being conserved.[62] We used the velocity Verlet algorithm[82] to propagate the classical degrees of freedom ($\boldsymbol{v}_{\mathrm{Na}^+{}_i}$, $\boldsymbol{v}_{\mathrm{solv}_i}$, $\boldsymbol{R}_{\mathrm{Na}^+{}_i}$, and $\boldsymbol{R}_{\mathrm{solv}_i}$) of the Hamiltonian in Eqs. 1 and 2 in the microcanonical (N, V, E) ensemble. We determined the forces from the sum of the classical-classical and classical-quantum interactions described above. We used the implicit restart Lanczos method to iteratively solve the time independent Schrödinger equation for the ground state wavefunction at every 4 fs time step.[85] The quantum forces on the classical

i	c_i (a.u.)	α_i (a.u.)
1	-16.3145	0.124293
2	0.0455219	0.0322129
3	16.3213 81	0.124181

Table 4.2: **Parameters used in the construction of the sodium-electron pseudopotential,** $\phi(r) = \sum_{i=1}^{3} c_i e^{-\alpha_i r^2}$**.** Further details of the sodium-electron pseupotential can be found in Ref 58.

$$U_{fit}(\mathbf{r}) = \left\{ \begin{array}{lllllllll} & U_o & + & U_{c\alpha 1} & + & U_{c\alpha 2} & + & U_{c\beta 1} & + & U_{c\beta 2} \\ + & U_{h\alpha 1} & + & U_{h\alpha 2} & + & U_{h\alpha 3} & + & U_{h\alpha 4} & + & U_{h\beta 1} \\ + & U_{h\beta 2} & + & U_{h\beta 3} & + & U_{h\beta 4} & + & U_{ao} & + & U_{ao} \\ + & U_{ac} & + & U_{ac} & + & U_{aa} & + & U_{af} & & \end{array} \right.$$

$$U_o(\mathbf{r}-\mathbf{r_o}) = \begin{array}{ll} & \left(o_1(x-x_o)^4 + o_2(y-y_o)^4 + o_3(z-z_o)^4 - o_4\right) \\ \times & exp\left(-\left[o_5(x-x_o)^2 + o_6((y-y_o)^2 + (z-z_o)^2)\right]\right) \\ + & o_7 \frac{e^{-o_8(\mathbf{r}-\mathbf{r_o})^2}}{|\mathbf{r}-\mathbf{r_o}|} \end{array}$$

$o_1 = 2.8926$	$o_2 = 0.1017$	$o_3 = 1.9379$	$o_4 = 4.1887$
$o_5 = 1.0552$	$o_6 = 1.2853$	$o_7 = 9.4147$	$o_8 = 23.4135$

$$U_{c\alpha}(\mathbf{r}-\mathbf{r_{c\alpha}}) = \begin{array}{ll} & c_1^\alpha\left[(y-y_{c\alpha}) + c_2^\alpha(z-z_{c\alpha})\right] \\ \times & exp\left(-\left[c_3^\alpha(x-x_{c\alpha})^2 + c_4^\alpha((y-y_{c\alpha})^2 + (z-z_{c\alpha})^2)\right]\right) \\ - & c_5^\alpha \frac{1}{|\mathbf{r}-\mathbf{r}_{c\alpha}|} + c_6^\alpha exp\left[-c_7^\alpha(\mathbf{r}-\mathbf{r}_{c_\alpha})^4\right] \end{array}$$

$c_1^\alpha = 62.6462$	$c_2^\alpha = 0.1426$	$c_3^\alpha = 7.9044$	$c_4^\alpha = 7.9516$
$c_5^\alpha = 0.3147$	$c_6^\alpha = 6.3821$	$c_7^\alpha = 34.2773$	

$$U_{c\beta}(\mathbf{r}-\mathbf{r_{c\beta}}) = \begin{array}{ll} & c_1^\beta\left[(y-y_{c\beta}) + c_2^\beta(z-z_{c\beta})\right] \\ \times & exp\left[-\left(c_3^\beta(x-x_{c\beta})^2 + c_4^\beta((y-y_{c\beta})^2 + (z-z_{c\beta})^2)\right)\right] \\ - & c_5^\beta \frac{1}{|\mathbf{r}-\mathbf{r}_{c\beta}|} + c_6^\beta e^{-c_7^\beta(\mathbf{r}-\mathbf{r}_{c\beta})^4} \end{array}$$

$c_1^\beta = 13.3107$	$c_2^\beta = 1.3455$	$c_3^\beta = 5.3624$	$c_4^\beta = 4.4085$
$c_5^\beta = 0.3033$	$c_6^\beta = 1.4495$	$c_7^\beta = 7.8897$	

$$U_{h\alpha}(\mathbf{r}-\mathbf{r_{h\alpha}}) = -h_1^\alpha \frac{exp\left[-h_2^\alpha(\mathbf{r}-\mathbf{r}_{h\alpha})^2\right]}{|\mathbf{r}-\mathbf{r}_{h\alpha}|} + h_3^\alpha exp\left[-h_4^\alpha(\mathbf{r}-\mathbf{r}_{h\alpha})^2\right]$$

$h_1^\alpha = 0.8357$	$h_2^\alpha = 0.8769$	$h_3^\alpha = 0.2657$	$h_4^\alpha = 0.0852$

$$U_{h\beta}(\mathbf{r}-\mathbf{r_{h\beta}}) = -h_1^\beta \frac{exp\left[-h_2^\beta(\mathbf{r}-\mathbf{r}_{h\beta})^2\right]}{|\mathbf{r}-\mathbf{r}_{h\beta}|} + h_3^\beta exp\left[-h_4^\beta(\mathbf{r}-\mathbf{r}_{h\beta})^2\right]$$

$h_1^\beta = 0.7861$	$h_2^\beta = 0.9584$	$h_3^\beta = 0.1362$	$h_4^\beta = 0.0359$

$$U_{ao}(\mathbf{r}-\mathbf{r_{ao}}) = a_1^o exp\left[-\left(a_2^o(x-x_{ao})^2 + a_3^o(y-y_{ao})^2 + a_4^o(z-z_{ao})^2\right)\right]$$

$a_1^o = 2.7673$	$a_2^o = 1.0552$	$a_3^o = 0.5211$	$a_4^o = 0.7436$

$$U_{ac}(\mathbf{r}-\mathbf{r_{ac}}) = a_1^c exp\left[-\left(a_2^c(x-x_{ac})^2 + a_3^c((y-y_{ac})^2 + (z-z_{ac})^2)\right)\right]$$

$a_1^c = 0.9996$	$a_2^c = 0.6810$	$a_3^c = 0.3058$	

$$U_{aa}(\mathbf{r}-\mathbf{r_{aa}}) = \begin{array}{ll} & a_1^a exp\left[-\left(a_2^a(x-x_{aa})^2 + a_3^a((y-y_{aa})^2 + (z-z_{aa})^2)\right)\right] \\ - & a_4^a exp\left[-\left(a_5^a(x-x_{aa})^2 + a_6^a((y-y_{aa})^2 + (z-z_{aa})^2)\right)\right] \end{array}$$

$a_1^a = 11.7043$	$a_2^a = 0.5978$	$a_3^a = 0.1703$	
$a_4^a = 10.7099$	$a_5^a = 0.5994$	$a_6^a = 0.1597$	

$$U_{af}(\mathbf{r}-\mathbf{r_{af}}) = a_1^f exp\left[-\left(a_2^f(x-x_{af})^2 + a_3^f(y-y_{af})^2 + a_4^f(z-z_{af})^2\right)\right]$$

$a_1^f = 0.4472$	$a_2^f = 0.0443$	$a_3^f = 0.0379$	$a_3^f = 0.2579$

Table 4.3: **Functional Form and Parameters of the Fit to the Exact e$^-$–THF Effective Potential.** The 47-parameter fit has functional contributions centered on 19 different sites. The functional and parameter notations are explained in Ref 59. For the parameters given here, the distances are in Bohr radii and the energies are in Hartrees.

particles were then found using the Hellman-Feynman theorem:

$$\boldsymbol{F}_i^Q = -\langle\Psi|\,\nabla_{\boldsymbol{R}_i}\hat{H}\,|\Psi\rangle \tag{4.8}$$

where, $\boldsymbol{F}_i^Q$ is the quantum force on classical particle i at position $\boldsymbol{R}_i$. Because the wave function is expanded in a basis that does not functionally depend on the position of the classical particles, Eq. 4 is exact (in other words, there are no issues with Pulay forces from the basis functions changing with time).[81]

For this paper, we collected data by placing the Na_2^+ molecule into the first excited state from uncorrelated equilibrium ground state configurations and then allowed the molecule to propagate adiabatically on its electronic excited state. Because ground state Na_2^+ is stabilized in two primary coordination states in THF, we selected starting configurations for each. For the $Na(THF)_4$–$Na(THF)_5^+$ species, the equilibrium bond length is ∼4.8 Å and for the $Na(THF)_5$–$Na(THF)_5^+$ species the equilibrium bond length is ∼5.6 Å. Twenty dissociation trajectories were run for each of the two $Na_2(THF)_n^+$ coordination states.

In the next section, we will discuss additional data that were not included in the paper.

4.5.2 Additional Data

Potentials of Mean Force

Na_2^+ in THF exists as a mixture of two solute-solvent complexes, $Na(THF)_4$–$Na(THF)_5^+$ and $Na(THF)_5$–$Na(THF)_5^+$, referred to as the (4,5) and (5,5) in the main text.[61] Using umbrella sampling,[116] we calculate a potential of mean force (PMF) for the (4,5) and (5,5) complexes as a function of Na^+–Na^+ length, the conventional order parameter of dissociation reactions. This is done by applying a biasing potential to adequately sample high energy configurations with equilibrium fluctuations. Here we apply a bias potential, $U(x)$, to both the Na^+–Na^+ distance and coordination state,

$$U(\boldsymbol{x}) = \frac{1}{2}k(\boldsymbol{x}-\zeta)^2 \tag{4.9}$$

where x is either Na^+–Na^+ distance or coordination number, ζ is either target Na^+–Na^+ distance or target coordination number, and k is a spring constant. Since the form of $U(r)$ is known, the statistics of the unbiased system can be recovered from the biased statistics. By constraining the system to a coordination number (either (4,5) or (5,5)), we can sample various Na^+–Na^+ distances to calculate the free energy along this coordinate for a single species using the multistate Bennet acceptance ratio method.[83]

The PMF of the (4,5) and (5,5) species can be seen in Supplementary Figure 1, where the free energy is calculated for the ground state (GS) and first excited state (FES) along the Na^+–Na^+ distance coordinate. The free energy minimum of the (5,5) GS is used as the zero energy reference point for these curves and the (4,5) GS curve is adjusted using the previously calculated Boltzmann weight of the (4,5) and (5,5) species.[60] The (4,5) FES and (5,5) FES curves are then adjusted to match the average excitation energy of the (4,5) and (5,5) species starting from the ground state. While the PMFs approximate the dissociative nature of the FES, these equilibrium predictions do not show the nonequilibrium dynamics that actually occur in photodissociation[11] or the photoisomerization step discussed in the main text. Therefore, the second reaction coordinate involving only motions of the solvent molecules, is required for a more complete picture of the nonequilibrium dynamics.

(5,5) Molecular Geometry

In the main text we analyze the dynamics following the photoexcitation of (4,5), and state that the data for (5,5), follow similar trends and omitted the data for the (5,5) complex from the main text for brevity. Here we show that data starting with the evolution of the solvent geometry.

Like the (4,5) molecule shown in the main text, Supplementary Figure 2 shows the (5,5) molecule changing geometry from square pyramid to trigonal bipyramid in the first ∼200 fs and that this change in geometry is coincident with a rotation of the excited state node. These trends are true for both the liquid case (a) and the cluster (b). In other words, after photoexcitation, the motions of the datively-bound solvent molecules are directly tied to the rotation of the node in the bonding electron's wavefunction. Since the Na^+–Na^+ bond length does not change during this solvent rearrangement, as discussed further below, we refer to the dynamics during this ∼200-fs window as a photoisomerization process, just like the (4,5) molecule.

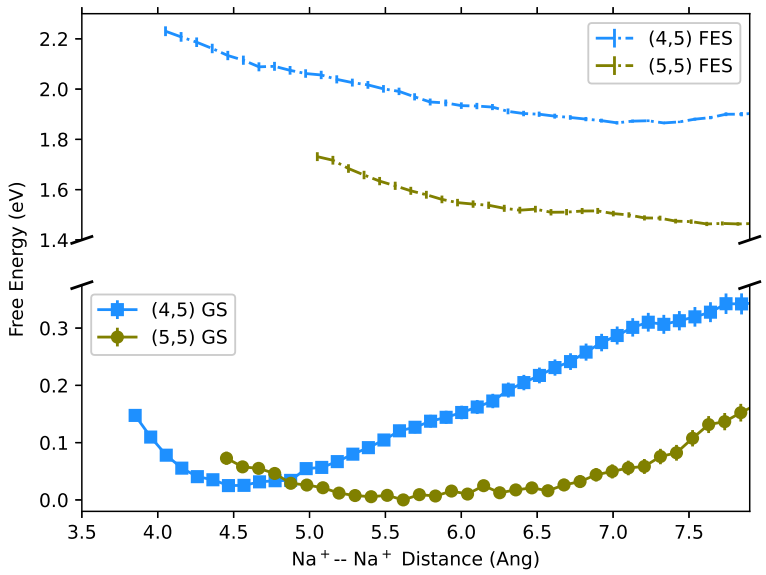

Figure 4.5: Potential of mean force for the (4,5) and (5,5) species in liquid THF on their respective ground (blue squares and green circles) and first excited states (blue and green "$-\cdot$" lines). Each data point corresponds to an equilibrium trajectory biased at the target coordination state and Na^+–Na^+ distance. The ground state (GS) PMF curves show a crossing between the (4,5) and (5,5) species, coinciding with a mixture of both solute-solvent complexes being stable. The first excited state (FES) curves predict both species as immediately dissociative, however, the first $\sim$200 fs follwing photoexcitation are not dissociative, as described in the main text. The excited state PMFs also do not include the isomerization step of first-shell solvent molecules seen in the nonequilibrium dynamics.

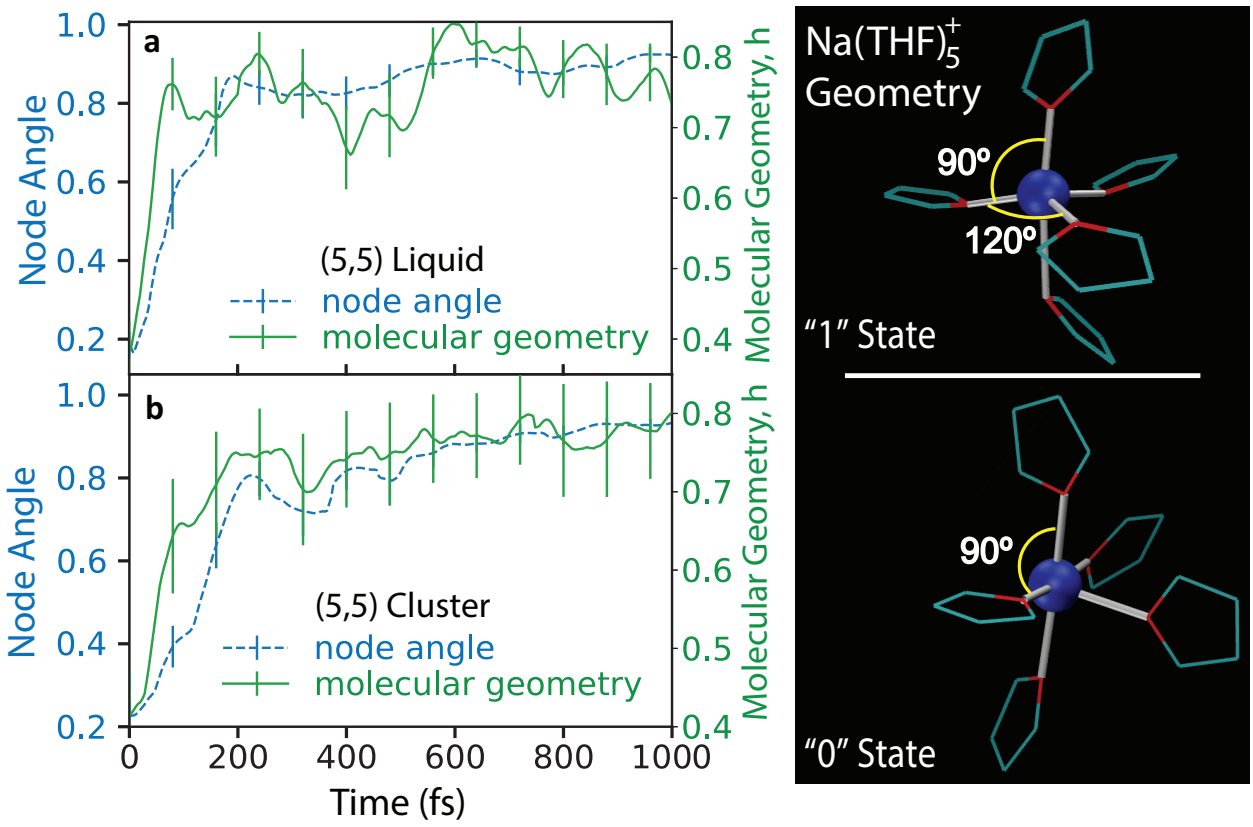

Figure 4.6: nonequilibrium ensemble average dynamics of the molecular geometry, h (green curves), and node angle (dashed blue curves) of the (5,5) species following photoexcitation. Panel (a) shows the molecular geometry and node angle evolution for the (5,5) complex in liquid THF, while panel (b) shows the same for the (5,5) gas-phase cluster. In both cases, there is a significant change in the molecular geometry over the first ∼200 fs that is correlated with a change in the node angle. The right panel illustrates the ideal molecular geometry states of $Na(THF)_5^+$ with the $h = 0$ equating to a square pyramidal state and $h = 1$ equating to a trigonal bipyramidal state. Error bars are $\pm 2\sigma$.

In comparing quantitative differences between the (4,5) and (5,5) molecule, it may appear that the correlation between node angle and molecular geometry change is higher in the (4,5) case. However, given the size of the error bars we are hesitant to suggest that the molecular geometry coordinate evolves significantly faster in the (5,5) case: while there may be a numerical difference between these two species, qualitatively they exhibit similar behavior given the level of precision available with only 20 nonequilibrium trajectories.

(5,5) Energy Surface

The main text defines a dissociation parameter, R, and uses it to create a two-dimensional energy surface with the molecular geometry parameter, h, as the other axis. Like figure 3 of the main text,

Supplementary Figure 3 shows two-dimensional energy surfaces but for the (5,5) molecule with panel (a) showing the dynamics in liquid THF and panel (b) showing that as a gas-phase cluster. The h, R-coordinate space is sampled using 20 nonequilibrium photodissociation trajectories. At each 4-fs time step, the molecular geometry, h, and photofragment distance, R, are calculated and binned with the enthalpy to create a 2D energy surface. The number of values in each bin depend on how often the trajectories in our nonequilibrium ensemble visit each (h, R) pair. For the initial motion along the h-coordinate, i.e. along the isomerization step, there are, on average, 37 samples per bin, and for the subsequent motion along the R-coordinate, i.e. the weakly dissociative step, there are, on average, 181 samples per bin. Given the number of samples and how the time-averaged trajectory (orange line) is calculated, the bins along the isomerization step are not as accurate. The time-averaged trajectory averages over a fairly wide distribution of initial configurations at early times for smaller values of h and R; these configurations are not shown on the energy surface due to insufficient statistics. This averaging, however, causes the time-averaged energy at early times to be greater than that apparent on the 2-D surface, leading the appearance that the orange non-equilibrium average trajectory resides 'above' the energy surface.

The right side of Supplementary Figure 2 shows a 'top-down' view of the nonequilibrium average behavior with the enthalpy shown using a color bar. Like what was argued in the main text for the (4,5) molecule, when the (5,5) molecule is photoexcited, the first ∼200 fs are spent rearranging the coordinating solvent molecules with almost no motion along the dissociation parameter, R. Only after the rearrangement, which we call isomerization in the main text, can the molecule move along the R. These sequence of events show that what once was a purely dissociative process for the diatomic molecule, Na_2^+, becomes a two-step process with the first being isomerization and the second being weakly dissociative.

(5,5) Coordination Number

The main text also shows how the total coordination number changes for the (4,5) molecule when in liquid THF and in the gas phase. In Supplementary Figure 4 we show the same for the (5,5) molecule. Whereas the (4,5) molecule in liquid THF starts with less coordinating THFs and eventually coordinates with surrounding solvents to form (5,5) and in some cases even (5,6), the initially (5,5) molecule does not coordinate with an additional surrounding solvent to form (5,6).

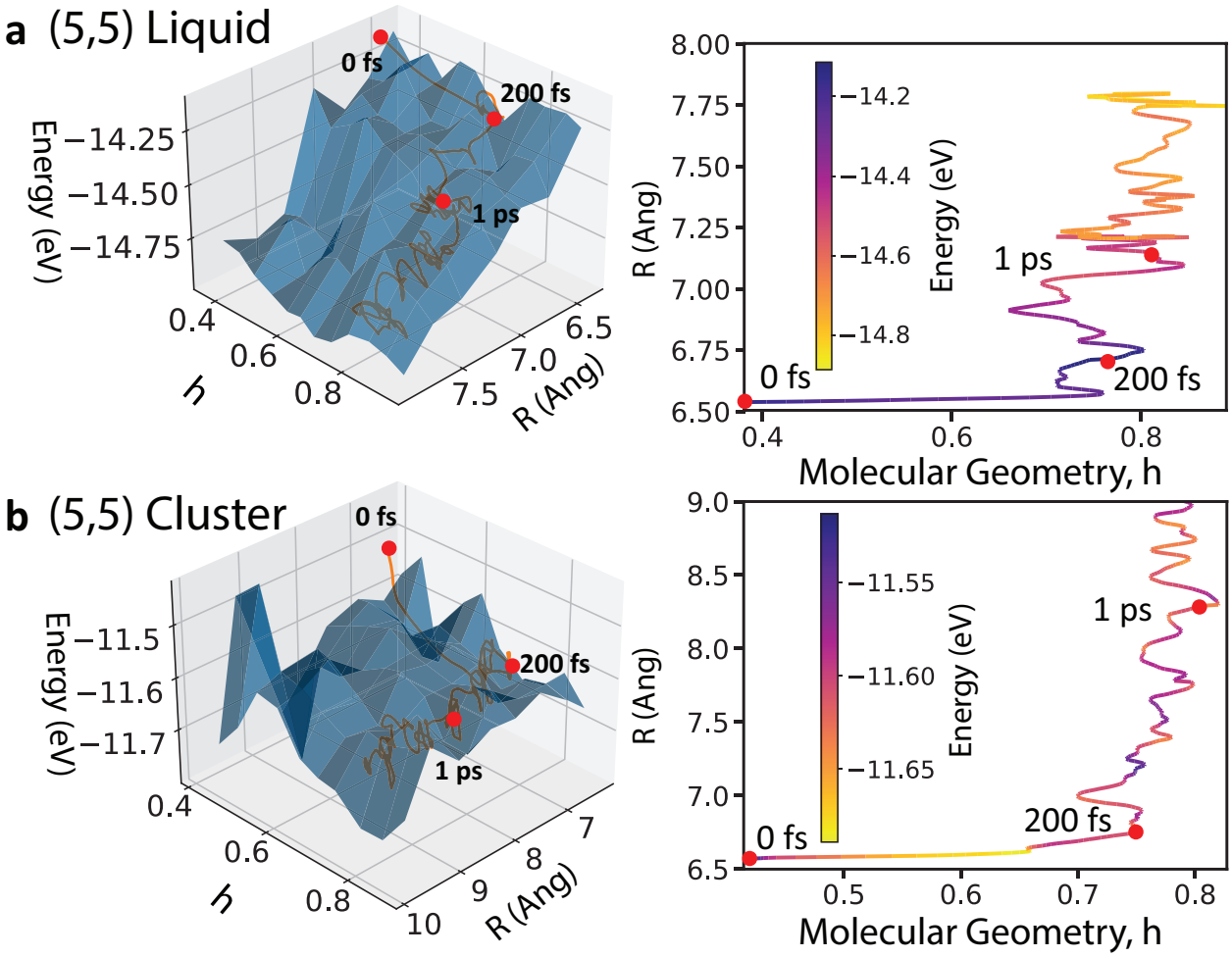

Figure 4.7: Two-dimensional energy surfaces (shown in blue in the left diagrams) with axes comprised of the datively-bonded solvent geometry, h, and the photofragment distance separation, R, for the nonequilibrium dynamics following photoexcitation of (5,5) in (a) liquid THF and (b) as a gas-phase cluster. The right diagrams show the same nonequilibrium average trajectory from a 'top-down' view with the color used to indicate the value of the energy. The time following photoexcitation is shown at a few select points. Clearly, the first ∼200-fs of the motion out of the Franck-Condon region is entirely along h, effectively a photoisomerization reaction that is associated with a ∼200 meV drop in energy. Only after the isomerization is complete can the system begin to move along the R dissociative coordinate. Dissociation of the gas-phase cluster in panel (b) is driven by only a ∼100 meV energy loss, while that of the (5,5) complex in the liquid in panel (a) is accompanied by ∼0.5 eV.

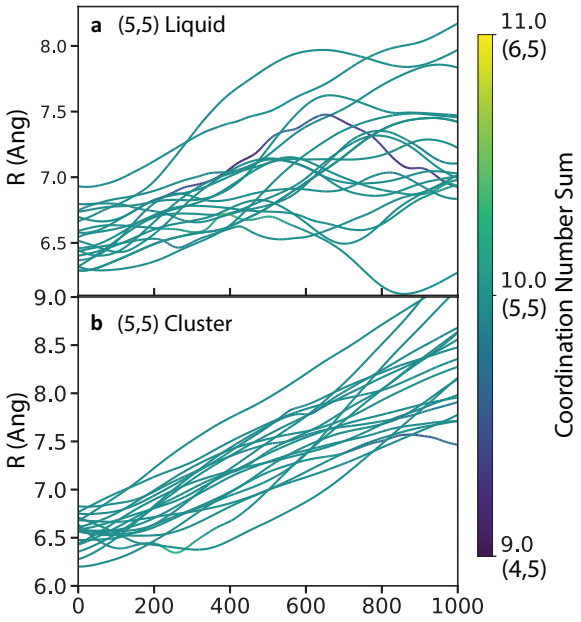

Figure 4.8: Plot of (5,5) fragment distance coordinate, R, following nonequilibrium photoexcitation with the color representing the total coordination number of datively-bonded THFs in (a) liquid THF and (b) as a gas-phase cluster. As the R coordinate for the (5,5) complex in liquid THF increases, panel (a) shows that the total THF coordination number remains the same. In panel (b), the (5,5) cluster coordination number also does not change with time.

This difference in behavior with initially (4,5) molecules occasionally forming (5,6) (but initially (5,5) not forming (5,6)) is the only qualitative difference in behavior between the (4,5) and (5,5) molecules. It appears that the solvent retains memory of the initial configuration even 1 ps following photoexcitation, as a (5,5) complex created from a (4,5) complex can sometimes go on to form a (6,5) complex, whereas we never see formation of (6,5) complexes starting with photoexcitation of an equilibrium (5,5) complex. Thus, there must be some kinetic barrier to creation of a new dative bond from the (5,5) complex that is avoided when the (5,5) complex is created in a nonequilibrium situation from a rapidly-dissociating (4,5) complex. Fortunately, this qualitative difference does not affect the conclusions of the main text.

Energy Gap Between Adiabatic States

Figure S5 shows nonequilibrium average eigenergies for the lowest 5 adiabatic states following photoexcitation of (4,5) and (5,5) complexes as both gas-phase clusters and in liquid THF. During the ∼200-fs isomerization process, the initially small energy gap between the first excited state (ϵ_1) and the second excited state (ϵ_2) rapidly increases to be $\geq$ 250 meV in all four cases. Both

the average and the individual trajectories show that there are no diabatic crossings between the initially-occupied state of Π_u character and a higher-lying state of σ_u character, which would be characterized by this energy gap tending toward zero. This also suggests that if non-adiabatic dynamics were employed, there would be few, if any, non-adiabatic transitions to higher lying excited states (most non-adiabatic dynamics algorithms reject upwards transitions if there is not enough kinetic energy along the classical non-adiabatic coupling vector to balance the electronic energy increase, so that large upward transitions virtually never happen). In addition, even though the isomerization reaction closes the energy gap between the ground (ϵ_0) and first excited (ϵ_1) states, this gap does remains $\geq$ 500 meV for all four cases even at times out to 1 ps. This means that the use of non-adiabatic dynamics would have only a small percentage of the trajectories hop to the ground state during this period, which would remove them from our ensemble and thus lower our statistics without effectively changing any of the observations or conclusions we reach. Thus, our use of adiabatic dynamics to explore how the node rotation and thus change in electronic character is driven by the solvent reorganization (Figs. 2 and 3 in the main text) is justified.

Movies of Photoinduced Bond-Breaking

Attached to the SI are movies of the photoinduced bond breaking of Na_2^+ in the gas phase as well as in liquid THF. The blue spheres represent the Na^+ cores and the isosurface represents the charge density of the bonding electron. Red and turquoise pentagons represent the THF solvent molecules. Movies were made using Visual Molecular Dynamics (VMD).[117] From the gas phase movie, we can see the bonding electron exhibits a node perpendicular to the bond axis immediately after photoexcitation, resembling a $\sigma*$ molecular orbital. For the entire duration of the bond breaking process the node remains in this orientation, as expected in a gas phase dissociation of a diatomic molecule. However, the bond breaking reaction in the condensed phase shows the initial bonding electron charge density parallel to the bond axis immediately after photoexcitation. This resembles a π molecular orbital rather than the σ^* molecular orbital seen in gas phase Na_2^+. It is not until the coordinating solvent molecules reorient to the change in electron density, that the node rotates to perpendicular of the bond axis giving the anti-bonding σ^* molecular orbital.

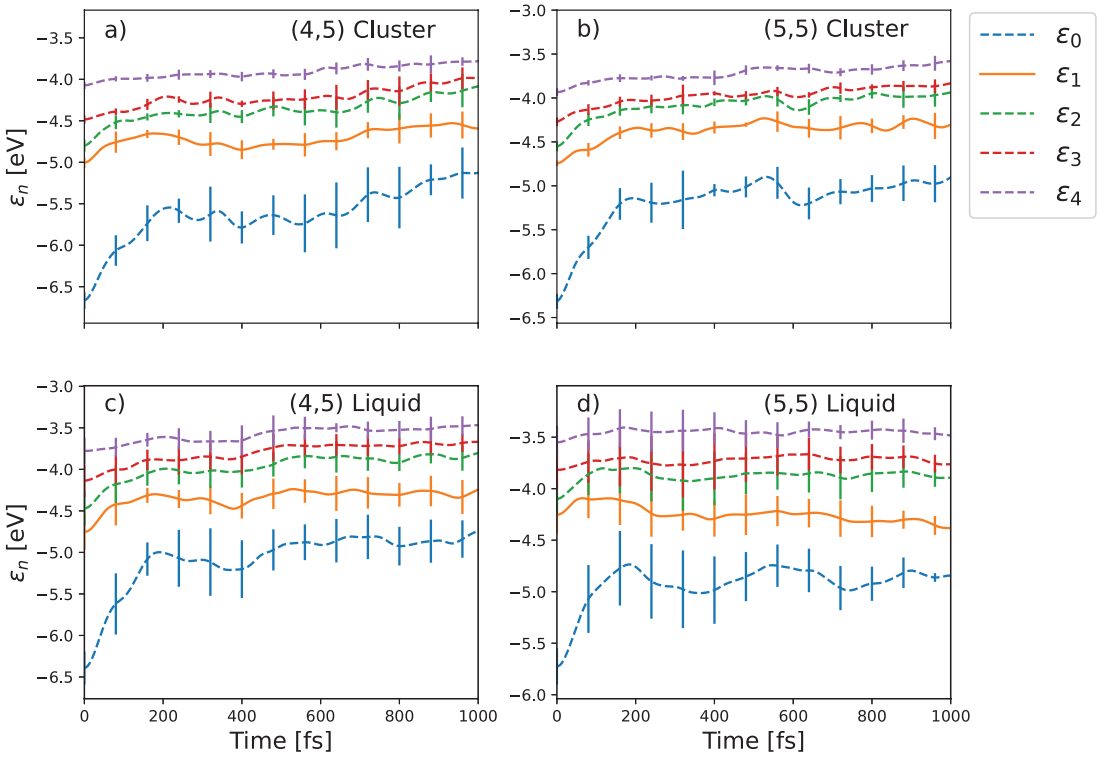

Figure 4.9: Average quantum energies for the first five adiabatic states for Na_2^+ in the clusters (panels a and b) and in liquid THF (panels c and d) for a subset of the trajectories. Dynamics are propagated on the first excited state (n=2), depicted in the solid orange line. The energy gap between the ground state during the node rotation (< 200 fs) suggests that nonadiabtic transitions onto the ground state are negligible due to the >500 meV difference in all solvent environments. The lack of crossings between the first excited (n=2) and second excited (n=3) states, suggest that the node rotation is a change in adiabatic character, rather than an inversion of states. Error bars are $\pm 1\sigma$.

Chapter 5

Conclusions

Both the average and fluctuational behavior of solvent-induced effects are necessary for thinking about solution-phase chemical reaction. The two common methods for constructing a solution-phase energy surface are to either inherit the gas-phase potential energy surface or to average the equilibrium solvent contribution in the potential of mean force. For molecularly "violent" reactions including photodissociation where solvent caging, a nonequilibrium solvent effect, dominates the dynamics, neither options are expected to adequately describe the solution-phase reaction. As for the solvent fluctuations, linear response is often applied to describe the nonequilibrium response using equilibrium calculations.

In Chapter 2 of the dissertation, using the photodissociation of Na_2^+ in liquid Ar and liquid THF, we compared the gas-phase energy surface and the potential of mean force against the nonequilibrium dynamics and found that, indeed, neither surfaces adequately represent the nonequilibrium solvent dynamics. Instead, a nonequilibrium, dynamical energy surfaced based on a time-integral of work expression does capture the nonequilibrium dynamics well, particularly for the case of Na_2^+ in liquid Ar. With Na_2^+ in Ar, this dynamical energy surface shows how solvent caging is mass dependent: when the solvent mass is appreciably smaller than the mass of the solute, the solvent can rearrange on a timescale faster than the timescale of solute motions and solvent caging is no longer observed. With Na_2^+ in THF, the same time-integral of work expression highlights how the identity of the solvent can change the reaction dynamics from a purely dissociative reaction (Na_2^+ in the gas-phase is purely dissociative), to one that is trapped and weakly dissociative. That said, the time-integral of work expression does not paint a clear, comprehensible picture of solution-phase

dynamics for the case of Na_2^+ in THF.

In Chapter 3, we look at how the solvent fluctuations change along the reaction coordinate for Na_2^+ in Ar. Surprisingly, the solute experiences a few distinct solvent environments and the transitions between each environment occur discretely. Moreover, the solvent environments encountered depend on the pathway taken, whether assuming the solvent is at equilibrium with the solute or not. We also test ideas of LR and no matter how LR is applied, nonstationary or otherwise, it does not hold. While we show that nonequilibrium response can not be predicted from equilibrium behavior and that the nonequilibrium response is nonstationary, it is also reassuring that the nonequilibrium fluctuations follow only a few response environments.

In Chapter 4, we revisit the case of Na_2^+ in THF and attempt to improve upon the dynamical energy surface by considering the motion of neighboring THF molecules. The moderate locally-specific solute-solvent interactions lead to Na_2^+ in THF as being better thought of as a solute-solvent complex, $Na_2(THF)_n^+$. To track the contribution of these datively bonded THF molecules, a second reaction coordinate was devised to follow the overall molecular geometry. With this molecular geometry coordinate, along with the natural reaction coordinate for dissociation, photofragment separation, a two-dimensional dynamical energy surface was constructed. This two-dimensional surface paints a clear picture of the reaction dynamics as a two-step sequential process with the first step being photoisomeration. By explicitly considering the dynamics of neighboring molecules, we have constructed a clear, comprehensible picture of the photodissociation dynamics of Na_2^+ in THF. At the same time, we directly highlight how solvents can have key, active contributions to solution-phase dynamics by providing molecular-level detail.

In summary, this work serves as a reference point for developing a theoretical framework for understanding solution-phase chemical reactions. Dynamical, nonequilibrium energy surfaces were constructed and compared to commonly used approaches to solution-phase energy surfaces, the gas-phase potential energy surface and potential of mean force. For two very different solvent systems, a time-integral of work expression unveils key nonequilibrium dynamics. When only the dissociating solute needs to be considered, such as in the case of Na_2^+ in liquid Ar, this expression also does very well in painting a clear picture of the reaction dynamics. When the solute is better thought of as a solute-solvent complex, such as in the case of Na_2^+ in liquid THF, incorporating the dynamics of the neighboring solvent into the energy surface allows for the construction of a higher-

dimensional energy surface that clearly captures the reaction dynamics. Aside from describing the average nonequilibrium behavior, we also detail how the nonequilibrium fluctuations can change discretely with the reaction coordinate. Fortunately, while we show that there are discrete solvent environments with distinct fluctuations, there are only a few environments even for a reaction that explores a large solvent configuration space.

Appendix

All code for running simulations and performing analysis can be found in a blue TOSHIBA external hard drive. Under the Andy/ folder can be found three directories: analysis/, Hoffman2/, and supermic/. All analysis was carried out using jupyter notebooks and the these notebooks can be found under the analysis/ folder. The Hoffman2/ folder contains all of my Hoffman2 data at the time exit. The supermic/ folder stores all of the .0data published in the dissertation chapters.

Some key files/folders in the TOSHIBA_EXT/Andy/analysis/ directory and their use are:

- change_m.ipynb, Na2+_Ar.ipynb, scratch_fes.ipynb, scratch_gnd.ipynb were all used for the time-integral work paper, Chapter 2 of the dissertation.
- electronic_structure_profile.ipynb, electronic_structure_profile2.ipynb, electronic_profile_structure.ipynb, egap_TCFs.ipynb, energy_gap.ipynb were all used for the solvent environments paper, Chapter 3 of the dissertation.
- Na2(THF)+_cluster.ipynb, Na2(THF)+_cluster2.ipynb, Na2(THF)+_liq.ipynb, Na2(THF)+_liq2.ipynb, Na2(THF)+_liq2_Sr.ipynb were all used for the photoisomerization paper, Chapter 4 of the dissertation.

All python scripts used for the analysis can either be found in the notebooks themselves or in one of the python libraries found in TOSHIBA_EXT/Andy/Hoffman2/python/

Some key files/folders in the TOSHIBA_EXT/Andy/Hoffman2/ directory and their use are:

- dev/ contains stable, up-to-date versions of Na_2^+ in code as of 8/19/2022. The three version of the code are Na_2^+ in liquid Ar, Na_2^+ in Ar clusters, and Na in liquid Ar. In each code the

bonding electron can be turned off to simulate Na_2^{2+} or Na^+. There are also README files that follow the progression of the code along with notes

- python/ contains all python libraries used for analysis. Some important libraries are 'dimer_dissoc_analysis.py' 'thf_dissoc_analysis.py', 'sm_fxns.py', and 'set_fxns.py.' The libraries contain comments on how to use the functions and what they are designed to do.
- bash/ contains bash scripts for submitting jobs

Some key files/folders in the TOSHIBA_EXT/Andy/supermic/ are:

- Na2+_Ar/{eqb_trj, inc_m, red_m} contain data used in Chapter 2
- Na2+_Ar/first_es/fssh/ contains all nonequilibrium dissociation trajectories
- Na2+_Ar/bond_umb/ contains all bond umbrella trajectories for mapping out the PMF with the electron on the ground state and the excited state

Bibliography

(1) Young, R. M.; Neumark, D. M. Dynamics of solvated electrons in clusters. *Chem. Rev.* **2012**, *112*, 5553–5577.

(2) Blandamer, M. J.; Fox, M. F. Theory and Applications of Charge-Transfer to Solvent Spectra. *Chem. Rev.* **1970**, *70*, 59–93.

(3) Mak, C. C.; Peslherbe, G. H. Relaxation Pathways of Photoexcited Iodide–Methanol Clusters: A Computational Investigation. *J. Phys. Chem. A* **2014**, *118*, 4494450.

(4) Liu, Q. L.; Wang, J. K.; Zewail, A. H. Femtosecond dynamics of dissociation and recombination in solvent cages. *Nature* **1993**, *364*, 427–430.

(5) Wang, W. N.; Nelson, K. A.; Xiao, L.; Coker, D. F. Molecular-dynamics simulation studies of solvent cage effects on photodissociation in condensed phases. *J. Chem. Phys.* **1994**, *101*, 9663–9671.

(6) Batista, V. S.; Coker, D. F. Nonadiabatic molecular dynamics simulations of the photofragmentation and geminate recombination dynamics in size-selected I_2^--Ar_n cluster ions. *J. Chem. Phys.* **1997**, *106*, 7102–7116.

(7) Bihary, Z.; Zadoyan, R.; Karavitis, M.; Apkarian, V. A. Dynamics and the breaking of a driven cage: I_2 in solid Ar. *J. Chem. Phys.* **2004**, *120*, 7576–7589.

(8) Douady, J.; Jacquet, E.; Giglio, E.; Zanuttini, D.; Gervais, B. Non-adiabatic molecular dynamics of excited Na_2^+ solvated in Ar_{17} clusters. *Chem. Phys. Lett.* **2009**, *476*, 163–167.

(9) Sheps, L.; Miller, E. M.; Horvath, S.; Thompson, M. A.; Parson, R.; McCoy, A. B.; Lineberger, W. C. Solvent-Mediated Electron Hopping: Long-Range Charge Transfer in $IBr^-(CO_2)$ Photodissociation. *Science* **2010**, *328*, 220–224.

(10) Zanuttini, D.; Douady, J.; Jacquet, E.; Giglio, E.; Gervais, B. Nonadiabatic molecular dynamics of photoexcited Li_2^+ Ne_n clusters. *J. Chem. Phys.* **2011**, *134*, 044308.

(11) Vong, A.; Widmer, D. R.; Schwartz, B. J. Nonequilibrium solvent effects during photodissociation in liquids: dynamical energy surfaces, caging, and chemical identity. *J. Phys. Chem. Lett.* **2020**, *11*, 9230–9238.

(12) Ishida, T.; Rossky, P. J. Consequences of strong coupling between solvation and electronic strucure in the excited state of a betaine dye. *J. Phys. Chem. B* **2008**, *112*, 11353–11360.

(13) Borgis, D.; Tarjus, G.; Azzouz, H. An adiabatic dynamical simulation study of the Zundel polarization of strongly H-bonded complexes in solution. *J. Chem. Phys.* **1992**, *97*, 1390.

(14) Jeanmairet, G.; Levesque, M.; Borgis, D. Tackling Solvent Effects by Coupling Electronic and Molecular Density Functional Theory. *J. Chem. Theory Comput.* **2020**, *16*, 7123–7134.

(15) Yamada, A.; Kojima, H.; Okazaki, S. A molecular dynamics study of intramolecular proton transfer reaction of malonaldehyde in solutions based upon mixed quantum-classical approximation. I. Proton transfer reaction in water. *J. Chem. Phys. 084509* **2014**, *141*, 084509.

(16) Kojima, H.; Yamada, A.; Okazaki, S. A molecular dynamics study of intramolecular proton transfer reaction of malonaldehyde in solution based upon a mixed quantum–classical approximation. II. Proton transfer reaction in non-polar solvent. *J. Chem. Phys.* **2015**, *142*, 174502.

(17) Ladanyi, B. M.; Hynes, J. T. Transition-State Solvent Effects on Atom Transfer Rates in Solution. *J. Am. Chem. Soc* **1986**, *108*, 585–593.

(18) Burghardt, I.; Hynes, J. T. Excited-State Charge Transfer at a Conical Intersection: Effects of an Environment. *J. Phys. Chem. A* **2006**, *110*, 11411–11423.

(19) Allen, T. W.; Andersen, O. S.; Roux, B. Molecular Dynamics – Potential of Mean Force Calculations as a Tool for Understanding Ion Permeation and Selectivity in Narrow Channels. *Biophys. Chem.*, *124*, 251–267.

(20) Iskrenova-Tchoukova, E.; Kalinichev, A. G.; Kirkpatrick, R. J. Metal Cation Complexation with Natural Organic Matter in Aqueous Solutions: Molecular Dynamics Simulations and Potentials of Mean Force. **2010**, *26*, 15909–15919.

(21) Heid, E.; Moser, W.; Schröder, C. On the validity of linear response approximations regarding the solvation dynamics of polyatomic solutes. *Phys. Chem. Chem. Phys.* **2017**, *19*, 10940–10950.

(22) Heid, E.; Schröder, C. Solvation dynamics in polar solvents and imidazolium ionic liquids: failure of linear response approximations. *Phys. Chem. Chem. Phys.*, *20*, 5246–5255.

(23) Bedard-Hearn, M. J.; Larsen, R. E.; Schwartz, B. J. Understanding nonequilibrium solvent motions through molecular projections: Computer simulations of solvation dynamics in liquid tetrahydrofuran (THF). *J. Phys. Chem. B* **2003**, *107*, 14464–14475.

(24) Bedard-Hearn, M. J.; Larsen, R. E.; Schwartz, B. J. Hidden breakdown of linear response: Projections of molecular motions in nonequilibrium simulations of solvation dynamics. *J. Phys. Chem. A.* **2003**, *107*, 4773–4777.

(25) Schile, A. J.; Thompson, W. H. Tests for, origins of, and corrections to non-Gaussian statistics: The dipole-flip model. *J. Chem. Phys.* **2017**, *146*, 154109–154109.

(26) Batista, V. S.; Coker, D. F. Nonadiabatic molecular dynamics simulation of photodissociation and geminate recombination of I_2 liquid xenon. *J. Chem. Phys.* **1996**, *105*, 4033–4054.

(27) Batista, V. S.; Coker, D. F. Nonadiabatic molecular dynamics simulation of ultrafast pump-probe experiments on I_2 in solid rare gases. *J. Chem. Phys.* **1997**, *106*, 6923–6941.

(28) Otto, B.; Schroeder, J.; Troe, J. Photolytic cage effect and atom recombination of iodine in compressed gases and liquids: Experiments and simple models. *J. Chem. Phys.* **1984**, *81*, 202–213.

(29) Harris, A. L.; Brown, J. K.; Harris, C. B. The nature of simple photodissociation reactions in liquids on ultrafast time scales. *Annu. Rev. Phys. Chem.* **1988**, *39*, 341–356.

(30) Parson, R.; Faeder, J.; Delaney, N. Charge flow and solvent dynamics in the photodissociation of solvated molecular ions. *J. Phys. Chem. A* **2000**, *104*, 9653–9665.

(31) Schroder, H.; Gabriel, H. Classical simulation of a cage effect in the dissociation of I_2Rg_n clusters (Rg=Ar,Kr,Xe; n¡=5). *J. Chem. Phys.* **1996**, *104*, 587–598.

(32) Jarzynski, C. Nonequilibrium Equality for Free Energy Differences. *Phys. Rev. Lett.* **1997**, *78*, 2690–2693.

(33) Vong, A.; Mei, K. J.; Widmer, D. R.; Schwartz, B. J. Solvent Control of Chemical Identity Can Change Photodissociation into Photoisomerization. *J. Phys. Chem. Lett.* **2022**, *13*, 7931–7938.

(34) Chandler, D., *Introduction to Modern Statistical Mechanics*; Oxford Univ. Press: New York, 1987.

(35) Laird, B. B.; Thompson, W. H. On the connection between Gaussian statistics and excited-state linear response for time-dependent fluorescence. *J. Chem. Phys.* **2007**, *126*, 211104.

(36) Tao, G.; Stratt, R. M. The molecular origins of nonlinear response in solute energy relaxation: The example of high-energy rotational relaxation. *J. Chem. Phys.* **2006**, *125*, 114501.

(37) Goderis, D.; Verbeure, A.; Vets, P. About the Exactness of the Linear Response Theory. *Commun. Math. Phys.* **1991**.

(38) King, G.; Warshel, A. Investigation of the free energy functions for electron transfer reactions. *J. Chem. Phys.* **1990**, *93*, 8682–8692.

(39) Ingrosso, F.; Ladanyi, B. M.; Mennucci, B.; Elola, M. D.; Tomasi, J. Solvation Dynamics in Acetonitrile: A Study Incorporating Solute Electronic Response and Nuclear Relaxation. *J. Phys. Chem. B.* **2004**, *109*, 3553–3564.

(40) Fonseca, T.; Ladanyi, B. M. Breakdown of Linear Response for Solvation Dynamics in Methanol. *J. Phys. Chem.* **1991**, *95*, 2116–2119.

(41) Ladanyi, B. M.; Maroncelli, M. Mechanisms of solvation dynamics of polyatomic solutes in polar and nondipolar solvents: A simulation study. *J. Chem. Phys.* **1998**, *109*, 3204–3221.

(42) Geissler, P. L.; Chandler, D. Importance sampling and theory of nonequilibrium solvation dynamics in water. *J. Chem. Phys.* **2000**, *113*, 9759–9765.

(43) Aherne, D.; Tran, V.; Schwartz, B. J. Non-Linear, Non-Polar Solvation Dynamics in Water: The Roles of Electrostriction and Solvent Translation in the Breakdown of Linear Response. *J. Phys. Chem. B* **2000**, *104*, 5382–5394.

(44) Hammes-Schiffer, S. Theoretical Perspectives on proton-coupled electron transfer reactions. *Acc. Chem. Res.* **2001**, *34*, 273–281.

(45) Moskun, A. C.; Jailaubekov, A. E.; Bradforth, S. E.; Tao, G.; Stratt, R. M. Rotational coherence and a sudden breakdown in linear response seen in room-temperature liquids. *Science* **2006**, *311*, 1907–1911.

(46) Bragg, A. E.; Cavanagh, M. C.; Schwartz, B. J. Linear response breakdown in solvation dynamics induced by atomic electron-transfer reactions. *Science* **2008**, *321*, 1817–1822.

(47) Bragg, A. E.; Glover, W. J.; Schwartz, B. J. Watching the solvation of atoms in liquids one molecule at a time. *Phys. Rev. Lett.* **2010**, *104*, 1–4.

(48) Laird, B. B.; Thompson, W. H. Time-dependent fluorescence in nanoconfined solvents: Linear-response. approximations and Gaussian statistics. *J. Chem. Phys.* **2011**, *135*, 1–13.

(49) Vong, A.; Schwartz, B. J. Bond-Breaking Reactions Encounter Distinct Solvent Environments Causing Breakdown of Linear Response. *J. Phys. Chem. Lett.* **2022**, *13*, 6783–6791.

(50) Furse, K. E.; Lindquist, B. A.; Corcelli, S. A. Solvation Dynamics in Hoechst 33258 in Water: An Equilibrium and Nonequilibrium Molecular Dynamics Study. *J. Phys. Chem. B* **2008**, *112*, 3231–3239.

(51) Rick, S. W.; Stuart, S. J.; Berne, B. J. Dynamical Fluctuating Change Force Fields: Application to Liquid Water. *J. Chem. Phys.*, *101*, 6141–6156.

(52) Bernardi, E.; Martins, M. M.; Stassen, H. The Breakdown of Linear Response Theory in Non-Polar Solvation Dynamics. *Chem. Phys. Lett.* **2005**, *407*, 171–175.

(53) Carter, E. A.; Hynes, J. T. Solvation Dynamics for an Ion Pair in a Polar Solvent: Time-Dependent Fluorescence and Photochemical Charge Transfer. *J. Chem. Phys.*, *94*, 5961.

(54) Fonseca, T.; Ladanyi, B. M. Solvation Dynamics in Methanol: Solute and Perturbation Dependence. *J. Mol. Liq.* **1994**, *60*, 1–24.

(55) Phillips, J. C.; Kleinman, L. New method for calculating wave functions in crystals and molecules. *Phys. Rev.* **1959**, *116*, 287–294.

(56) Szaz, L., *Pseudopotential Theory of Atoms and Molecules*; Wiley: New York, 1985.

(57) Gervais, B.; Giglio, E.; Jacquet, E.; Ipatov, I.; Reinhard, P. G.; Suraud, E. Simple DFT model of clusters embedded in rare gas matrix: Trapping sites and spectroscopic properties of Na embedded in Ar. *J. Chem. Phys.* **2004**, *121*, 8466–8480.

(58) Smallwood, C. J.; Larsen, R. E.; Glover, W. G.; Schwartz, B. J. A computationally efficient exact pseudopotential method. I. Analytic reformulation of the Philips-Kleinman theory. *J. Chem. Phys.* **2006**, *125*, 074102.

(59) Smallwood, C. J.; Mejia, C. N.; Glover, W. G.; Larsen, R. E.; Schwartz, B. J. A computationally efficient exact pseudopotential method. 2. Application to the molecular pseudopotential of an excess electron interacting with tetrahydrofuran (THF). *J. Chem. Phys.* **2006**, *125*, 074103.

(60) Widmer, D. R.; Schwartz, B. J. The role of the solvent in the condensed-phase dynamics and identity of chemical bonds: The case of the sodium dimer cation in THF. *J. Phys. Chem. B* **2020**, *124*, 6603–6616.

(61) Widmer, D. R.; Schwartz, B. J. Solvents can control solute molecular identity. *Nat. Chem.* **2018**, *10*, 910–916.

(62) Glover, W. J.; Larsen, R. E.; Schwartz, B. J. The roles of electronic exchange and correlation in charge-transfer-to-solvent dynamics: Many-electron non-adiabatic mixed quantum/classical simulations of photoexcited sodium anions in the condensed phase. *J. Chem. Phys.* **2008**, *129*, 164505.

(63) Glover, W. J.; Larsen, R. E.; Schwartz, B. J. Simulating the formation of sodium:electron tight-contact pairs: Watching the solvation of atoms in liquids one molecule at a time. *J. Phys. Chem. A* **2011**, *115*, 5887–5894.

(64) Glover, W. J.; Larsen, R. E.; Schwartz, B. J. The nature of sodium atoms/(Na^+-e^-) contact pairs in liquid tetrahydrofuran. *J. Phys. Chem. B* **2010**, *114*, 11535–115439.

(65) Glover, W. J.; Larsen, R. E.; Schwartz, B. J. First principles multi-electron mixed quantum/classical simulations in the condensed phase. II. The charge-transfer-to-solvent states of sodium anions in liquid tetrahydrofuran. *J. Chem. Phys.* **2010**, *132*, 144102.

(66) Glover, W. J.; Schwartz, B. J. How does a solvent affect chemical bonds? Mixed quantum/classical simulations with a full CI treatment of the bonding electrons. *J. Phys. Chem. Lett.* **2010**, *1*, 165–169.

(67) Niv, M. Y.; Bargheer, M.; Gerber, R. B. Photodissociation and recombination of F_2 molecule in Ar_{54} cluster: Nonadiabatic molecular dynamics simulations. *J. Chem. Phys.* **2000**, *113*, 6660–6672.

(68) Winter, N.; Chorny, I.; Vieceli, J.; Benjamin, I. Molecular dynamics study of the photodissociation and photoisomerization of ICN in water. *J. Chem. Phys.* **2003**, *119*, 2127–2143.

(69) Peslherbe, G. H.; Ladanyi, B. M.; Hynes, J. T. Trajectory study of photodissociation dynamics in the $NaI(H_2O)$ cluster system. *J. Phys. Chem. A* **1998**, *102*, 4100–4110.

(70) Kirkwood, J. G. Statistical Mechanics of Fluid Mixtures. *J. Chem. Phys.* **1935**, *3*, 300–313.

(71) Timko, J.; Castro, A. D.; Kuyucak, S. Ab initio calculation of the potential of mean force for dissociation of aqueous Ca-Cl. *J. Chem. Phys.* **2011**, *134*, 204510.

(72) Zhang, C.; Giberti, F.; Sevgen, E.; de Pablo, J. J.; Gygi, F.; Galli, G. Dissociation of salts in water under pressure. *Nat. Commun.* **2020**, *11*, 3037.

(73) Pham, V.-T.; Fulton, J. L. Ion-pairing in aqueous $CaCl_2$ and RbBr solutions: Simultaneous structural refinement of XAFS and XRD data. *J. Chem. Phys.* **2013**, *138*, 044201.

(74) Yaspal S. Badyal Adrian C. Barnes, G. J. C.; Simonson, J. M. Understanding the effects of concentration on the solvation structure of Ca^{2+} in aqueous solution. II: Insights into longer range order from neutron diffraction isotope substitution. *J. Phys. Chem. A* **2004**, *108*, 11819–11827.

(75) Schmidt, C. Raman spectroscopic determination of carbon speciation and quartz solubility in H_2O + Na_2CO_3 and H_2O + $NaHCO_3$ fluids to 600°C and 1.53 GPa. *Geochim. Cosmochim. Acta* **2014**, 281–296.

(76) Voth, G. A. Computer simulation of proton solvation and transport in aqueous and biomolecular systems. *Acc. Chem. Res.* **2006**, *39*, 143–150.

(77) Wong, K. F.; Watney, J. B.; Hammes-Schiffer, S. Analysis of electrostatics and correlated motions for hydride transfer in dihydrofolate reductase. *J. Phys. Chem. B* **2004**, *108*, 12231–12241.

(78) Ishida, T.; Hirata, F.; Kato, S. Solvation dynamics of benzonitrile excited state in polar solvents: A time-dependent reference interaction site model self-consistent field approach. *J. Chem. Phys* **1998**, *110*, 11423–11432.

(79) Koch, D. M.; Timerghazin, Q. K.; Peslherbe, G. H.; Ladanyi, B. M.; Hynes, J. T. Nonadiabatic Trajectory Studies of $NaI(H_2O)_n$ Photodissociation Dynamics. *J. Phys. Chem. A* **2000**, *110*, 1438–1454.

(80) Kahros, A.; Schwartz, B. J. Going beyond the frozen core approximation: development of coordinate-dependent pseudopotentials and application to Na_2^+. *J. Chem. Phys.* **2013**, *138*, 149901.

(81) Glover, W. J.; Larsen, R. E.; Schwartz, B. J. First principles multi-electron mixed quantum/classical simulations in the condensed phase. I. An efficient fourier-grid method for solving the many-electron problem. *J. Chem. Phys.* **2010**, *132*, 1–11.

(82) Allen, M. P.; Tildesley, D. J., *Computer Simulation of Liquids*; Oxford University Press: London, 1992.

(83) Shirts, M. R.; Chodera, J. D. Statistically optimal analysis of samples from multiple equilibrium states. *J. Chem. Phys.* **2008**, *129*, 124105.

(84) Steinhauser, O. Reaction field simulation of water. *Mol. Phys.* **1982**, *45*, 335–348.

(85) Allen, M. P.; Tildesley, D. J., *ARPACK Users' Guide, Solution of LargeScale Eigenvalue Problems with Implicitly Restarted Arnoldi Methods*; SIAM: Philadelphia, 1998.

(86) Chandrasekhar, J.; Jorgensen, W. L. The nature of dilute-solutions of sodium-ion in water, methanol, and tetrahydrofuran. *J. Chem. Phys.* **1982**, *77*, 5080–5089.

(87) Smit, B. Phase-diagrams of Lennard-Jones fluids. *J. Chem. Phys.* **1992**, *96*, 8639–8640.

(88) Ahmadi, G. R.; Almlöf, J.; Røeggen, I. The interaction potential for the $X^1\Sigma^+$ state of $ArNa^+$, $NeNa^+$ and $HeNa^+$. *Chem. Phys.* **1995**, *199*, 33–52.

(89) Larsen, R. E.; Glover, W. J.; Schwartz, B. J. Does the hydrated electron occupy a cavity? *Science* **2010**, *329*, 65–69.

(90) Voth, G. A.; Hochstrasser, R. M. Transition State Dynamics and Relaxation Processes in Solutions: A Frontier of Physical Chemistry. *J. Phys. Chem.* **1996**, *100*, 13034–13049.

(91) Keaveney, S. T.; White, B. P.; Haines, R. S.; Harper, J. B. The effects of ionic liquid on unimolecular substitution processes: the importance of the extent of transition state solvation. *Org. Biomol. Chem.* **2016**, *14*, 2572–2580.

(92) Goyal, P.; Schwerdtfeger, C. A.; Soudackov, A. V.; Hammes-Schiffer, S. Proton Quantization and Vibrational Relaxation in Nonadiabatic Dynamics of Photoinduced Proton-Coupled Electron Transfer in a Solvated Phenol-Amine Complex. *J. Phys. Chem. B* **2016**, *120*, 2407–2417.

(93) Margulis, C. J.; Coker, D. F.; Lynden-Bell, R. M. Symmetry Breaking of the Triiodide Ion in Acetonitrile Solution. *Chem. Phys. Lett.* **2001**, *341*, 557–560.

(94) Zhang, F. S.; Lynden-Bell, R. M. Solvent-Induced Symmetry Breaking. *Phys. Rev. Lett.* **2003**, *90*, 185505.

(95) Zhang, F. S.; Lynden-Bell, R. M. Solvent-Induced Symmetry Breaking: Varying Solvent Strength. *Phys. Rev. E* **2005**, *71*, 021502.

(96) Maroncelli, M. Computer simulations of solvation dynamics in acetonitrile. *J. Chem. Phys.* **1990**, *94*, 2084–2103.

(97) Kumar, P. V.; Maroncelli, M. Polar solvation dynamics of polyatomic solutes: Simulation studies in acetonitrile and methanol. *J. Chem. Phys.* **1995**, *103*, 3038–3060.

(98) Truhlar, D. G.; Garrett, B. C.; Klippenstein, S. J. Current Status of Transition-State Theory. *J. Phys. Chem.* **1996**, *100*, 12771–12800.

(99) Stratt, R. M.; Maroncelli, M. Nonreactive Dynamics in Solution: The Emerging Molecular View of Solvation Dynamics and Vibrational Relaxation. *J. Phys. Chem.* **1996**, *100*, 12981–12996.

(100) Tachiya, M. Relation between the Electron-Transfer Rate and the Free Energy Change of Reaction. *J. Phys. Chem.* **1989**, *93*, 7050–7052.

(101) Wu, Q.; Voorhis, T. V. Direct Calculation of Electron Transfer Parameters through Constrained Density Functional Theory. *J. Phys. Chem. A* **2006**, *110*, 9212–9218.

(102) Zhu, J.; Spirina, O. B.; Cukier, R. I. Solvent dynamical effects on bond-breaking electron transfer reactions. *J. Chem. Phys.* **1994**, *100*, 8109–8124.

(103) Grabowski, Z. R.; Rotkiewicz, K.; Rettig, W. Structural Changes Accompanying Intramolecular Electron Transfer: Focus on Twisted Intramolecular Charge-Transfer States and Structures. *Chem. Rev.* **2003**, *103*, 3899–4032.

(104) Ghosh, S.; Soudackov, A. V.; Hammes-Schiffer, S. Electrochemical Electron Transfer and Proton-Coupled Electron Transfer: Effects of Double Layer and Ionic Environment on Solvent Reorganization Energies. *J. Chem. Theory Comput.* **2016**, *12*, 2917–2925.

(105) Warburton, R. E.; Soudackov, A. V.; Hammes-Schiffer, S. Theoretical Modeling of Electrochemical Proton-Coupled Electron Transfer. *Chem. Rev.* **2022**.

(106) Mak, C. C.; Timerghazinw, Q. K.; Peslherbe, G. H. Photoinduced electron transfer and solvation dynamics in aqueous clusters: comparison of the photoexcited iodide-water pentamer and the water pentamer anion. *Phys. Chem. Chem. Phys.* **2012**, *14*, 6257–6265.

(107) Marcus, R. A. On the theory of oxidation–reduction reactions involving electron transfer. *J. Chem. Phys.* **1956**, *24*, 966–978.

(108) Marcus, R. A.; Sutin, N. Electron transfers in chemistry and biology. *Biochim. Biophys. Acta.* **1985**, *811*, 265–322.

(109) Barthel, E. R.; Martini, I. B.; Schwartz, B. J. How does the solvent control electron transfer? Experimental and theoretical studies of the simplest charge transfer reaction. *J. Phys. Chem. B* **2001**, *105*, 12230–12241.

(110) Thi, T. H. T.; Prayer, C.; Millie, P.; Uznanski, P.; Hynes, J. T. Substituent and Solvent Effects on the Nature of the Transitions of Pyrenol and Pyranine. Identification of an Intermediate in the Excited-State Proton-Transfer Reaction. *J. Phys. Chem. A* **2002**, *106*, 2244–2255.

(111) Olivieri, J.-F.; Laage, D.; Hynes, J. T. A Model Electron Transfer Reactionin Confined Aqueous Solution. *Chem. Phys. Chem.* **2021**, *22*, 2247–2255.

(112) Jonely, M.; Noriega, R. Role of Polar Protic Solvents in the Dissociation and Reactivity of Photogenerated Radical Ion Pairs. *J. Phys. Chem. B* **2020**, *124*, 3083–3089.

(113) Jonely, M.; Noriega, R. Selectively Altering the Reactivity of Transient Organic Radical Ions via Their Solvation Environment. *J. Phys. Chem. B* **2022**, *126*, 3107–3115.

(114) Kauffman, J. F. Quadrupolar Solvent Effects on Solvation and Reactivity of Solutes Dissolved in Supercritical CO2. *J. Phys. Chem. A* **2001**, *105*, 3433–3442.

(115) Cusati, T.; Granucci, G.; Persico, M. Photodynamics and Time-Resolved Fluorescence of Azobenzene in Solution: A Mixed Quantum-Classical Simulation. *J. Am. Chem. Soc.* **2011**, *133*, 5109–5123.

(116) Torrie, G. M.; Valleau, J. P. 1977. *23*, 187–199.

(117) Humphrey, W.; Dalke, A.; Schulten, K. Visual Molecular Dynamics. **1996**, *14*, 33–38.